

# **Turbulent Structures of Non-Newtonian Solutions in Taylor-Couette Flow**

by

Haozhe Li

A thesis submitted in partial fulfillment of the requirements for the degree of

Master of Science

Department of Mechanical Engineering  
University of Alberta

© Haozhe Li, 2024

# Abstract

The turbulent structures of Taylor-Couette (T-C) flow of a Polyacrylamide (PAM) solution (200 and 400 ppm) is experimentally investigated and compared with the same flow with water at  $Re = 1.50 \times 10^4$ , to understand the effect of nonlinear shear-thinning viscosity on the flow regime, in terms of turbulence statistics, coherent structures, turbulence production, and viscous dissipation. The turbulent Taylor-Couette (TTC) flow regime is achieved and driven by inner cylinder rotation (outer cylinder stays stationary). Velocity measurements are conducted by employing Stereoscopic-Particle Image Velocimetry (SPIV) to obtain three velocity components within a rectangular field of view (FOV) in radial-axial ( $r - z$ ) (meridional) plane, and the torque acted on the inner cylinder is recorded to obtain skin friction coefficient  $C_{f,i}$ .

The torque measurements show that with the addition of shear-thinning polymer, 41% and 52% drag reduction is achieved for 200 ppm and 400 ppm solutions both under  $Re = 1.50 \times 10^4$ , respectively. The velocity measurement of the in-plane velocity shows that the motions of non-Newtonian Taylor vortices are more flexible compared to the Newtonian case in both the axial and radial direction induced by the shear-thinning effect. The turbulence statistics show that wall-normal ( $r$ ) and spanwise ( $z$ ) Reynolds normal stresses are significantly attenuated and smeared out across the bulk domain as the concentration of shear-thinning polymers increases. The radial jet (both inner and outer jets) intensity is reduced with the addition of shear-thinning polymer. Snapshot Proper Orthogonal Decomposition (POD) of in-plane velocity fluctuations field shows that vortical-shape fluctuations are the dominant energetic structures for both Newtonian and non-Newtonian T-C flows that statistically contribute to most of the turbulence kinetic energy (TKE) for both Newtonian and

non-Newtonian fluids. The shear layer structure changes due to the shear-thinning effect, which is reflected by the second POD mode. The Snapshot POD of the azimuthal velocity fluctuation field captures energetic structures at locations where turbulence is generated and the shear-thinning effect is pronounced. With the addition of shear-thinning polymer, the energetic structures are compressed closer to the wall, and the bulk flow becomes less important in terms of contributing to turbulence production.

The spatial correlation analysis of the in-plane velocity fluctuations shows that the shear-thinning polymer enhances the space correlation compared to the Newtonian fluid. Anti-correlation is found more pronounced than the Newtonian case in the axial direction, which leads to a reduced magnitude of axial integral lengthscale  $L_{33}$ . The 2D energy spectrum shows that the Kolmogorov  $-5/3$  law does not hold for T-C turbulence for both Newtonian and non-Newtonian fluids. Non-Newtonian energy spectrum based on radial and azimuthal fluctuations shows an increased importance of large-scale structures and a decreased importance of motions at small lengthscales in terms of energy containment. The dissipation spectrum shows increased contribution for dissipation at smaller lengthscales as concentration increases.

# Preface

This thesis is an original work by Haozhe Li. No part of this thesis has been previously published.

# Acknowledgements

I would like to express my sincere gratitude to Dr. Fleck for his instruction and support throughout my Master's program. He has supported and provided me with the necessary resources to conduct my research, and his mentorship and guidance were invaluable in shaping my academic and professional development. His belief in my abilities has given me the confidence to pursue my academic goals and to strive for excellence in my research. I am deeply grateful for his mentorship and for the opportunities he has provided me to study at the University of Alberta with the top scholars in the world. Without him, none of the progress I made would have been achieved.

I would also like to thank Dr. Nobes for his guidance in experiments and support during my time as his student. His expertise in experimental research has been a tremendous asset to my education and has inspired me to become a great experimentalist. I have learned a lot with Dr. Nobes in terms of fluid visualization and velocimetry measurement. His guidance and instruction have helped me develop a deeper understanding of the experimental research process.

I am grateful to the best instructors, Dr. Alexandra Komrakova, Dr. Jaime Wong, and Dr. Sina Ghaemi for their excellent courses in CFD, fluid dynamics, and turbulence, which are invaluable and insightful for me. I have learned so much from them.

I am grateful to all the friends I have known in my graduate study, Dr. Guilherme Bessa, Sina Kashanj, Yeganeh Saffar, Emran Hamzehnezhadabkenari, Linda Hasanovich, Jason Der, Khashayar Rahnamaybahambary, Mohammad Reza Kavian Nezhad, Jake Hadfield, Adam Lim, Soufyane Ayed, Dr. Mohammad Mahmoodi, Yutai Liu, Muaadh Baessa, Yifan Li, Song Xue (Wuhan University), Xiaomiao Pan (BJTU), Yash Kothari, Jiale Zhu, Dr. Shaofeng

Yang, Zepeng Zhang(ShanghaiTech University), Laura Chen, Ashley Chen, Andrea Rodriguez Moreno. Their love and support have been critical in helping me overcome the challenges of graduate school and in helping me achieve my academic goals. I wish all the best to them in their studies and their careers.

# Table of Contents

<b>1</b>	<b>Introduction</b>	<b>1</b>
1.1	Motivation . . . . .	1
1.2	Taylor-Couette Flow . . . . .	3
1.2.1	Governing Equations . . . . .	4
1.2.2	Taylor-Couette Flow of Newtonian Fluids . . . . .	6
1.2.3	Taylor-Couette Flow of Shear-thinning Fluids . . . . .	10
1.3	Polymers and Polymeric Flows . . . . .	12
1.3.1	Classification of Polymers and Polymer Solutions . . . . .	13
1.3.2	Viscoelasticity . . . . .	14
1.3.3	Drag Reduction . . . . .	15
1.3.4	Turbulent Polymeric Boundary Layer . . . . .	17
1.4	Ensemble Mean, Fluctuation, and Variances . . . . .	18
1.5	Energy Cascade . . . . .	20
1.6	Application of Proper Orthogonal Decomposition in Turbulence . . . . .	22
1.7	Stereoscopic PIV Measurement Technique . . . . .	24
1.8	Objectives and Hypothesis . . . . .	25
1.9	Thesis Outline . . . . .	26
<b>2</b>	<b>Experimental Setup And Methodology</b>	<b>27</b>
2.1	Overview . . . . .	27
2.2	T-C Flow Apparatus . . . . .	27
2.3	Stereo-scopic PIV Configuration . . . . .	30
2.3.1	Field of View (FOV) . . . . .	30
2.3.2	Camera Arrangement . . . . .	31
2.3.3	Camera Angle . . . . .	32
2.3.4	Reservoir for Refraction Elimination . . . . .	32
2.3.5	Seeding . . . . .	33
2.3.6	Particle Image Displacement . . . . .	35
2.3.7	Calibration . . . . .	36

2.4	Viscosity Model and Polymer Solutions . . . . .	38
2.4.1	Viscosity Model . . . . .	38
2.4.2	Experimental Fluids . . . . .	39
2.4.3	Preparation Procedure . . . . .	40
2.4.4	Post-Processing . . . . .	41
2.5	SPIV Accuracy and Uncertainty Analysis . . . . .	41
<b>3</b>	<b>Results</b>	<b>44</b>
3.1	Overview . . . . .	44
3.2	Statistical Convergence . . . . .	45
3.2.1	Estimation of Time Span . . . . .	45
3.2.2	Estimation of Number of Samples . . . . .	47
3.3	Skin Friction and Prandtl-von Kármán Law . . . . .	51
3.4	Observations of Instantaneous and Mean Taylor Vortices . . . . .	53
3.5	Turbulence Statistics . . . . .	57
3.5.1	Radial and Axial Fluctuation Statistics . . . . .	57
3.5.2	Reynolds Shear Stress Statistics . . . . .	60
3.6	Radial Jet Instability . . . . .	63
3.7	Vorticity Magnitude . . . . .	65
3.8	Vortex Centre Location, Core Size and Circulation . . . . .	67
3.8.1	Vortex Centre location . . . . .	67
3.8.2	Vortex Core Size . . . . .	69
3.8.3	Circulation . . . . .	72
3.9	Spatial Organization of Energetic Modes . . . . .	73
3.9.1	Spatial Modes Based on In-plane Velocities . . . . .	75
3.9.2	Spatial Modes Based on Azimuthal Velocity . . . . .	84
3.10	Two-Point Correlation . . . . .	85
3.11	Energy and Dissipation Spectrum . . . . .	92
3.11.1	Energy Spectrum Based on Radial and Axial Velocity Fluctuation . . . . .	93
3.11.2	Energy Spectrum Based on Radial and Azimuthal Fluctuation . . . . .	95
3.11.3	Dissipation Spectrum . . . . .	95
<b>4</b>	<b>Discussion</b>	<b>98</b>
<b>5</b>	<b>Conclusion</b>	<b>102</b>
<b>6</b>	<b>Future Work</b>	<b>104</b>

<b>Appendix A: Coordinate Conversion</b>	<b>116</b>
A.1 Cartesian Coordinate System to Cylindrical Coordinate system . . . . .	116
<b>Appendix B: Equation Derivations</b>	<b>118</b>
B.1 Relation between $C_{f,s}$ and $C_{f,l}$ . . . . .	118
<b>Appendix C: Matlab Code</b>	<b>120</b>
C.1 Code for POD Analysis . . . . .	120
C.2 Code for Energy Spectrum . . . . .	128
<b>Appendix D: Engineering Drawings of Taylor-Couette Flow Rig</b>	<b>132</b>

# List of Tables

2.1	List of dynamic characteristics of the seeding particles under the flow conditions at $Re = 1.50 \times 10^4$ . . . . .	35
2.2	List of experimental parameters and optical system properties for SPIV measurement. . . . .	36
2.3	Carreau-Yasuda model parameters for tested solutions. Property of PAM data comes from (Azadi 2023). Properties of glycerol-water mixtures come from (Volk and Kähler 2018). . . . .	39
3.1	List of experimental parameters of number of samples and number of images in each experiment. . . . .	49
3.2	Mean and standard deviation of vortex core sizes for three fluids. . . . .	71
3.3	List of integral lengthscales of $L_{11}$ and $L_{33}$ for three solutions. . . . .	91

# List of Figures

1.1	Schematic of Taylor-Couette flows and secondary vortices in the meridional plane. . . . .	3
1.2	Plot of mean velocity profiles of turbulent polymeric flows. . . . .	18
2.1	Annotated schematic of Taylor-Couette apparatus. . . . .	28
2.2	Schematic of field of view (FOV). . . . .	31
2.3	Schematic of Calibration Target. The left image shows the dot pattern of the calibration target. The dark dots are on the top level, and the light grey dots are on the bottom level. The right image shows the 3D view of the target. . . . .	37
2.4	Plot of Dynamic viscosity versus shear rate. Figure replotted with permission (Azadi and Nobes 2022). . . . .	40
2.5	Plot of Normalized azimuthal velocity profile for $Re \approx 10$ . . . . .	43
3.1	Variability of statistics for water at $Re = 1.50 \times 10^4$ . (a) Mean statistics based on ensemble average and axial-ensemble average. (b) Variance statistics based on ensemble average and axial-ensemble average. . . . .	50
3.2	Variability of statistics for PAM-200ppm at $Re = 1.50 \times 10^4$ . (a) Mean statistics based on ensemble average and axial-ensemble average. (b) Variance statistics based on ensemble average and axial-ensemble average. . . . .	50
3.3	Variability of statistics for PAM-400ppm at $Re = 1.50 \times 10^4$ . (a) Mean statistics based on ensemble average and axial-ensemble average. (b) Variance statistics based on ensemble average and axial-ensemble average. . . . .	51
3.4	Plot of skin friction coefficient vs $Re$ . . . . .	52
3.5	Plot of streamlines of turbulent Taylor-Couette vortical structures for water at $Re = 1.50 \times 10^4$ . (a-b) Streamlines of instantaneous velocity $\mathbf{U}(U_r, U_z)$ . (c) Streamlines of ensemble-averaged velocity $\langle \mathbf{U}(U_r, U_z) \rangle_N$ . . . . .	54
3.6	Plot of streamlines of Taylor-Couette vortical structures for PAM-200 ppm at $Re = 1.50 \times 10^4$ . (a-b) Streamlines of instantaneous velocity. (c) Streamlines of ensemble-averaged velocity $\langle \mathbf{U}(U_r, U_z) \rangle_N$ . . . . .	55

3.7	Plot of streamlines of turbulent Taylor-Couette vortical structures for PAM-400ppm at $Re = 1.50 \times 10^4$ . (a-c) Streamlines of instantaneous velocity $\mathbf{U}(U_r, U_z)$ . . . . .	56
3.8	Plot of second order statistics of water at $Re = 1.50 \times 10^4$ . (a) Contour of variances of radial velocity $\langle u_r^2 \rangle_N / U_{ref}^2$ . (b) Contour of variances of axial velocity $\langle u_z^2 \rangle_N / U_{ref}^2$ . . . . .	57
3.9	Plot of second-order statistics of PAM-200 ppm at $Re = 1.50 \times 10^4$ . (a) Contour of variances of radial velocity $\langle u_r^2 \rangle_N / U_{ref}^2$ . (b) Contour of variances of axial velocity $\langle u_z^2 \rangle_N / U_{ref}^2$ . . . . .	59
3.10	Plot of second-order statistics of PAM-400 ppm at $Re = 1.50 \times 10^4$ . (a) Contour of variances of radial velocity $\langle u_r^2 \rangle_N / U_{ref}^2$ . (b) Contour of variances of axial velocity $\langle u_z^2 \rangle_N / U_{ref}^2$ . . . . .	60
3.11	Schematic of demonstration of the sign of $u_i u_j$ in streamwise-wall-normal direction. (a) stationary wall-bounded flows (b) moving wall-bounded flows. . . . .	61
3.12	Plot of statistics $\langle u_r u_\theta \rangle_N$ in the $r - z$ plane for (a) water, (b) PAM-200 ppm, and (c) PAM-400 ppm. . . . .	62
3.13	Plot of example of fluctuation statistics $u_r u_\theta$ in the $r - z$ plane for (a) water, (b) PAM-200ppm, and (c) PAM-400ppm. Regions that $u_r u_\theta$ is greater than $\langle u_r u_\theta \rangle_N$ is highlighted (for $u_r < 0$ the region is enclosed with solid lines, and for $u_r > 0$ the region is enclosed with dashed lines). . . . .	63
3.14	Plot of time evolution of radially-averaged quantity $\langle U_r \rangle_r$ at $Re = 1.50 \times 10^4$ . (a) Water. (b) PAM-200 ppm. (c) PAM-400 ppm . . . . .	64
3.15	Plot of contour of ensemble-averaged azimuthal vorticity $\langle \omega_\theta \rangle_N$ distribution. (a) Water, $Re = 1.50 \times 10^4$ . (b) PAM-200 ppm, $Re = 1.50 \times 10^4$ . . . . .	66
3.16	Plot of scatter of spatial distributions of vortex centre locations at $Re = 1.50 \times 10^4$ . The scatter of vortex centre locations is colored by Kernel probability density estimate. The triangles indicate the ensemble-mean vortex centre locations. (a) Water. (b) PAM-200 ppm. (c) PAM-400 ppm. . . . .	70
3.17	Plot of the probability density function of vortex core sizes. (a) Lognormal probability density function (PDF) of vortex sizes. (b) Lognormal probability cumulative density function (CDF) of vortex core sizes. . . . .	71
3.18	Probability density histogram of the magnitude of circulation for (a) water. (b) PAM-200 ppm. (c) PAM-400 ppm. . . . .	73
3.19	Plot of spatial modes of radial velocity fluctuation of water at $Re = 1.5 \times 10^4$ . (a) mode 1. (b) mode 2. (c) mode 3. The vector shows $\phi_j(\phi_{j,r}, \phi_{j,z})$ and background shows the value of $\phi_{j,r}$ . . . . .	76

3.20	Plot of spatial modes of axial velocity fluctuation of water at $Re = 1.5 \times 10^4$ . (a) mode 1. (b) mode 2. (c) mode 3. The vector shows $\phi_j(\phi_{j,r}, \phi_{j,z})$ and background shows the value of $\phi_{j,z}$ . . . . .	77
3.21	Plot of demonstration of the second mode structure. (a) An instantaneous radial velocity fluctuation (b) Reconstruction of the radial velocity component by using only the second mode. . . . .	78
3.22	Plot of spatial modes of radial velocity fluctuation of PAM-200 ppm solution at $Re = 1.50 \times 10^4$ . (a) mode 1. (b) mode 2. (c) mode 3. The vector shows $\phi_j(\phi_{j,r}, \phi_{j,z})$ and background shows the value of $\phi_{j,r}$ . . . . .	79
3.23	Plot of spatial modes of axial velocity fluctuation of PAM-200 ppm solution at $Re = 1.50 \times 10^4$ . (a) mode 1. (b) mode 2. (c) mode 3. The vector shows $\phi_j(\phi_{j,r}, \phi_{j,z})$ and background shows the value of $\phi_{j,z}$ . . . . .	80
3.24	Plot of spatial of radial velocity fluctuation of PAM-400 ppm solution at $Re = 1.50 \times 10^4$ . (a) mode 1. (b) mode 2. (c) mode 3. The vector shows $\phi_j(\phi_{j,r}, \phi_{j,z})$ and background shows the value of $\phi_{j,r}$ . . . . .	81
3.25	Plot of spatial modes of axial velocity fluctuation of PAM-400 ppm solution at $Re = 1.50 \times 10^4$ . (a) mode 1. (b) mode 2. (c) mode 3. The vector shows $\phi_j(\phi_{j,r}, \phi_{j,z})$ and background shows the value of $\phi_{j,z}$ . . . . .	82
3.26	Plot of singular values and cumulative energy as a function of mode number. (a) Singular values $\sigma_r$ . (b) Cumulative energy in first $r$ modes. . . . .	83
3.27	Plot of spatial mode 1 of azimuthal velocity fluctuation of different fluids at $Re = 1.50 \times 10^4$ . (a) Water. (b) PAM-200 ppm. (c) PAM-400 ppm. The background shows the value of $\phi_{j,\theta}$ . . . . .	85
3.28	Plot of contours of two-point correlation of water based on an example reference point at $r^* = 0.5$ and $z^* = 1.4$ . (a) Contour of $\tilde{R}_{11}$ . (b) Contour of $\tilde{R}_{13}$ . (c) Contour of $\tilde{R}_{33}$ . . . . .	87
3.29	Plot of contours of two-point correlation of PAM-200 ppm based on an example reference point at $r^* = 0.5$ and $z^* = 1.4$ . (a) Contour of $R_{11}$ . (b) Contour of $R_{13}$ . (c) Contour of $R_{33}$ . . . . .	88
3.30	Plot of contours of two-point correlation of PAM-400 ppm based on an example reference point at $r^* = 0.5$ and $z^* = 1.4$ . (a) Contour of $R_{11}$ . (b) Contour of $R_{13}$ . (c) Contour of $R_{33}$ . . . . .	89
3.31	Plot of distribution of normalized two-point correlation in radial and axial direction at reference point $r^* = 0.5, z^* = 1.4$ . (a) $\tilde{R}_{11}$ distribution in $r$ direction. (b) $\tilde{R}_{33}$ distribution in $z$ direction. . . . .	90
3.32	Plot of ratio of ratio of integral lengthscale $L_{33}/L_{11}$ of water, PAM-200 ppm, and PAM-400 ppm. . . . .	92

3.33	Plot of turbulence kinetic energy spectrum over wavenumber with solutions under $Re = 1.50 \times 10^4$ . (a) Water. (b) PAM-200 ppm. (c) PAM-400 ppm. . . . .	94
3.34	Plot of normalized energy spectrum based on radial and azimuthal fluctuation over wavenumber with three solutions under $Re = 1.50 \times 10^4$ . (a) Water. (b) PAM-200 ppm. (c) PAM-400 ppm. . . . .	96
3.35	Plot of turbulent dissipation spectrum $k^2 E_{13}(k)$ over wavenumber with solutions under $Re = 1.50 \times 10^4$ . (a) Water. (b) PAM-200 ppm. (c) PAM-400ppm. The dashed line shows the cumulative dissipation percentage over the wavenumber. . . . .	97

# List of Symbols

## Constants

$B$  Logarithmic intercept for law of the wall 5

## Latin

$C$  normalized covariance data matrix

$C_{f,l}$  skin coefficient

$C_{f,s}$  skin coefficient,  $C_{f,l}/C_{f,s} = \pi r_i^2/d^2$

$C_p$  concentration of polymer

$d$  gap width between cylinders

$\mathbf{D}$  strain-rate tensor

$D$  data matrix of velocity fluctuation field over time

$D(\kappa)$  dissipation function

$D_I$  interrogation window size

$E$  energy spectrum function

$\mathbf{e}$  unit vector

$f$  acquisition rate of camera

$Fr$  Froude number

$G$  dimensionless torque

$L$  aspect ratio of the setup

$l_0$  characteristic lengthscale

$l_c$  length of the cylinder

$l_{DI}$  lengthscale demarcating inertial subrange and dissipation range

$l_{EI}$  lengthscale demarcating energy-containing range and universal equilibrium range

$n$  flow index

$R$	two-point correlation function
Re	Reynolds number
$r$	rank of velocity fluctuation matrix $\mathbf{D}$
$\tilde{R}$	normalized two-point correction
$r$	radial direction
$r^*$	dimensionless radial distance
$r_i$	radius of inner cylinder
$r_o$	radius of outer cylinder
$r^+$	dimensionless radial distance
$\mathbf{S}$	fluctuation of strain rate tensor
Stk	Stokes number
Ta	Taylor number
T	torque
$u$	velocity fluctuation based on ensemble average, $u = U - \langle U \rangle_N$
$\mathbf{U}$	velocity vector
$\mathbf{U}_g$	settling velocity
$u'$	velocity fluctuation based on ensemble-axial average, $u' = U - \langle U \rangle_{z,N}$
$U^+$	dimensionless velocity
$u_\eta$	Kolmogorov velocity scale
$U_\theta$	instantaneous azimuthal velocity
$U_{ref}$	velocity scale
$U_r$	instantaneous radial velocity
$U_z$	instantaneous axial velocity
We	Weissenberg number
$y^+$	dimensionless distance from the wall
$z$	axial direction
$z^*$	dimensionless axial distance

### Greek

$\dot{\gamma}_{\text{nom}}$  nominal shear rate

$\Gamma$	second invariant of strain rate tensor
$\Gamma_S$	circulation
$\delta$	Dirac delta function
$\varepsilon$	dissipation rate
$\zeta$	aspect ratio
$\eta$	Kolmogorov lengthscale
$\eta_r$	radius ratio
$\theta$	azimuthal direction
$\boldsymbol{\kappa}$	wavenumber vector
$\kappa$	von Kármán constant (Equation 1.19)
$\kappa$	wavenumber magnitude
$\kappa_r$	radial wavenumber
$\kappa_z$	axial wavenumber
$\lambda_c$	relaxation time of the fluid
$\mu$	dynamic viscosity of the fluid
$\mu_0$	dynamic viscosity at zero shear rate
$\mu_\infty$	dynamic viscosity at infinite shear rate
$\nu$	kinematic viscosity
$\rho$	fluid density
$\sigma$	geometrical Prandtl number
$\tau_\eta$	Kolmogorov timescale
$\tau_p$	particle's response time
$\Phi_{ij}(\boldsymbol{\kappa})$	velocity spectrum function
$\omega_\theta$	azimuthal vorticity magnitude
$\omega_i$	angular velocity of inner cylinder

# Abbreviations

**BLs** boundary layers.

**DNS** direct numerical simulation.

**DR** drag reduction.

**FOV** field of view.

**GV** Görtler vortices.

**LDV** laser doppler anemometry.

**LES** large eddy simulation.

**MDR** maximum drag reduction.

**MWVF** modulated wavy Vortex flow.

**PAM** Polyacrylamide.

**PDF** probabilty density function.

**PIV** particle image velocimetry.

**POD** proper orthogonal decomposition.

**RANS** Reynolds-Averaged Navier-Stokes.

**RI** refractive index.

**SPIV** stereo-scopic particle image velocimetry.

**TBL** turbulent boundary layer.

**T-C** Taylor-Couette.

**TKE** turbulence kinetic energy.

**TTVF** turbulent Taylor vortex flow.

**TVF** Taylor vortex flow.

**WVF** wavy vortex flow.

**XG** xanthan gum.

# Chapter 1

## Introduction

### 1.1 Motivation

Shear-thinning polymers can modify turbulent flow patterns and exhibit a strong influence on changing turbulent structures. These properties can be tailored in engineering applications. Numerous studies have demonstrated that the addition of polymers alters the near-wall flow structures and statistics in wall-bounded flows (Housiadas and Beris 2003; Warholic *et al.* 2001). This modification leads to various physical phenomena, including drag reduction (Mohammadtabar *et al.* 2017), decrease in cavitation intensity (Azadi 2023), transition delay to turbulence (Rudman and Blackburn 2012), and decrease in total turbulent dissipation (Singh *et al.* 2017). Therefore, understanding polymeric flow behaviors under turbulent conditions can contribute to more efficient processes and economic energy consumption.

Taylor-Couette turbulence of high Re has been extensively studied for Newtonian fluids (Berghout *et al.* 2020; Grossmann *et al.* 2016; Huisman *et al.* 2012, 2013b; Ostilla-Mónico *et al.* 2014). The investigation of shear-thinning Taylor-Couette turbulence, especially at high Reynolds numbers in the turbulent Taylor-Couette (TTC) regime, remains under-explored. Existing experimental investigations of shear-thinning Taylor-Couette flow has only covered a relatively low Reynolds number range from 0-1000 (Cagney and Balabani 2019; Elçiçek and Güzel 2020) encompassing circular Couette flow, Taylor-Vortex flow, and wavy vortex flow regimes. Information regarding the effects of polymer additives on the turbulent Taylor-Couette (TTC) regime, characterized by a high rate of angular momentum transfer and

strong dissipation is still lacking. Additionally, while some research has delved into turbulent structures in the TTC regime (Dong 2007; Krygier *et al.* 2021; Martínez-Arias *et al.* 2014), there is no available information examining the nonlinear shear-thinning viscosity effects of polymers on coherent structures in the TTC regime, making this study novel.

The Taylor-Couette geometry was chosen based on the following factors: (a) Rich turbulent flow structures including Taylor vortices and radial jets exist in the  $r - z$  direction. (b) Taylor-Couette flow geometry is a special case of wall-bounded flows where the curvature effect influences the distribution of statistics in the radial (wall-normal) direction. In a laminar flow case, a classical Newtonian plane Couette flow shows linear distribution of velocity, i.e., constant shear rate. However, the curvature effect of T-C geometry with Newtonian fluids results in an increasing concave-up azimuthal velocity from inner to outer cylinder, with a higher shear rate close to the inner cylinder and a lower shear rate close to the outer cylinder. From this perspective, the curvature effect acts in the same direction as the shear-thinning effect close to the inner cylinder wall.

Taylor-Couette flows, like other wall-bounded flows, share similarities with channel flows. Numerous studies on polymeric channel flows focus on near-wall turbulent statistics. For stationary flat wall-bounded turbulence for polymeric flows, it is widely accepted that polymer additives can reduce the wall-normal and spanwise velocity fluctuation as well as Reynolds shear stresses (Kim *et al.* 2007; Min *et al.* 2003; Mitishita *et al.* 2023; Mohammadtabar *et al.* 2017; Procaccia *et al.* 2008; Rudd 1972; Thirumalai and Bhattacharjee 1996; Tiederman 1990; White and Mungal 2008; Willmarth and Wei 1987; Zadrazil *et al.* 2012). It was observed that in turbulent flows of polymeric solutions, positive and negative second-order covariance  $\langle uv \rangle_t$  were found, a term considered the source of production of turbulence kinetic energy in the Newtonian case, which stays mostly negative. This finding highlights the decreased importance of production by the wall (Warholic *et al.* 2001), It is argued that at maximum drag reduction (MDR), the wall does not produce turbulence (Warholic *et al.* 1999). Conversely, in Taylor-Couette flow turbulence, the rotation of the inner cylinder is a source of turbulent production and sustains constant energy input, which distinguishes this

as a study of forced turbulence, as opposed to free-decaying turbulence. Thus, it is plausible to postulate that in turbulent T-C polymeric flows, the coherent structures in the bulk flow will differ in terms of energy and dissipation distribution at different length scales.

## 1.2 Taylor-Couette Flow

Taylor-Couette (T-C) apparatus is a fundamental flow configuration that has been widely investigated in fluid dynamics (Akonur and Lueptow 2003; Huisman *et al.* 2012, 2013a; Schimpf *et al.* 2021). It consists of two independently rotating cylinders where the flow is confined in between the annulus space (Grossmann *et al.* 2016). A schematic of the Taylor-Couette apparatus is shown in Figure 1.1, where  $r$  is the radial direction,  $\theta$  is the azimuthal direction and  $z$  indicates axial direction.

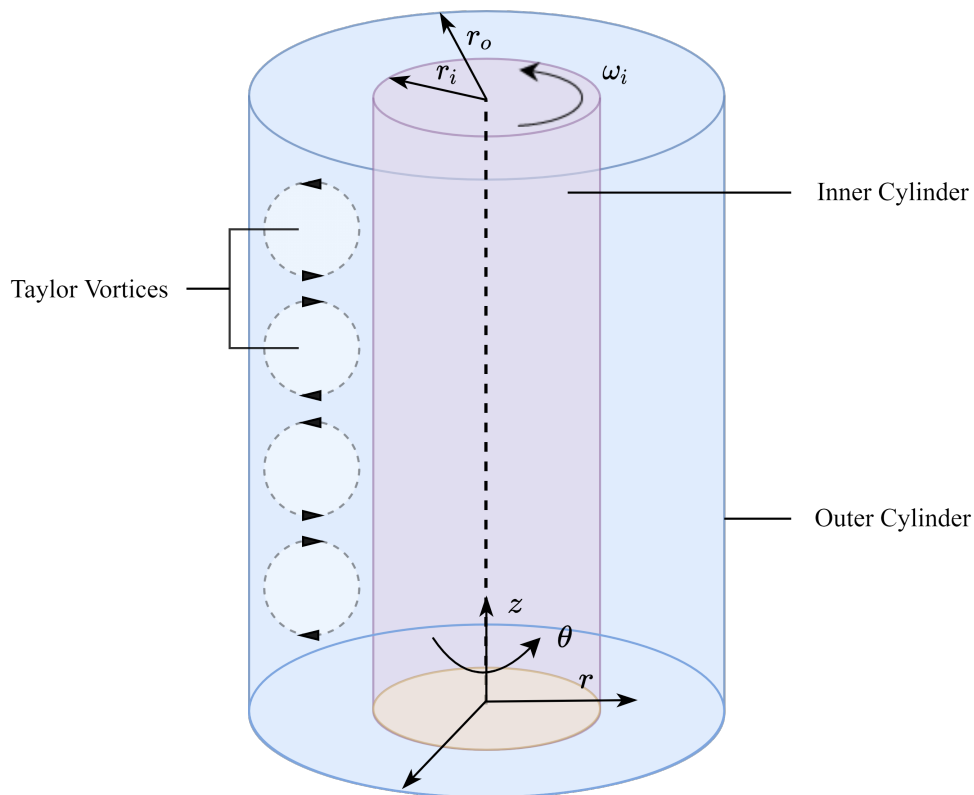


Figure 1.1: Schematic of Taylor-Couette flows and secondary vortices in the meridional plane.

T-C apparatus has been used in a variety of research interests, e.g., viscosity measurement

(Couette 1890), linear and non-linear hydrodynamic instabilities (Andereck *et al.* 1986; Di Prima and Swinney 1981; Taylor 1923) , transitions (Coles 1965; Topayev *et al.* 2022), steady and unsteady flow states and turbulence (Akonur and Lueptow 2003; Dutcher and Muller 2009; Grossmann *et al.* 2016). The behavior and pattern of the flow can vary greatly depending on multiple factors, including the rotational speed of both cylinders, the properties of the fluid, radius, and aspect ratio of the setup, which makes this problem complex and challenging.

### 1.2.1 Governing Equations

In this thesis, the velocity is defined in the Eulerian perspective. For clarity, symbols that are used in this thesis strictly follow the below notation. Italic letter denotes scalar quantity, e.g.,  $U$ . Italic bold letters represent vectors and tensors (e.g., velocity vector  $\mathbf{U}$ ). A vector described in terms of scalar quantity in the three-dimensional space is written in a form:  $\mathbf{U} = U_1\mathbf{e}_1 + U_2\mathbf{e}_2 + U_3\mathbf{e}_3$  , where  $\mathbf{e}$  is the unit vector, and the subscript  $i=1,2,3$  is the index of each different direction. In this study, given the Taylor-Couette rig geometry, cylindrical coordinate system is preferred, where the three-dimensional space is described by radial distance  $r$ , azimuthal angle  $\theta$ , and height  $z$ . Thus the velocity vector can be written as:  $\mathbf{U} = U_r\mathbf{e}_r + U_\theta\mathbf{e}_\theta + U_z\mathbf{e}_z$ . The conversion from Cartesian to Cylindrical coordinates is given in Appendix A.1).

In cylindrical coordinates, a general form of three-dimensional continuity equation is given by:

$$\frac{\partial \rho}{\partial t} + \frac{1}{r} \frac{\partial (\rho r U_r)}{\partial r} + \frac{1}{r} \frac{\partial (\rho U_\theta)}{\partial \theta} + \frac{\partial (\rho U_z)}{\partial z} = 0. \quad (1.1)$$

The Navier–Stokes equation in cylindrical coordinates of each direction can be expressed as follows:

$$\frac{\partial U_r}{\partial t} + \left[ (\mathbf{U} \cdot \nabla) U_r - \frac{U_\theta^2}{r} \right] = -\frac{1}{\rho} \frac{\partial p}{\partial r} + \nu \left[ \nabla^2 U_r - \frac{U_r}{r^2} - \frac{2}{r^2} \frac{\partial U_\theta}{\partial \theta} \right], \quad (1.2a)$$

$$\frac{\partial U_\theta}{\partial t} + \left[ (\mathbf{U} \cdot \nabla) U_\theta + \frac{U_r U_\theta}{r} \right] = -\frac{1}{\rho r} \frac{\partial p}{\partial \theta} + \nu \left[ \nabla^2 U_\theta - \frac{U_\theta}{r^2} + \frac{2}{r^2} \frac{\partial U_r}{\partial \theta} \right], \quad (1.2b)$$

$$\frac{\partial U_z}{\partial t} + (\mathbf{U} \cdot \nabla) U_z = -\frac{1}{\rho} \frac{\partial p}{\partial z} + \nu [\nabla^2 U_z]. \quad (1.2c)$$

Assumptions can be made to simplify the governing equations under certain circumstances, e.g., classic Circular Couette flow (CCF) assumes:

- Cylinders are infinitely long,
- Incompressible flow ( $\rho = \text{uniform}$ ,  $\frac{\partial \rho}{\partial t} = 0$ ),
- Axisymmetric ( $U_r = U_z = 0$ ,  $U_\theta = U(r)$ ,  $\frac{\partial}{\partial \theta} = 0$ ).

In this specific case, given the velocity is only a function of  $r$ ,  $U$  is used interchangeably with  $U_\theta$  below.

Under the above assumptions, all the terms in the continuity equation are canceled out, and the N-S equations in each direction can be reduced respectively to:

$$\frac{dp}{dr} = \frac{\rho U^2}{r}, \quad (1.3a)$$

$$\frac{d^2 U}{dr^2} + \frac{1}{r} \frac{dU}{dr} - \frac{U}{r^2} = 0, \quad (1.3b)$$

$$\frac{\partial p}{\partial z} = 0. \quad (1.3c)$$

The inner cylinder rotates at a constant angular velocity  $\omega_i$ , and the outer cylinder stays stationary. Thus the boundary conditions of this problem are:

$$U_\theta|_{r=r_i} = \omega_i r_i, \quad (1.4a)$$

$$U_\theta|_{r=r_o} = 0. \quad (1.4b)$$

Thus for circular (infinite-long cylinder) Couette flow, the analytical solution for azimuthal velocity exists and is given by:

$$U_\theta = U(r) = -\frac{r_i^2 \omega_i (r_o^2/r - r)}{r_o^2 - r_i^2}. \quad (1.5)$$

The torque acted on the inner cylinder could be obtained:

$$\mathbb{T}_z = \int_0^{2\pi} (\tau_{r\theta})_{r=r_i} r_i^2 d\theta = \frac{4\pi\mu r_i^2 r_o^2}{r_o^2 - r_i^2} \omega_i. \quad (1.6)$$

An estimation of torque for a finite long cylinder (length of cylinder  $l_c$ ):

$$\mathbb{T}_z = \int_0^{l_c} dz \int_0^{2\pi} (\tau_{r\theta})_{r=r_i} r_i^2 d\theta = \frac{4\pi\mu r_o^2 r_i^2}{r_o^2 - r_i^2} \omega_i l_c. \quad (1.7)$$

Note that Equation 1.7 is valid only for low Reynolds numbers, and the shear stress magnitude at the inner cylinder wall could be regarded as everywhere the same.

For Taylor-Couette turbulence, a time-averaged torque  $\langle \mathbb{T}_z \rangle_t$  can be calculated as (Huisman *et al.* 2013b):

$$\langle \mathbb{T}_z \rangle_t = 2\pi r_i^2 l_c \tau_{w,i}, \quad (1.8)$$

where  $\tau_{w,i}$  is the average inner wall shear stress, and  $l_c$  is the inner cylinder length.

## 1.2.2 Taylor-Couette Flow of Newtonian Fluids

In the late 18th and early 19th centuries, research was first conducted for Newtonian Taylor-Couette flow at low Reynolds numbers and onset instabilities. Couette (1890) first built Taylor-Couette type viscometer to investigate the effect of fluid viscosity on torque measurement. Taylor (1923) studied and reported the linear stability of Taylor-Couette flow theoretically. This leads to subsequent research on instability theory and generalization of the famous Rayleigh stability criterion (Esser and Grossmann 1996; Rayleigh 1917), which states that the T-C flow is linearly stable if the inner cylinder is fixed and the outer cylinder rotates only. In contrast, in cases where the inner cylinder rotates only and the outer cylinder is held stationary, the flow is linearly unstable due to force imbalance between driving

centrifugal forces and pressure gradient (Grossmann *et al.* 2016). In the unstable regime of T-C flow, a variety of flow regimes can be observed, such as Taylor vortices, wavy vortices, and featureless turbulence (Grossmann *et al.* 2016; Huisman *et al.* 2012).

The most frequently used configuration of the Taylor-Couette flow rig is to have the inner cylinder of radius  $r_i$  in rotation and the outer cylinder of radius  $r_o$  remain stationary. Hereafter discussion is limited to cases where only the inner cylinder rotates. The radius ratio  $\eta_r$  is defined as:

$$\eta_r = \frac{r_i}{r_o}. \quad (1.9)$$

The gap width between cylinders:

$$d = r_o - r_i. \quad (1.10)$$

The length of the cylinder  $l_c$  should be much larger than the gap width  $d$  to minimize the end effects from the top and bottom, thus the aspect ratio of the setup  $\zeta$  is given by:

$$\zeta = \frac{l_c}{d}. \quad (1.11)$$

$\zeta$  is usually much larger than 1 ( $\zeta \gg 1$ ). The velocity scale can be defined as:

$$U_{ref} = \omega_i r_i. \quad (1.12)$$

The Reynolds number for Newtonian fluid is defined as:

$$\text{Re} = \frac{\rho U_{ref} d}{\mu}, \quad (1.13)$$

where  $\rho$  is the fluid density,  $\omega_i$  is the angular the velocity of the inner cylinder and  $\mu$  is the constant dynamic viscosity of the Newtonian fluid.

Taylor-Couette flow exhibits a variety of flow regimes under different Reynolds numbers. At sufficiently low Re, Taylor-Couette flow is stable and laminar. The flow is purely axisymmetric and two-dimensional, with both radial velocity and axial velocity component

being zero (Topayev *et al.* 2022). This flow state is called Circular Couette Flow (CCF). As  $Re$  is increased, the system tends to be less stable. When Reynolds number is beyond the first critical value  $Re_{c,1}$ , the flow is characterized with stationary toroidal vortices (Taylor rolls/Taylor vortices) distributed along the axial direction (Cagney and Balabani 2019; Topayev *et al.* 2022). A pair of Taylor vortices in a vortex cell are counter-rotating and are separated by radial jets (Topayev *et al.* 2019). This flow regime is referred to as Taylor Vortex Flow (TVF). TVF is a time-independent process. As  $Re$  is increased further beyond  $Re_{c,2}$ , a second instability shows up resulting in an unsteady flow, with azimuthal traveling waves superimposed on the vortices (Cagney and Balabani 2019; Wereley and Lueptow 1998), which is referred to as Wavy Vortex Flow (WVF). This flow regime can be visually confirmed by a stack of closed cell vortices that undulate with identical phase (Akonur and Lueptow 2003; Wereley and Lueptow 1998). Wavy vortices were observed to have both axial and radial motions by PIV experiment (Wereley and Lueptow 1998). It was found that in the Wavy Vortex Flow (WV) regime, the strongest component velocity is in the azimuthal direction, the axial and radial velocities are more than an order of magnitude less than the maximum azimuthal velocity. This flow regime is characterized by a single temporal frequency and wavelength (Cagney and Balabani 2019). Keep increasing  $Re$  leads to more instabilities getting into the system, and the flow is characterized by the presence of two modulated waves with different rotation frequency (Akonur and Lueptow 2003; Andereck *et al.* 1986; Brandstater and Swinney 1987; Shaw *et al.* 1982). The subsequent increase of  $Re$  leads to the Turbulent Taylor Vortex flow (TTV).

The Reynolds number discussed above is limited in the range that is less than the estimation of the onset of turbulence  $Re \sim 1000$  (Brandstater and Swinney 1987; Lathrop *et al.* 1992). High  $Re$  number Taylor-Couette turbulence has been explored in the last few decades. Global response parameters of Taylor-Couette system (e.g., dimensionless torque  $G$ , Taylor number  $Ta$ , angular velocity flux  $J^\omega$ , and Nusselt number  $Nu_\omega$ , etc.) are defined and studied. Efforts to find the dependence between parameters are made by many researchers (Grossmann *et al.* 2016; Lathrop *et al.* 1992). Lathrop *et al.* (1992) studied Reynolds numbers

ranging over  $800 < \text{Re} < 1.23 \times 10^6$  and the experimental results showed that there is no fixed power law for torque scaling with Reynolds number. This conclusion is also verified and reported by other researchers (Eckhardt *et al.* 2007; Lewis and Swinney 1999; Van Gils *et al.* 2011). Van Gils *et al.* (2011) experimentally investigated strong turbulent regimes at  $\text{Re}_i = 2 \times 10^6$  and found a universal scaling law between dimensionless torque  $G$  and Taylor number. Nusselt number  $Nu_\omega$ , which is defined to characterize the relative ratio of the turbulent angular velocity  $J^\omega$  and its laminar case  $J_{\text{lam}}^\omega$  (Bodenschatz *et al.* 2000), is found to be dependent with Ta. This is the most relevant relationship that has been found between global responses (Van Gils *et al.* 2011).

Numerical simulation research has also provided insights into understanding the complex behavior of the flow. Numerical study of Taylor-Couette flow has its particular advantage in terms of visualization in T-C study, for it is not limited by the curved surface of the flow rig, which causes light distortion and refraction.

A substantial quantity of numerical simulation work has provided visual observation of Taylor vortices in a variety of flow states, from TVF to turbulent flow (Andereck *et al.* 1986; Coles 1965; Parker and Merati 1996). Thus Taylor vortices are believed to exist and remain visible in a wide range of Re, the Taylor vortices are considered the primary coherent structures in T-C turbulence. An interesting result by Dong (2007) with 3D direct numerical simulation (DNS) showed the existence of Taylor vortices underlying turbulent fluctuations at a very high  $\text{Re} = 8000$ . Parker and Merati (1996) reported Taylor vortex motion at even higher  $\text{Re} = 73000$ . Ostilla-Mónico *et al.* (2014) investigated the Taylor-Couette turbulence by using DNS up to inner cylinder Reynolds numbers of  $\text{Re}_i = 10^5$ . Taylor number was defined as  $\text{Ta} = 1/4\sigma (r_o - r_i)^2 (r_o + r_i)^2 \omega_i^2 \nu^{-2}$ , where  $\sigma$  is a geometrical Prandtl number that is dependent on the individual apparatus used. It was shown that at relatively small Taylor numbers ( $\text{Ta} \sim 10^6$ ), Taylor vortices are developed. They are the dominant coherent structures occupying the gap. The length scale of the coherent structures decreases as increasing Ta (Grossmann *et al.* 2016; Ostilla-Mónico *et al.* 2014), and small-scale coherent motion becomes more significant and is observed to co-exist with large-scale

coherent structures (Barcilon and Brindley 1984). The small-scale coherent structures are referred to as Görtler vortices (GV) (Dong 2007), which occurs only at the near wall region with a much smaller lengthscale (Bilson and Bremhorst 2007).

The boundary layer also changes as Re or Ta varies. Under  $Ta = 3 \times 10^6$ , the classical regime of turbulence is obtained, where turbulence starts to develop in the bulk at length-scales between the Kolmogorov and the integral scale and larger. Meanwhile laminar type of boundary layers (BLs), also known as Prandtl-Blasius BLs, is developed at the inner and outer cylinders (Huisman *et al.* 2013b). If Ta exceeds the critical value  $Ta^*$  ( $Ta^* \approx 3 \times 10^8$  for  $\eta_r = 0.71$ ), the boundary layer is sheared strongly and becomes turbulent boundary layer, i.e., Prandtl–von Karman boundary layer. This regime is referred to as the ultimate turbulence regime (Huisman *et al.* 2012). In a recent study by Huisman *et al.* (2013b) who investigated the properties of turbulent logarithmic boundary layers at Re up to  $2 \times 10^6$  (ultimate turbulence regime), it was found that the mean azimuthal velocity  $U_\theta$  profile of turbulent boundary layer can be fitted by the von Kármán log law of wall:

$$U_\theta^+(r^+) = \kappa^{-1} \log r^+ + B, \quad (1.14)$$

where  $r^+$  is the dimensionless distance against the wall,  $B$  is the logarithmic intercept, and  $\kappa$  is von Kármán constant which is dependent on Taylor number Ta. For Ta is large enough,  $\kappa$  was found close to 0.4 which is the classic fitting constant for fully developed turbulence. This conclusion coincides with previous investigation by Lathrop *et al.* (1992), who concluded that the boundary layer turbulence of T-C flow shares similarity with flat wall boundary layer turbulence.

### 1.2.3 Taylor-Couette Flow of Shear-thinning Fluids

A unique Reynolds number for a given flow situation requires a constant and uniform viscosity, which does not exist for non-Newtonian fluids. Different definitions of the effective Reynolds number have been used (Agbessi *et al.* 2015; Cagney and Balabani 2019; Elçiçek and Güzel 2020; Topayev *et al.* 2019). The most common definition of Reynolds number for

the non-Newtonian fluid is based on the nominal shear rate  $\dot{\gamma}_{\text{nom}}$  :

$$\dot{\gamma}_{\text{nom}} = \frac{\omega_i r_i}{d}, \quad (1.15)$$

which leads to the definition of nominal Reynolds number:

$$\text{Re}_{\text{nom}} = \frac{\rho \omega_i r_i d}{\mu|_{\dot{\gamma}=\dot{\gamma}_{\text{nom}}}}. \quad (1.16)$$

Note in the present study, the above definition of Reynolds number is adopted for non-Newtonian fluids, and  $\text{Re}$  is used interchangeably with  $\text{Re}_{\text{nom}}$  for non-Newtonian fluids.

Another definition of Reynolds number  $\text{Re}_{cw}$  could be defined based on inner wall shear viscosity  $\mu|_{r=r_i}$ , as shown in Equation 1.17 below:

$$\text{Re}_{cw} = \frac{\rho \omega_i r_i d}{\mu|_{r=r_i}}. \quad (1.17)$$

Based on this definition, it is observed that shear-thinning effects delays the appearance of the Taylor vortices for all radius ratio  $\eta_r$ , which is attributed to the energy exchange reduction between base and perturbation (Alibenyahia *et al.* 2012).

A major difference between Newtonian and shear-thinning Taylor-Couette flow is the viscosity stratification in the spatial domain prior to the onset of secondary flow. This leads to different velocity profiles and flow patterns. Shear-thinning fluids, in general, are found to modify several aspects of Taylor-Couette turbulence: flow regimes, transition, velocity distribution, as well as the size, locations, and vorticity magnitude of Taylor vortices. Experimentally, Escudier *et al.* (1995b) found that the transition from CCF to TVF of Newtonian fluids is an abrupt process that could be identified, whereas the transition from CCF to TVF of non-Newtonian fluid is a gradual process, which is reflected by the observation of a slow and steady increment of the radial velocity component. Elçiçek and Güzel (2020) discussed the shear-thinning flow structures under a variety of  $\text{Re}_{cw} \approx 100 - 1000$ . Interestingly, two additional non-axisymmetric flow states, namely spiral vortex flow (SVF) and ribbons (RIB) are found between CCF and TVF states, whereas the wavy vortex flow (WVF) is bypassed in

the transition from Taylor Vortex Flow (TVF) to Modulated Wavy Vortex Flow (MWVF). The result also shows that the magnitude of mean radial velocity of the inward jets is less than the amplitude of the outward jets. This conclusion is also reported by other researchers (Cagney and Balabani 2019; Nemri *et al.* 2016; Wereley and Lueptow 1998).

Newtonian and non-Newtonian Taylor-Couette flows have been compared and interesting phenomena have been observed. Cagney and Balabani (2019) investigated a wide range of  $Re$  from 150 – 1000 with a combination of planar PIV and flow visualization technique, the findings showed that compared to a Newtonian fluid, shear-thinning behavior was linked to an expansion of vortex wavelength (Bahrani *et al.* 2015), reduction of vorticity and strength of outward jet. This observation is coincident with DNS studies of wall-bounded homogeneous, isotropic turbulence (Pandit *et al.* 2009; Perlekar *et al.* 2006). Vortex drift along axial direction was observed specifically in shear-thinning cases, however, no axial drift was observed in Newtonian case (Cagney and Balabani 2019; Elçiçek and Güzel 2020; Escudier *et al.* 1995b; Topayev *et al.* 2019). Escudier *et al.* (1995a) investigated the Taylor-Couette flow of shear-thinning fluid with xanthan gum solution at a concentration of 1500 ppm (parts per million) and the aqueous solution of Laponite. It was found that shear-thinning effects cause the vortex eye to move significantly in the radial direction. Taylor vortices in shear-thinning fluids distribute asymmetrically in a vortex pair both radially and axially. Due to the larger shear-thinning effects (lower effective viscosity) occur at the inner cylinder, the vortices tend to locate closer to the near wall region of the inner cylinder in radial direction (Agbessi *et al.* 2015). Similarly, in the axial direction, the vorticity was found to concentrate closer to the radial outward jet where the shear rate is higher (Cagney and Balabani 2019).

### 1.3 Polymers and Polymeric Flows

Polymeric fluids are widely used in various industrial processes due to their unique properties such as elasticity and non-Newtonian behavior Fried (2014). The engineering applications of polymers and polymeric flows are numerous and diverse, such as in the design of pipelines for transporting crude oil or natural gas (Al Christopher *et al.* 2021). The use of polymeric

solutions in pipeline transportation can reduce the drag and energy losses associated with turbulent flow, leading to more efficient and cost-effective transport (Dimitropoulos *et al.* 1998; Kim *et al.* 2007; Sureshkumar *et al.* 1997). In addition to pipeline transportation, polymeric solutions are used in the design of medical devices, such as catheters and stents (Annabi *et al.* 2013; Astaneh *et al.* 2009), where the viscoelastic properties of the fluid can be tailored to achieve specific mechanical properties. Polymeric solutions are also used in the production of food and consumer products, where the rheological properties of the fluid can be adjusted to improve product quality and consistency while using edible or consumable additive polymers. Overall, the presence of polymers can significantly alter the flow characteristics, leading to complex phenomena such as drag reduction (Housiadas and Beris 2003; Thirumalai and Bhattacharjee 1996), turbulence modulation or control (De Angelis *et al.* 2005; Fu and Kawaguchi 2013), and flow instability (Graham 2004; Samanta *et al.* 2013).

### 1.3.1 Classification of Polymers and Polymer Solutions

The classification of polymers could be based on their molecular structure, thermal processing behavior, chemical resistance, and mechanism of polymerization (Fried 2014).

Based on the molecular structure, polymers can be divided into two primary categories: flexible or rigid polymers (Afshari *et al.* 2008). Flexible polymers are characterized by molecular structures that allow for significant conformational changes in response to external stimuli, such as temperature (Schnurr *et al.* 1997) or shear (LeDuc *et al.* 1999; Lee *et al.* 2008). Mechanical degradation could occur for flexible polymers when they are subjected to mechanical stresses such as stretching, compression, and bending, which is a major concern in engineering applications (Azadi and Nobes 2022; Mitishita *et al.* 2023; Pereira *et al.* 2013). These motions can cause changes in the molecular weight structure of polymers, leading to a reduction in the mechanical properties and performance over time (Abdel-Alim and Hamielec 1973). Rigid polymers are long-chain molecules that resist deformation under flow conditions due to their high tensile strength and stiffness. They are less prone to mechanical degradation

compared to flexible polymers (Mitishita *et al.* 2023). Most biopolymers, e.g., xanthan gum (XG) (Pereira *et al.* 2013; Rochefort and Middleman 1987), diutan gum (Santos *et al.* 2020), starch, cellulose nanocrystals, pineapple fibers (Bhambri *et al.* 2017) and glycogen have rigid structure and are classified as rigid polymers.

Polymer solutions can be classified into two categories in terms of rheological behavior: Newtonian and non-Newtonian behavior. Newtonian behavior refers to the behavior of fluids that exhibit a constant viscosity regardless of the applied stress or shear rate. In contrast, non-Newtonian behavior refers to fluids that exhibit a changing viscosity as a function of shear stress or shear rate. Non-Newtonian fluids can exhibit more complex and interesting behavior compared to Newtonian fluids and are often used in various industrial applications. However, the complexity of the fluid behavior in non-Newtonian flow can also make it more difficult to analyze and predict. The biggest challenge characterizing flows with fluids of variable viscosity is that universal Reynolds number scaling is not possible.

### 1.3.2 Viscoelasticity

Polymers exhibit both viscous and elastic behavior. Viscous behavior refers to the resistance to deformation, and elastic behavior refers to the ability to deform and return to the original shape once the force is removed. When polymer is added to a liquid, the polymer chains undergo conformational changes and begin to unravel and entangle with each other. The entangled polymer network gives rise to both viscous and elastic properties in the solution. The viscosity is due to the resistance of the polymer chains sliding past each other, while the elasticity results from the ability of the entangled chains to spring back to their original positions when deformed. Polymers can also be classified into shear-thinning and shear-thickening fluids, whose viscosity reduces or increases under applied stress or strain rate. These behaviors make polymeric solutions useful in various applications, such as in the petroleum industry for enhanced oil recovery, as thickeners in food products, and in cosmetics and pharmaceuticals (Herth *et al.* 2000).

### 1.3.3 Drag Reduction

One reason that polymers received great attention is the phenomenon of drag reduction (DR) in turbulent flows (White and Mungal 2008). A small quantity of polymer additives can lead to a significant decrease in energy dissipation and friction loss in turbulent flows (Dimitropoulos *et al.* 1998; Min *et al.* 2003; Virk 1975; Xi 2019). Virk (1975) found that the addition of small amounts of polymers resulted in significant drag reduction in pipe flow turbulence, with a maximum reduction of 80% observed, and maximum drag reduction (MDR) asymptote was first proposed to illustrate the observation that skin friction has converged to a level lying between the magnitudes of Newtonian laminar flow and turbulence. Interestingly, drag reduction is a phenomenon that only occurs in turbulence. It is argued that turbulence induces significant increase in extensional viscosity which is necessary for the occurrence of drag reduction (Dimitropoulos *et al.* 1998).

Abundant studies are available that investigated the effect of polymer on drag reduction and turbulent structures. Mohammadtabar *et al.* (2017) investigated the turbulent structures in a channel flow at  $Re = 7200$  by using xanthan gum solutions at different concentrations from 75-125 ppm. Xanthan gum solutions are shear thinning but their apparent viscosity increases with increasing xanthan gum concentration. It was found that as the concentration of polymer increases, the boundary layer moves further away from the wall, and at MDR, wall-normal Reynolds stresses and Reynolds shear stresses are significantly attenuated. Sureshkumar *et al.* (1997) used direct numerical simulation to investigate the effects of polymers on turbulent drag reduction in a channel flow, and it was shown that the effect of drag reduction is associated with a decrease in the streamwise vorticity fluctuations and an increase in the streak spacing within the buffer layer. This result is also reported by other researchers (Mohammadtabar *et al.* 2017; Nieuwstadt and Den Toonder 2001; Tiederman 1990). Kim *et al.* (2007) studied the near-wall turbulent structures in fully-developed turbulent channel flow with polymers. It was found that as Weissenberg number  $We$  (ratio of the polymer relaxation time to the flow time scale) increases (indicative of an increase in

DR), the root mean square (r.m.s.) of the streamwise velocity fluctuations decrease at very near wall region (around  $0 < y^+ < 20$ ) but increases further away from the wall ( $y^+ \geq 20$ ). However, the r.m.s. of the wall-normal and spanwise direction velocity fluctuations decrease throughout the entire channel. This coincides with previous experimental results (Luchik and Tiederman 1988). It was also found that the addition of polymers results in a reduction of turbulence kinetic energy production and dissipation across the channel (Dimitropoulos *et al.* 1998).

The research in the discussion above has provided numerical and experimental support to the understanding of drag reduction mechanisms. Several kinds of DR mechanisms have been reported. A possible mechanism responsible for DR is the viscous theory (Lumley 1969), which suggested that turbulent structures are suppressed as the polymer molecules are stretched, leading to an increase in extensional viscosity, which ultimately results in drag reduction. It is observed that increasing extensional viscosity leads to dampening small-scale eddies and inhibits the production of vortices (Thais *et al.* 2010). Dimitropoulos *et al.* (1998) investigated the streamwise vorticity in a turbulent viscoelastic channel flow. Reduction of streamwise vorticity was found to be due to the enhancement of extensional viscosity. This is consistent with the proposed viscous theory. Another mechanism to explain DR is elastic theory (De Gennes 1986), which postulates that the presence of polymers introduces a remarkable effect on decreasing the turbulent velocity fluctuations at small scales. This phenomenon arises due to the inherent elasticity of the polymer flows, which plays a crucial role in dampening the turbulence. As turbulent motion occurs at increasingly smaller scales, the flexible nature of the polymers allows them to interact with the turbulent eddies, absorbing some of the energy and dissipating it in the process. Consequently, this polymer-induced damping effect leads to a smoother and more subdued turbulence behavior at the smaller scales compared to scenarios without polymer presence. Turbulent energy is stored as elastic energy in partially stretched polymers, the elastic energy gets accumulated at the very near wall region, and transported and released in the buffer layer and log layer (Min *et al.* 2003). In elastic theory, it is argued that the elasticity effect is dominant, whereas

the increase in the extensional viscosity is insignificant to DR.

### 1.3.4 Turbulent Polymeric Boundary Layer

For Newtonian fully developed turbulence, the law of the wall and log law scaling is given for mean wall-parallel velocity which is valid in viscous sublayer and logarithmic layer respectively:

$$U^+ = y^+, y^+ < 5, \quad (1.18)$$

$$U^+ = \frac{1}{\kappa} \ln y^+ + B, y^+ > 30, \quad (1.19)$$

where  $\kappa$  is von Kármán constant,  $B$  is the logarithmic intercept. It was found  $\kappa = 0.4$  and  $B = 5$  for a fully developed channel flow (Kim *et al.* 1987).

Despite different proposed mechanisms for drag reduction, in polymeric turbulence, the thickness of the boundary layer was found to be larger than Newtonian flows. Virk and Smith (1970) and Virk (1975) determined the mean wall-parallel velocity profile of drag-reduced polymer flows. Drag-reduced scaling law was proposed and the boundary layer was divided into three wall-normal zones: viscous sublayer, elastic (interactive) sublayer, and Newtonian (log-law) plug zones. A schematic is shown in Figure 1.2 below with adding data from several researchers (Azadi 2023; Rollin and Seyer 1972; Rudd 1972; Virk 1975).

Virk and Smith (1970) proposed the ultimate mean velocity profile at theoretical maximum drag reduction that a polymeric flow could reach Virk’s MDR asymptote:

$$U^+ = 11.7 \ln(y^+) - 17.0, \quad y^+ > 30. \quad (1.20)$$

From Figure 1.2, it can be observed that experimental data within the linear viscous sublayer coincides with the law of the wall. The velocity profile started to deviate from the intersection point of Newtonian log law and Newtonian law of the wall. The dimensionless distance of the intersection point to the wall is  $y^+ = 11.45$ . The interactive sublayer is thickened compared to

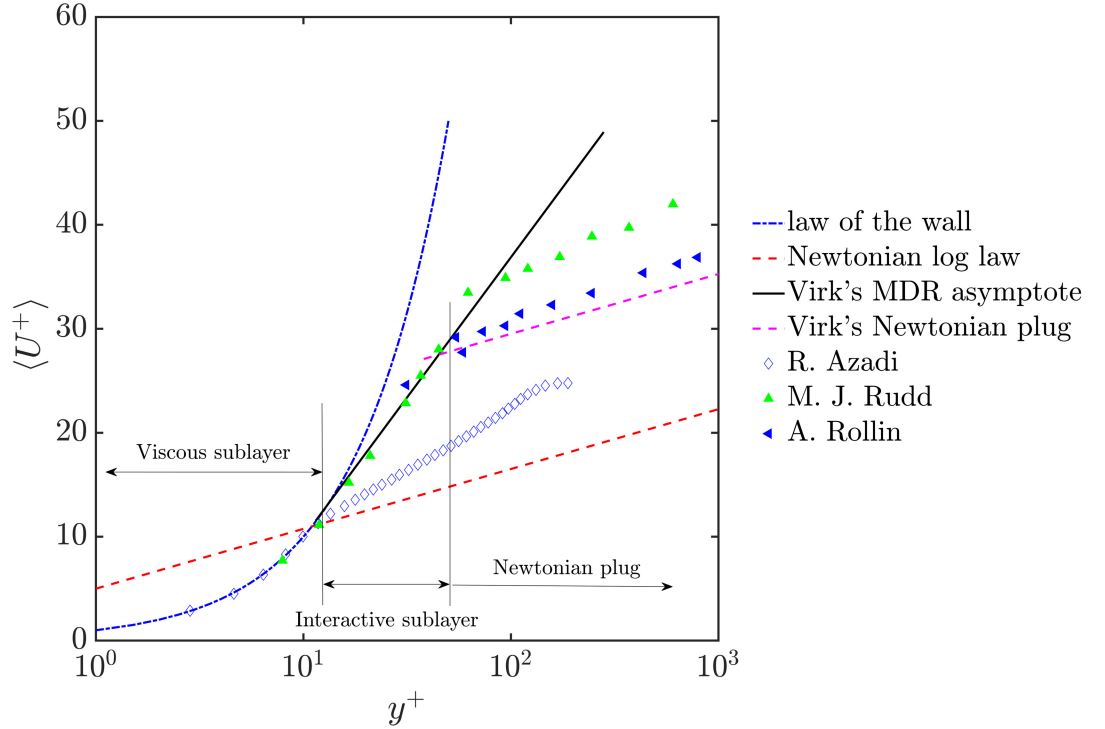


Figure 1.2: Plot of mean velocity profiles of turbulent polymeric flows.

the Newtonian log law and the mean velocity profile showed a larger slope, which indicates the logarithmic region is pushed further away. Verk proposed another asymptote to describe the velocity profile of polymer flows in Newtonian log law plug region by shifting the Newtonian log law upwards by a constant  $c_1^+$ , which is the value of intercept of Newtonian's plug profile on the  $y$ -axis higher than the common Newtonian logarithmic intercept  $B$ .

## 1.4 Ensemble Mean, Fluctuation, and Variances

The ensemble average denotes the arithmetic average of a random variable computed across  $N$  realizations, with each realization is an independent event (George 2013). In turbulence, the velocity is often described as a random variable and the mean behaviour of velocity is of interest (Aliabadi 2022). The true ensemble average of velocity is given by:

$$\langle U \rangle \equiv \lim_{N \rightarrow \infty} \frac{1}{N} \sum_{n=1}^N U_n, \quad (1.21)$$

where  $\langle \rangle$  denotes the expected mean of a random variable, and  $N$  is the number of realizations of independent experiment. The true ensemble mean  $\langle U \rangle$  cannot be obtained, since infinite number of independent realizations of measurement is unable to achieve experimentally. However, the ensemble average of velocity based on finite number of samples can be obtained (denoted by  $\langle U \rangle_N$ ) and is often used as an estimator for the true mean. The  $\langle U \rangle_N$  is given by:

$$\langle U \rangle_N = \frac{1}{N} \sum_{n=1}^N U_n. \quad (1.22)$$

Alternatively, time averaging technique has been introduced to obtain a mean value for the estimation of true ensemble average based on finite time range, the mean velocity by time averaging for a statistically stationary process is given by:

$$\langle U \rangle_t \equiv \frac{1}{T} \int_0^T U(t) dt. \quad (1.23)$$

In this thesis, the ensemble samples were collected over time physically in one realization, but the velocity fields were considered independent samples. It has been proven that under certain conditions, time averaging can be the same as ensemble average (George 2013), as will be discussed in subsequent chapter.

The fluctuation of velocity based on ensemble average is defined as:

$$u = U - \langle U \rangle_N, \quad (1.24)$$

The variance of velocity, i.e, the ensemble average of the square of the fluctuation  $\text{var}(U)$  or  $\langle u^2 \rangle$  thus is given by:

$$\langle u^2 \rangle = \lim_{N \rightarrow \infty} \frac{1}{N} \sum_{n=1}^N [U_n - \langle U \rangle]^2. \quad (1.25)$$

An unbiased estimator for variance with finite number of samples adopted in the current study is given by:

$$\langle u^2 \rangle_N = \frac{1}{N-1} \sum_{n=1}^N [U_n - \langle U \rangle_N]^2. \quad (1.26)$$

## 1.5 Energy Cascade

The energy cascade refers to turbulence kinetic energy transferred from large scales of motion to smaller scales in turbulence. Based on Kolmogorov's hypothesis of local isotropy (Pope 2001), turbulence can be considered statistically isotropic if lengthscale of structures  $l \ll l_0$ , where  $l_0$  is the characteristic lengthscale of a flow. A distinctive lengthscale  $l_{EI} \approx 1/6l_0$  was thus introduced to separate the energy-containing range (where the turbulence is considered locally anisotropic) and universal equilibrium range (where the turbulence is considered isotropic). The lengthscale of the energy-containing range is estimated to be in the range of  $1/6l_0 \leq l \leq 6l_0$ , where most of the energy is contained. Universal equilibrium range can be subdivided further into dissipation range and inertial subrange, with a demarcation lengthscale of  $l_{DI}$ . According to Kolmogorov's second hypothesis, statistics are only dependent on dissipation rate  $\varepsilon$  whereas independent of kinematic viscosity  $\nu$  in the inertial subrange. The energy spectrum of the inertial subrange is given by the form:

$$E(\kappa) = C\varepsilon^{2/3}\kappa^{-5/3}, \quad (1.27)$$

where  $E(\kappa)$  is energy per wavenumber,  $C$  is a dimensionless constant, and  $\varepsilon$  is the rate of energy dissipation per unit mass. It is noteworthy to mention that this hypothesis is based on the assumption that the only relevant parameters in the inertial subrange are  $\varepsilon$  and  $k$ , and that the flow is statistically homogeneous and isotropic.

The energy dissipation is the process by which the kinetic energy is dissipated into heat by viscous effect. The dissipation rate  $\varepsilon$  is given by:

$$\varepsilon = 2\nu \langle S_{ij}S_{ij} \rangle, \quad (1.28)$$

where  $\nu$  is the kinematic viscosity, and  $S_{ij}$  is the fluctuation of strain rate tensor.  $S_{ij}$  is defined as:

$$S_{ij} = \frac{1}{2} \left( \frac{\partial u_i}{\partial x_j} + \frac{\partial u_j}{\partial x_i} \right), \quad (1.29)$$

where  $u_i$  is the velocity fluctuation component in the  $i$ -th direction. The dissipation is related to the smallest lengthscale of motions in turbulence, known as Kolmogorov scales, which are defined as:

$$\eta = \left( \frac{\nu^3}{\varepsilon} \right)^{1/4}, \quad (1.30a)$$

$$\tau_\eta = \left( \frac{\nu}{\varepsilon} \right)^{1/2}, \quad (1.30b)$$

$$u_\eta = (\nu\varepsilon)^{1/4}, \quad (1.30c)$$

where  $\eta$  is the lengthscale,  $\tau_\eta$  is the timescale, and  $u_\eta$  is the velocity scale of the smallest eddies where viscous dissipation is dominant.

From the discussion above, it can be seen that turbulence is characterized by different scales both in time and space. The energy contained at different scales is different. The velocity spectrum is introduced to describe how the kinetic energy of the flow is distributed among different scales of motion (Pope 2001). The velocity spectrum is given by:

$$\Phi_{ij}(\boldsymbol{\kappa}) = \frac{1}{(2\pi)^3} \iiint_{-\infty}^{\infty} R_{ij}(\mathbf{r}) e^{-i\boldsymbol{\kappa}\cdot\mathbf{r}} d\mathbf{r}, \quad (1.31)$$

where  $R_{ij}$  is the two-point correlation that describes the correlation between velocity fluctuations at two points separated by distance  $r$  :

$$R_{ij}(\mathbf{r}, t) = \langle u_i(\mathbf{x}, t) u_j(\mathbf{x} + \mathbf{r}, t) \rangle. \quad (1.32)$$

It can be seen from Equation 1.31 that  $\Phi_{ij}$  and  $R_{ij}$  form Fourier transform pairs.

$\Phi_{ij}$  carries directional information since  $\boldsymbol{\kappa}$  is a vector quantity. Since in practice, we might be more interested in how much energy is distributed at each scale but not in the direction the energy is flowing, the energy spectrum was introduced to remove the directional information:

$$E(\kappa) = \iiint_{-\infty}^{\infty} \frac{1}{2} \Phi_{ii}(\boldsymbol{\kappa}) \delta(|\boldsymbol{\kappa}| - \kappa) d\boldsymbol{\kappa}, \quad (1.33)$$

where  $\delta$  is Dirac delta function, and  $\kappa$  is an independent variable defined as the norm of vector  $\boldsymbol{\kappa}$ :

$$\kappa = \|\boldsymbol{\kappa}\|. \quad (1.34)$$

The dissipation rate is given by:

$$\varepsilon = \int_0^{\infty} D(\kappa) d\kappa, \quad (1.35)$$

where  $D(\kappa)$  is the dissipation spectrum that describes how energy dissipation is distributed among different lengthscales:

$$D(\kappa) = 2\nu\kappa^2 E(\kappa). \quad (1.36)$$

## 1.6 Application of Proper Orthogonal Decomposition in Turbulence

Proper Orthogonal Decomposition (POD) is a technique that aims to identify and represent the coherent structures that dominate the energy content of turbulent flows. The POD can be seen as similar to Fourier decomposition, which represents a function as a linear combination of orthogonal sinusoidal functions. The POD, however, does not use a fixed set of basis functions, but rather adapts them to the data, such that they optimally capture the variance or energy of the data (Brunton and Kutz 2022), so they are like a spatial principle component of variance analysis.

Lumley (1967) first introduced POD and related it to the analysis of turbulent flows. The advantage of POD is that it is available for highly non-linear dynamic systems, and is able to extract the shape of dominant features from the system. Fundamentally, this method is able to decompose non-homogeneous fluctuation fields, such as fluctuating velocity, pressure or vorticity fields, into a set of orthogonal empirical functions, i.e., POD modes. These POD modes are usually associated with the fluctuation patterns that correspond to the coherent structures that contribute to most of the energy in the flow. For example, when applying POD to the velocity fluctuation field, the resulting POD modes provide optimal decomposition in terms of turbulence kinetic energy (TKE) (Vitkovicova *et al.* 2020). This approach enables the concise representation of fluctuating fields as linear combinations in terms of the most energetic modes. The spatial modes are often interpreted into different motions in turbulence. In wall-bounded flows, POD is applied to identify wall-attached POD eddies and wall-detached POD eddies, which are the prime statistical representations of eddy motions near the wall (Wang *et al.* 2022a; Wang *et al.* 2022b). In the turbulent boundary layers study, the first mode captures ejection or sweep motion, and the second mode captures the shear-layer structures (Mohammadtabar *et al.* 2017).

POD application to turbulent flows primarily highlights the dominance of the first few modes, corresponding to large-scale coherent structures (Khan *et al.* 2021; Muralidhar *et al.* 2019; Smith *et al.* 2005; Wu *et al.* 2019). POD orders the principle components of the velocity fluctuations in descending order, into shapes which cover the contributions to the total fluctuation field. Usually, the first several modes will describe the vast majority of the energy in the fluctuation field, thus for most of the cases, the energy convergence is fast. However, some exceptions to this tendency are reported in the literature. Rovira *et al.* (2021) performed POD on large eddy simulations of counter-flowing jets and the result shows that more than 50 modes are needed to capture 70% of the turbulence kinetic energy. Kostas *et al.* (2005) attributed the poor convergence to the large variety of scales in turbulence. For flow with a wide variety of lengthscales, it will take more modes to capture and reconstruct the features.

In summary, the POD has been applied to various types of turbulent flows, such as channel flows, boundary layers, wakes, jets, mixing layers, and bluff body flows, etc. POD has also been combined with other methods, such as Galerkin projection (Hijazi *et al.* 2023), balanced truncation (Rowley 2005), dynamic mode decomposition(DMD) (Wu *et al.* 2019), and machine learning, to enhance its performance and capabilities. POD remains one of the most widely used and powerful methods for the analysis and modeling of turbulent flows, and continues to inspire new developments and applications in fluid dynamics.

## 1.7 Stereoscopic PIV Measurement Technique

Stereoscopic Particle Image Velocimetry (Stereo-PIV/SPIV) is an advanced optical technique for non-intrusive, quantitative measurement of fluid flow velocity fields in three dimensions (Prasad 2000). It provides a more comprehensive and accurate understanding of the flow behavior compared to traditional two-dimensional (planar) PIV techniques. Stereo-PIV configuration consists of two cameras focusing on a single object plane. Three velocity components in total can be obtained (two in-plane components and one out-of-plane component). The two velocity components within the object plane (laser plane) are referred to as in-plane velocity components. It has been found that in-plane components are biased when using a single camera (planar-PIV) configuration due to perspective errors, which are not present in a Stereo-PIV configuration Kähler (2004). Particle images are captured simultaneously from two different viewing directions, and the out-of-plane velocity component can be reconstructed based on the disparity in what cameras capture from two viewing perspectives.

Stereo-PIV configuration can be classified based on the camera position relative to the light sheet (Kähler 2004). Backward Forward-scattering is an SPIV configuration in which one camera captures the light that is scattered forwardly, while the other camera captures the light that is scattered backwardly. Following the same concept, there are Forward Forward and Backward Backward-scattering arrangements.

On top of the classification above, the arrangements of Stereo-PIV could be classified into the translation method and angular displacement method based on the relative angle

between the lens plane and object plane. With the translation method, the light-sheet plane, the main plane of the lens, and the image plane are all parallel to each other. The translation method offers a constant magnification across the field of view and ensures particles are in focus, but it has limitations in angular aperture and modulation transfer function, which lead to a limited FOV (Raffel *et al.* 1998).

The angular displacement method performs better with larger stereo opening angles and has a better modulation transfer function, however it has a varying magnification and perspective distortions which will require additional calibration (Kähler 2004). Typically, the angular displacement method is more often implemented in experiments; this allows for larger FOV. The object plane, lens plane, and image plane for each camera need to be set to converge to a single line of intersection, which is referred to as the Scheimpflug criterion (Hinsch 1995; Raffel *et al.* 1998; Royer and Stanislas 1996). Scheimpflug adapters are used in this configuration which allows tilting the the camera lens relative to the camera body with an angle to adjust the plane of focus back to the object plane. In the experiment, this will lead to a larger focused range so that all dots on the calibration target can be adjusted in focus. For SPIV calibration, small apertures are typically preferred to have a larger depth of field (Prasad and Jensen 1995).

## 1.8 Objectives and Hypothesis

The present study aims to investigate and characterize turbulent structures of shear-thinning polymers in a Taylor-Couette flow geometry and examine different nonlinear shear-thinning viscosity effects on turbulent statistics, energy spectra, and coherent motions under the same  $Re$  compared to the Newtonian fluid. Several hypotheses are made below:

It was hypothesized that (1) shear-thinning polymers could change the turbulent structures in the bulk flow in the Taylor-Couette annulus, which leads to changes in turbulent statistics, (2) the nonlinear effects induced by the viscosity of the non-Newtonian fluid alters the flow regimes and reshaped the evolving vortical structures, (3) shear-thinning polymers could affect the coherent motions and structures of T-C turbulence, and (4) shear-thinning

polymers could affect the turbulence kinetic energy transport in terms of energy containment and dissipation rate, and therefore change the energy cascade.

The main objectives of the research were to (1) to develop an experimental T-C setup which could obtain a dataset of two dimensional - three components (2D-3C) turbulent velocity fields of high accuracy, (2) to investigate the different nonlinear shear-thinning viscosity effect on turbulent structures, and (3) to elucidate the shear-thinning effects in terms of TKE and dissipation distribution at different lengthscales.

## 1.9 Thesis Outline

This thesis comprises 5 Chapters and 4 Appendices which are organized as follows:

Chapter 1 provides a literature review of Newtonian and non-Newtonian Taylor-Couette flow turbulence, and the background knowledge including the mathematical and experimental tools for turbulence investigations.

Chapter 2 provides a detailed overview of the Taylor-Couette apparatus, including the components of the designed T-C flow rig, SPIV configuration, and optical imaging settings. The accuracy and uncertainty analysis of the measurements are conducted and explained in detail.

Chapter 3 provides an analysis of the nonlinear effect of shear-thinning turbulence in several aspects including the turbulent statistics, structures related to drag reduction, primary spatial structures of modes from POD, turbulence isotropy, energy cascade, and dissipation contributions at different lengthscales.

Chapter 4 provides a concise discussion of the results and justification of the analysis.

Chapter 5 provides a summary of the conclusions and the primary findings of the current research.

Chapter 6 provides a discussion about the experiment limitation, potential future work and the challenges.

# Chapter 2

## Experimental Setup And Methodology

### 2.1 Overview

The experimental investigations and visualization of turbulent Taylor-Couette flow are conducted in this section. A detailed overview of the T-C flow apparatus, including its components and dimension specifications, is provided. The Stereoscopic Particle Image Velocimetry (SPIV) configuration serves as the imaging approach. The optical settings of the SPIV setup are elaborated upon, covering aspects such as field of view (FOV) selection, camera arrangements, PIV seeding guidelines, and calibration procedures to ensure precise measurement of fluid velocities. Furthermore, the preparation procedure for Polyacrylamide (PAM) solution is outlined. The Carreau-Yasuda viscosity model is employed for modeling shear-thinning viscosity behavior. Additionally, the accuracy and error analysis of the SPIV measurements, along with post-processing steps, are detailed. This comprehensive overview establishes the groundwork for subsequent sections, where the experimental results and findings concerning turbulent Taylor-Couette flow dynamics are discussed.

### 2.2 T-C Flow Apparatus

The Taylor-Couette apparatus employed in the present experiments is shown in Figure 2.1 below. It mainly consists of components as follows: i) T-C chamber, ii) High-speed cameras and lasers iii) DC Motor and iv) Torque Sensor.

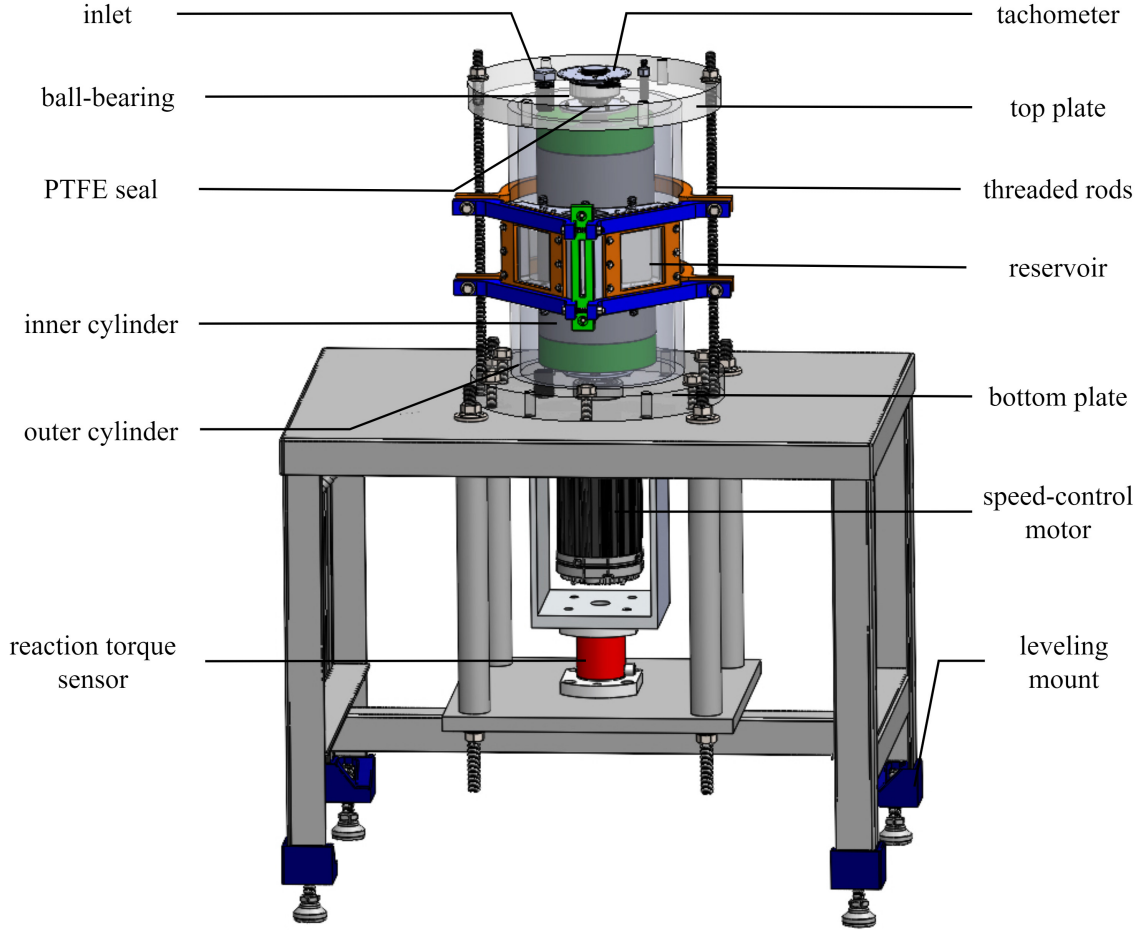


Figure 2.1: Annotated schematic of Taylor-Couette apparatus.

The T-C chamber consisted of two end plates at the top and bottom and two coaxial independent cylinders. Both cylinders were made of cast acrylic, whose clarity allows for clear visualization. The total inner cylinder length is  $l_c = 270.0$  mm and the radius of outer cylinder is  $r_o = 79.4$  mm and it stays stationary. The inner cylinder has a radius  $r_i = 60.3$  mm, corresponding to the gap width between cylinders  $d = 19.1$  mm, radius ratio  $\eta_r = r_i/r_o = 0.76$ , and aspect ratio  $\zeta = l_c/d = 14.1$ . In T-C study, fluid flow is almost inevitably influenced by the presence of the end walls, which is referred to as end effects (Coles and Van Atta 1966; Hollerbach and Fournier 2004). It is argued that end effects come from two major aspects: the limitation of finite span and bottom secondary flow (Wiswell *et al.* 2023). Secondary flow could have important end effects, especially for a small aspect ratio

apparatus  $\eta_r$  of order 10 and less (Burin *et al.* 2006). In the present study, two bowl-shape spacers are designed and put between the inner cylinder and the top and bottom plates to decrease the effect of secondary flow from top and bottom. The region of interest is chosen to be located at the midplane between the top and bottom plates, and the distance from the region of interest to the end plates is 115.0 mm  $\gg d = 19.1$  mm to minimize the end effects.

The inner cylinder was hollow and interference fitted onto a drive rotary shaft. Two shaft collars were fixed onto the shaft at the top and bottom of the inner cylinder to ensure no axial displacement of the inner cylinder. Two high-load (1338 kg radial dynamic load capacity) sealed ball bearings were used and interference fitted in the top and bottom plates. To prevent leakage of fluids, two spring-loaded Graphite PTFE seals were selected for rod sealing and were embedded in the top and bottom plates respectively. The inner and outer cylinders were mounted using tie rods between end plates.

### **Motor**

A ClearPath Integrated Servo Motor (CPM-MCVC-3441S-RLN) with speed control was used. It allows for a maximum rotational speed of 840 RPM and a peak torque of 13.0 N · m, which were large enough to generate turbulence in the T-C system. The motor provides two options of power supply: DC input and AC input. In this study, DC input was adopted, by connecting the motor and Teknic IPC-5 power supply. The AC power cable connected the 120V in-wall power and IPC-5. A USB cable connected the Windows PC to the motor to achieve speed control.

### **Torque Sensor**

Reaction torque sensor (FSH04381-TFF425, FUTEK Advanced Sensor Technology, Inc.) was selected to obtain the reaction torque of the inner rotational cylinder. The TFF sensor was bolted down towards the bottom plate, and the top was grabbed onto the motor chamber that connected to the body of the motor. The torque sensor thus works by measuring the top twisting of the motor with respect to the fixed bottom plate. The maximum torque capacity

is  $7.06 \text{ N} \cdot \text{m}$ . The hysteresis and nonlinearity are all within  $\pm 0.2\%$  of rated output. A USB 220 kit is used to connect the Windows PC to the TFF sensor. A maximum sampling rate up to 4800 Hz could be obtained. In this study, the Nyquist criterion was satisfied when collecting torque signals. The sampling rate was adjusted twice as high as the rotation frequency of the inner cylinder.

## Cameras and Lens

Two CCD cameras (ImagerPro X4M, LaVision GmbH) with have a color image sensor with resolution(  $h \times v$  ) of  $2048 \times 2048$  pixel. The pixel size (  $h \times v$  ) is  $7.4 \times 7.4 \mu\text{m}^2$  . Both ImagerProX 4M cameras were connected to camera controllers from *LaVision*. The cameras require a trigger signal for image recording. A programmable timing unit (PTU 9) was used to generate an accurate camera trigger signal and synchronize the image recording with laser pulses. BNC cables were used to connect the programmable timing unit (PTU 9) from the PC to the socket of camera controllers. Nikon 50 mm focal length, 1 : 2 aperture objective lens were installed on both cameras. Aperture was set to an opening of  $f/16$ , and depth-of-field is set to approximately 4 mm.

## Laser and Optics

An Nd: YAG laser (Solo III-15, New Wave Research) was used as the light source, with 15 Hz repetition rate and 532 nm wavelength. The Solo-PIV laser system provides high energy with a maximum output of 50 mJ. The laser was fired externally and triggered by PTU unit installed in the PC. An adjustable laser sheet optic was utilized which contains a combination of cylindrical and spherical lenses to adjust the focal length of the optics.

## 2.3 Stereo-scopic PIV Configuration

### 2.3.1 Field of View (FOV)

The size of the FOV was designed to include a pair of vortices. The wavelength of TV pair  $\lambda = 2.29$  was used as an estimation in the present study based on experimental results

(Kataoka *et al.* 1977), which showed that for a single vortex, the wavelength of vortex in the axial direction is roughly the same as the gap width  $d$  between cylinders. This was also observed in the present study as will be shown in the subsequent discussion. For Newtonian fluid measurement, the FOV was accomplished with a pair of Nikon Nikkor 50 mm  $F/2$  lenses and 12 mm extension tubes. The spatial resolution achieved was 37.76 pixel/mm. The demonstration of FOV is shown in Figure 2.2 below.

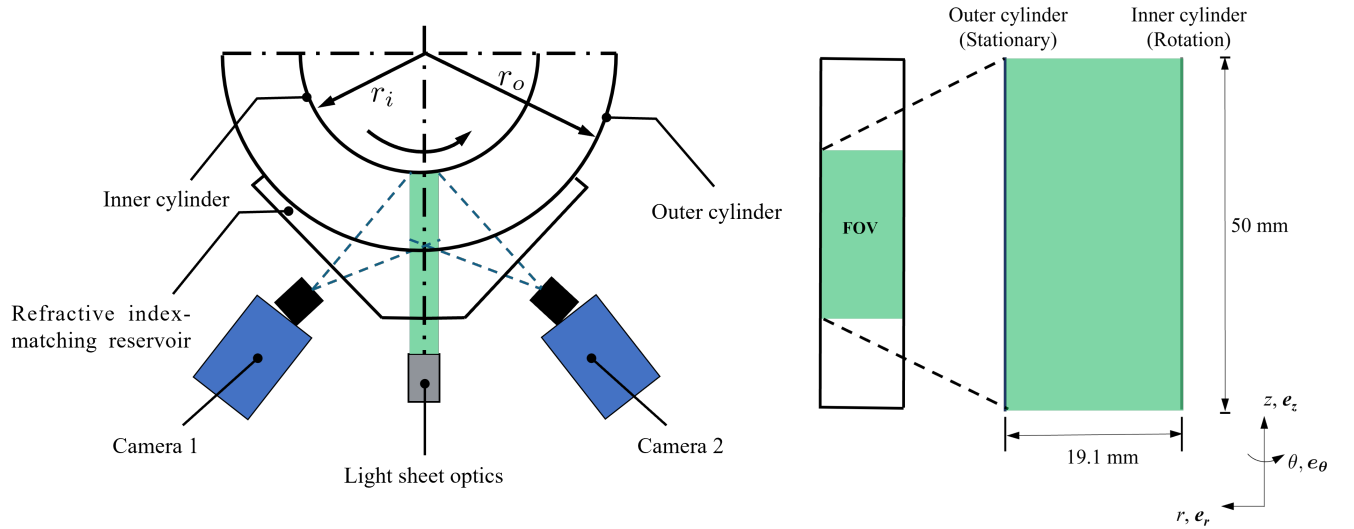


Figure 2.2: Schematic of field of view (FOV).

### 2.3.2 Camera Arrangement

Purely backward-scattering of camera arrangement was employed. In the present study, the laser wavelength  $\lambda = 532$  nm and particle diameter  $d_p = 2 \mu\text{m}$ . Given the value  $d_p \gg \lambda$ , predictions can be made that there will be strong scattering (Mie 1908). However, the intensity of scattering was not uniform in all directions. The backward-scattering arrangement has relatively weak scattered light intensity compared to the forward-scattering camera arrangement based on Mie scattering theory (Fischer 2017; Mie 1908). Considering this factor, laser intensity was adjusted in the experiments to an appropriate level so that the light scattered back from seeding particles is sufficient and can be captured clearly by both cameras.

### 2.3.3 Camera Angle

Reconstruction of the out-of-plane velocity component relies on the perspective disparity from two viewing directions. The angle between the optical axis of two cameras needs to be determined to have minimal uncertainty. The opening angle has to be at least larger than  $20^\circ$  for an accurate reconstruction. It is typical to have an opening angle between cameras from  $30 - 120^\circ$  for a stereo configuration. For a backward forward-scattering configuration, the uncertainty in measuring the out-of-plane component becomes larger as the opening angle between the two cameras increases. It can be proven that when the opening angle is equal to  $90^\circ$ , the uncertainty of all three velocity components is equal and balanced (Prasad 2000; Raffel *et al.* 1998). Mathematically this is true, whereas the overlap of the images captured by two cameras at this angle was found to be slightly sharp, which might lead to a decrease in image quality caused by fewer pixels being detected. It is argued that due to fewer pixels available to calculate the in-plane components that leads to an increase in error estimation, the optimal camera angle in stereo-PIV is actually closer to  $\simeq 30^\circ$  to  $35^\circ$ , indicating the optimal angle between two cameras would be around  $110^\circ - 120^\circ$  (LaVision 2013).

In the present study, camera opening angles were set to  $100^\circ$ , which is slightly less than the recommended optimal opening angle. The Scheimpflug adapters were adjusted to have the lens plane parallel to the window of the reservoir and at the same time, the Scheimpflug criterion was satisfied.

### 2.3.4 Reservoir for Refraction Elimination

One of the challenges in the experimental T-C study is optical aberrations due to the refraction effects at the curved surface of the flow rig. A reservoir for refraction reduction was designed and fitted against the curved surface of the outer cylinder. In this way, the light scattered from seeding particles goes through the interface close to  $90^\circ$ . In the present study, the reservoir was filled with the same liquid as the working fluid in the T-C flow rig. The undesirable refraction effects were thus reduced.

### 2.3.5 Seeding

The PIV measurement technique determines the velocity of fluid flow by following the displacement of seeding particles that are carried by the flow. The instantaneous velocity field is estimated from a pair of images that are separated by laser pulse  $\Delta t$ . As opposed to measuring the fluid velocity directly, the PIV measurement technique is indirect in that what it calculates is the velocity of the seeding particles (Willert *et al.* 2007). Thus, the velocity of particles should be as close to the fluid velocity as possible, so that the motion of particles can represent the fluid motion. To prevent significant differences between the motion of the fluid and particles, it is necessary to investigate their physical properties and how they interact with each other. First, the density of the particle should be neutrally buoyant to be similar to the density of the fluid to avoid body forces creating a difference between the particle and fluid velocities (Willert *et al.* 2007). Furthermore, the volumetric population of seeding particles should not be too dense or sparse. If the volumetric population of seeding particles in a PIV experiment is too sparse, it can lead to several issues, e.g., poor signal-to-noise ratio, incorrect velocity field estimation, and limited spatial resolution for small scale structures (Adrian and Westerweel 2011). High volumetric population could lead to particle agglomeration instead of having well-dispersed particles in the flow. Excessive seeding volumetric population can also cause image saturation, which can result in the loss of image resolution. Typically it is recommended to have a seeding volumetric population close to 0.05 particles per pixel (ppp) (LaVision 2013).

The size of the seeding particles needs to be large enough so that the scattered light can be visible and captured by the cameras. Particle sizes around 2-4 pixels in diameter are recommended (LaVision 2013). In the present experiment, the diameter of 2  $\mu\text{m}$  glass bead seeding particles were added to the flow and the light scattered by the seeding particles was recorded by the cameras. 8-10 particles were achieved per interrogation window to ensure accuracy for most of the interrogation windows. In the same time, the seeding particles should be small enough to follow the fluid motion faithfully.

To verify the tracing accuracy, the Stokes number  $\text{Stk}$  is introduced:

$$\text{Stk} = \frac{\tau_p}{\tau_f}, \quad (2.1)$$

where  $\tau_p$  is the particle's response time, which is defined as:

$$\tau_p = d_p^2 \frac{\rho_p}{18\mu}, \quad (2.2)$$

where  $d_p$  and  $\rho_p$  are the diameter and density of the particle,  $\tau_f$  is characteristic time scale in the flow. In this case  $\tau_f$  was taken as the estimated integral timescale as calculated in Section 3.2.  $\mu$  was taken as the dynamic viscosity for water solution, and nominal viscosity for shear-thinning polymers. It is recommended that Stokes number less than  $10^{-1}$  indicates an acceptable tracing accuracy (Raffel *et al.* 1998).

Additionally, the settling velocity  $\mathbf{U}_g$  is considered to evaluate the source of error induced by the gravitational forces of seeding particles. The settling velocity is given by:

$$\mathbf{U}_g = d_p^2 \frac{(\rho_p - \rho)}{18\mu} \mathbf{g}. \quad (2.3)$$

The Froude number  $\text{Fr}$  of seeding particle that characterizes the settling of particles in the flow is given by:

$$\text{Fr} = \frac{\mathbf{U}_g}{\mathbf{U}_s}, \quad (2.4)$$

where  $\mathbf{U}_s$  is the characteristic velocity scale of the flow, it was taken as the linear velocity at the inner cylinder wall  $U_\theta|_{r=r_i}$  as shown in Table 2.2. Table 2.1 lists the characteristics of the seeding particles for each fluid. It can be seen that both  $\text{Stk}$  and  $\text{Fr}$  are of infinitesimal orders, indicating the seeding particles used in the current experiment follow the flow faithfully. The inertia and settling in the flow are insignificant compared to the characteristic scale of the flow investigated.

Table 2.1: List of dynamic characteristics of the seeding particles under the flow conditions at  $Re = 1.50 \times 10^4$ .

Solution	$\mu$ (Pa · s)	$d_p$ ( $\mu\text{m}$ )	$\rho_p$ ( $\text{kg}/\text{m}^3$ )	$\tau_P$ (s)	$\tau_f$ (s)	$\mathbf{U}_g$ (m/s)	Stk	Fr
Water	$1.0 \times 10^{-3}$	2	2300	$5.1 \times 10^{-7}$	0.48	$2.8 \times 10^{-6}$	$1.1 \times 10^{-6}$	$3.6 \times 10^{-6}$
PAM-200ppm	$2.0 \times 10^{-3}$	2	2300	$2.6 \times 10^{-7}$	0.24	$1.4 \times 10^{-6}$	$1.1 \times 10^{-6}$	$9.0 \times 10^{-6}$
PAM-400ppm	$3.6 \times 10^{-3}$	2	2300	$1.4 \times 10^{-7}$	0.13	$0.8 \times 10^{-6}$	$1.1 \times 10^{-6}$	$2.8 \times 10^{-6}$

### 2.3.6 Particle Image Displacement

The typical particle image displacement rules were proposed in literature (Keane and Adrian 1992; Lu and Sick 2013). A “one-quarter-rule” was suggested for both the in-plane and out-of-plane velocity components. First, the maximum particle displacement in  $x$  (or  $y$ ) direction  $\Delta X$  (or  $\Delta Y$ ) less than 25% of size of the interrogation window  $D_I$  was suggested, i.e.,  $\Delta X \leq \frac{1}{4}D_I$ ,  $\Delta Y \leq \frac{1}{4}D_I$ . For example, for a commonly used final interrogation window size of  $32 \times 32$  pixels, the particle displacement of in-plane components (radial and axial direction) between two consecutive frames should not exceed 8 pixels, i.e.,  $\Delta X \leq 8$  pixel,  $\Delta Y \leq 8$  pixel. It was suggested that normally a 5-pixel shift is preferred (Thielicke and Sonntag 2021). For the out-of-plane motion, a maximum out-of-plane displacement  $\Delta Z$  less than 25% of light sheet thickness  $\Theta$ , i.e.,  $\Delta Z \leq \frac{1}{4}\Theta$ .

In each experiment, the duration between the two consecutive laser pulses  $\Delta t$  was adjusted according to the rules mentioned above to ensure accurate spatial resolution while preventing too many particles with out-of-plane velocity from escaping the light sheet within  $\Delta t$ . For all our experiments,  $\Delta t$  was set such that seeding particles would travel less than a quarter of the light sheet thickness even for the largest expected azimuthal velocity  $U_\theta|_{r=r_i}$  within laser pulse. At the same time, 5-pixel in-plane displacement was guaranteed during the experiment. The  $\Delta t$  used in experiments are listed in Table 2.2.

Table 2.2: List of experimental parameters and optical system properties for SPIV measurement.

Solution	$Re_{\text{nom}}$	$\omega_i$ (rpm)	$\Theta$ (mm)	$U_\theta _{r=r_i}$ (m/s)	$\Delta t$ ( $\mu s$ )	$0.25\Theta/U_\theta _{r=r_i}$ ( $\mu s$ )
Water	$1.50 \times 10^4$	125	2.5	0.79	350	791.49
PAM-200ppm	$1.50 \times 10^4$	250	2.5	1.58	200	395.74
PAM-400ppm	$1.50 \times 10^4$	450	2.5	2.84	100	219.86

### 2.3.7 Calibration

The purpose of calibration is to establish the relationship between the measured pixel displacement and the corresponding physical displacement of seeding particles in the fluid. This relationship is required to convert the pixel displacements observed in the PIV images into actual velocities in the fluid. Camera calibration and self-calibration are the main two steps in this procedure. It is essential to perform a camera calibration before the experiment to obtain the viewing direction of cameras and the relative location of cameras concerning the target, which are information for the reconstruction of the velocity. A second calibration (self-calibration) was employed after the experiment to eliminate the error caused by the misalignment of the calibration target (Raffel *et al.* 1998).

#### Camera Calibration

Camera calibration involves using a customized two-level calibration plate. The calibration plate was milled with a 5-axis CNC mill (POCKET NC V2-50 CHK, PENTA) of high precision (6.10  $\mu\text{m}$  resolution in XYZ (translation) axis and  $0.01^\circ$  resolution in A&B (rotation) axis). The plate was designed to have alternating top and bottom levels. Levels were separated with a defined separation distance. Dot patterns were milled and equally spaced on the two levels of planes with specific spacing between the dots. An image of the target is shown in Figure 2.3 below.

Camera calibration was performed using working fluids to compensate for image distortion caused by light refraction from the working fluid. A new camera calibration was implemented

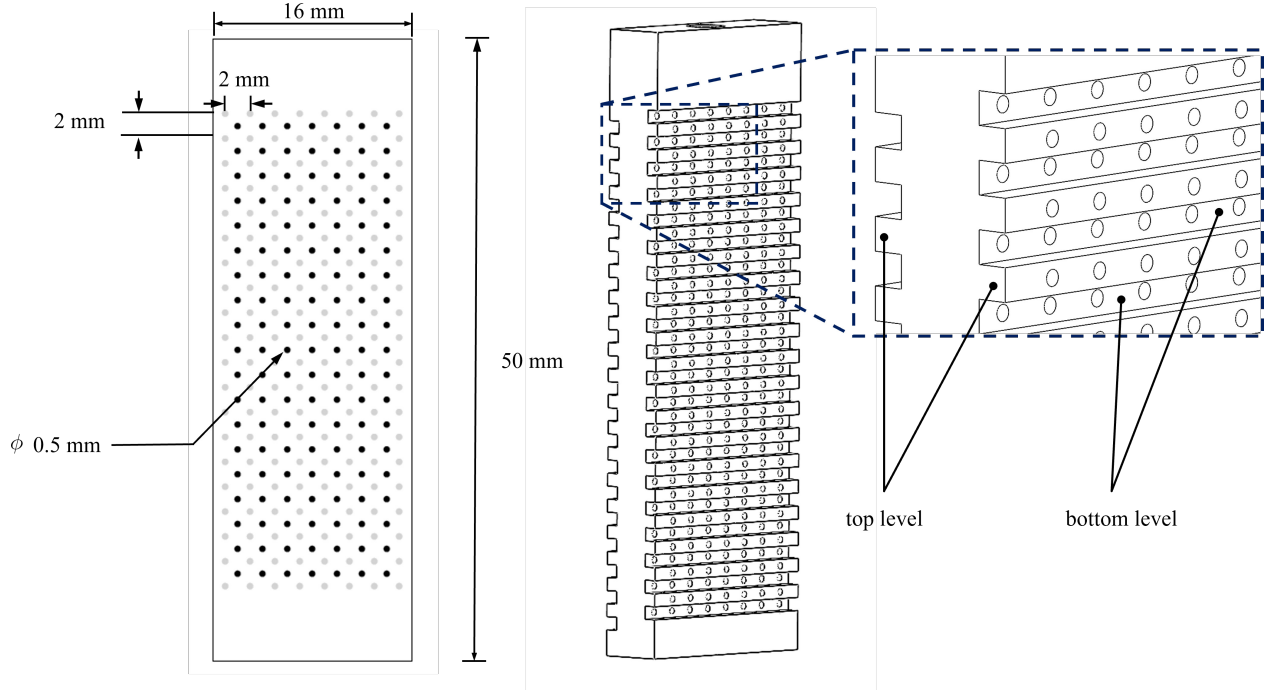


Figure 2.3: Schematic of Calibration Target. The left image shows the dot pattern of the calibration target. The dark dots are on the top level, and the light grey dots are on the bottom level. The right image shows the 3D view of the target.

each time the working fluid was changed to ensure consistency in the obtained results with the current calibration. LaVision LaVision (2013) offers two fit mapping functions: the camera pinhole model and a 3rd-order polynomial. The pinhole model was utilized to verify the camera positions and fit parameters (focal length, distance in  $z$ , rotation  $(x, y, z)$ ), and 3rd-order polynomial model was used for camera calibration.

### Self-Calibration

Self-calibration allows the correction of misalignment of the calibration target to the plane of the light sheet. For each experiment, self-calibration is done with 100 stereo particle images to ensure the quality of self-calibration. The correlation map exhibits peaks that are centered at zero within each window (LaVision 2013). The width of the peaks in the correlation map gives a very good estimate of the laser sheet thickness. In the present experiment, the laser sheet thickness was set to  $\Theta = 2.5$  mm.

## 2.4 Viscosity Model and Polymer Solutions

### 2.4.1 Viscosity Model

In this study, turbulent characteristics of Taylor-Couette flow were experimentally investigated with non-Newtonian polymer solution Polyacrylamide (PAM). PAM is proven to have dramatic shear thinning behavior for a wide range of concentrations up to 5000 ppm (Shabaka *et al.* 2016).

The rheology is described by the Carreau model (Cagney and Balabani 2019):

$$\mu(\dot{\gamma}) = \mu_{\infty} + (\mu_0 - \mu_{\infty}) [1 + (\lambda_c \dot{\gamma})^a]^{(n-1)/2}, \quad (2.5)$$

The non-Newtonian characteristics are described with parameters:  $\mu_0$ ,  $\mu_{\infty}$ ,  $\lambda_c$  and  $n$ .  $\mu_0$  and  $\mu_{\infty}$  are the values of dynamic viscosities at zero and infinite shear rates.  $\lambda_c$  is the relaxation time of the fluid and  $n$  is the flow index (shear thinning fluid,  $n < 1$ ).  $\dot{\gamma}$  is the magnitude of the rate-of-strain tensor, i.e, shear rate. The shear rate is defined as:

$$\dot{\gamma} = \sqrt{2\mathbf{D} : \mathbf{D}}, \quad (2.6)$$

where  $\mathbf{D}$  is the strain-rate tensor in convention.  $\mathbf{D} = 1/2 [\nabla\mathbf{U} + (\nabla\mathbf{U})^T]$ .

The second invariant of the strain-rate tensor is expressed:

$$\Gamma = \frac{1}{2} \dot{\gamma} : \dot{\gamma} = \frac{1}{2} \dot{\gamma}_{ij} \dot{\gamma}_{ji}, \quad (2.7)$$

where  $\dot{\gamma}$  is the rate of strain tensor.  $\dot{\gamma} = \nabla\mathbf{U} + (\nabla\mathbf{U})^T$ . The relation between  $\mathbf{D}$  and  $\dot{\gamma}$ :

$$\dot{\gamma} = 2\mathbf{D}. \quad (2.8)$$

In Equation 2.7, the Einstein's summation convention for repeated indices is used. Since the rate of strain tensor  $\dot{\gamma}$  is symmetric, thus:

$$\Gamma = \frac{1}{2} \dot{\gamma} : \dot{\gamma} = \frac{1}{2} \dot{\gamma}_{ij} \dot{\gamma}_{ji} = \frac{1}{2} \dot{\gamma}_{ij} \dot{\gamma}_{ij}. \quad (2.9)$$

The relation between the second invariant of the strain-rate tensor  $\Gamma$  and shear rate  $\dot{\gamma}$  is:

$$\dot{\gamma} = \sqrt{\frac{1}{2} \sum_i \sum_j \dot{\gamma}_{ij} \dot{\gamma}_{ji}} = \sqrt{\Gamma}. \quad (2.10)$$

## 2.4.2 Experimental Fluids

### Newtonian Fluid Selection

Water was selected as a pure solvent compared to the PAM solutions. The dynamic viscosity of water is  $10^{-3} \text{ Pa} \cdot \text{s}$  under  $21^\circ\text{C}$ . The water-glycerol mixture has been proven to maintain constant viscosity regardless of the applied shear rate (Hanson *et al.* 2019). Additionally, 80% by volume of glycerol with a high viscosity of  $0.086 \text{ Pa} \cdot \text{s}$  was used in stereoscopic configuration accuracy verification (Volk and Kähler 2018).

### Non-Newtonian Fluid Selection

In this study, the same Polyacrylamide (PAM) powders and concentrations of PAM solution were used similar to the literature (Azadi 2023) to ensure consistency. The parameters of each solution are listed in Table 2.3.  $C_p$  represents concentration of PAM solution, and  $\rho$  is the density of the solution.

Table 2.3: Carreau-Yasuda model parameters for tested solutions. Property of PAM data comes from (Azadi 2023). Properties of glycerol-water mixtures come from (Volk and Kähler 2018).

Solution	$C_p$ (ppm)	$\rho$ ( $\text{kg}/\text{m}^3$ )	$\mu_0$ ( $\text{Pa} \cdot \text{s}$ )	$\mu_\infty$ ( $\text{Pa} \cdot \text{s}$ )	$\lambda_c$ (s)	$n$	$a$
1	0	997.0	$10^{-3}$	$10^{-3}$	-	1	-
2	200	997.2	$8.010 \times 10^{-3}$	$1.388 \times 10^{-3}$	2.287	0.58	3.523
3	400	997.4	$8.395 \times 10^{-3}$	$1.525 \times 10^{-3}$	0.164	0.53	0.732

The assumed viscosity versus shear rate  $\dot{\gamma}$  by the Carreau-Yasuda model was shown in Figure 2.4.

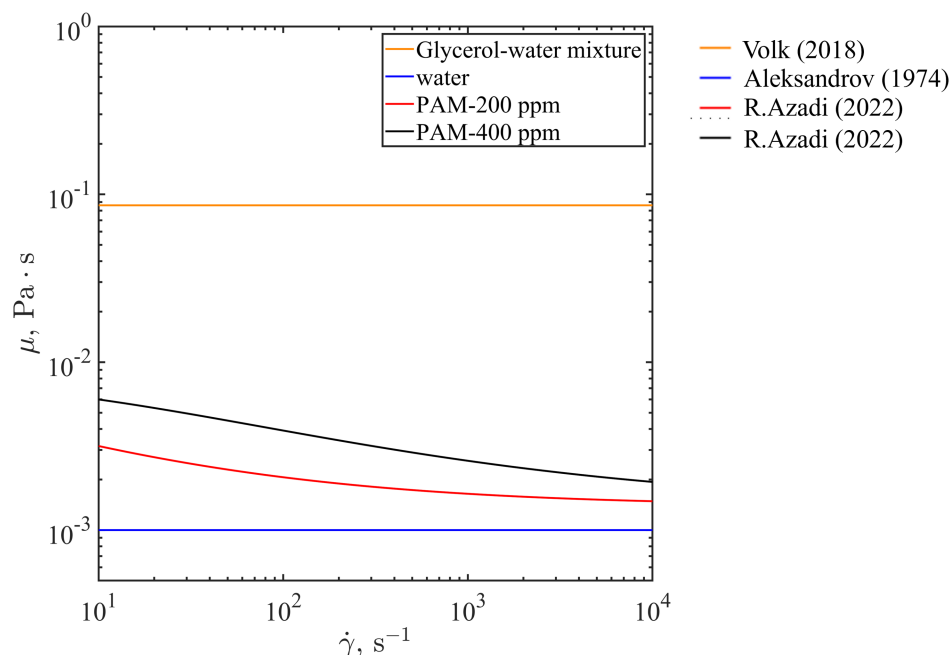


Figure 2.4: Plot of Dynamic viscosity versus shear rate. Figure replotted with permission (Azadi and Nobes 2022).

### 2.4.3 Preparation Procedure

The preparation procedure follows the literature (Azadi and Nobes 2022). To prepare the PAM solutions of different concentrations, a high-concentration master solution with a small volume was prepared, which will be added to different amounts of water later. First, the precise weighing of the required amount of PAM polymer was carried out with a precision of  $\pm 0.1 \text{ mg}$  (Mettler Toledo, AB104-S). The PAM powder and water were gradually added to a beaker and mixed with a magnetic stirrer mixer to ensure polymers were fully dispersed and no aggregation of polymer molecules. After 2 hours of continuous mixing, the master solution was added to an appropriate amount of water to achieve the desired concentration (200, 400 ppm). A vacuum pump was utilized to eliminate air bubbles present in the solution which could affect the quality of particle images.

#### 2.4.4 Post-Processing

The implementation of post-processing of particle images involved the calculation of double frame vectors. A lengthscale of 8 pixels was chosen for sliding background subtraction. The intensity of particle images was filtered with a min-max filter, with a 4-pixel lengthscale. The particle images were cropped by applying square geometric masks for each camera to define the region of interest. Stereo cross-correlation was enabled and a multi-pass (decreasing size) algorithm was used, with an initial interrogation window size of  $48 \times 48$  pixel and a final interrogation window size of  $24 \times 24$  pixel with 75% overlap to gain higher spatial resolution. No weighting function was selected and the square-shaped interrogation window (aspect ratio of 1:1) was chosen. The final interrogation window size of  $24 \times 24$  pixel is able to offer the true interrogation window size of  $0.64 \times 0.64 \text{ mm}^2$ . A median filter was used for multi-pass post-processing. It is worth mentioning that  $4(2 \times 2)$  interrogation windows are needed to resolve a vortex (LaVision 2013), thus the size of a perfect circular vortex that the current resolution is able to resolve is  $1.28 \times 1.28 \text{ mm}^2$ .

### 2.5 SPIV Accuracy and Uncertainty Analysis

The SPIV measurements of the Taylor-Couette flow rig has sources of errors, both random and systematic, which must be estimated and quantified using uncertainty bounds. These sources include calibration precision (quality of calibration target, camera positions, etc.), image distortion arising from refractive index matching quality, light-sheet thickness, and spatial resolution. Therefore, it was important to scrutinize the reliability of the stereoscopic velocity measurements. To assess the accuracy of out-of-plane motion, a preliminary test was conducted under conditions of pure laminar flow, aligning with the methodology proposed by Ravelet *et al.* (2010). This approach considered the compounding factors mentioned above without differentiating them, and a total compounding error could be obtained for the out-of-plane motion. However, the accuracy of in-plane velocity components is unable to be verified, since they are extremely close to zero as expected. Following the prescribed

procedure, measurements were conducted in a laminar flow scenario with the inner cylinder rotating at a Reynolds number as low as  $\text{Re} \approx 10$ , utilizing an 80% by volume glycerol-water mixture as mentioned previously. In this particular instance, the analytical velocity field is well-defined, with zero radial and axial velocities (secondary flow), and the azimuthal velocity was anticipated to be entirely axisymmetric with no axial dependence, as shown in Equation 1.5. Scaling of coordinates was performed. The radial coordinate was scaled to a range from 0 (outer cylinder wall) to 1 (inner cylinder wall). The dimensionless radial coordinate is given by:

$$r^* = (r_o - r) / d, \quad (2.11)$$

where  $d$  is the gap width.

The axial coordinate was scaled and the dimensionless axial coordinate is given by:

$$z^* = z / d, \quad (2.12)$$

where  $z$  is the physical distance of axial length. The result of the measured azimuthal velocity is shown in Figure 2.5. It can be seen that the result at the bulk is in good agreement with the analytical solution, with less than 10% of relative error in the region  $r^* \in (0.2, 1)$ . However at the outer cylinder wall where  $r^* = 0$ , a strong deviation was observed. In the present study, the configuration employed was similar to that utilized by Ravelet *et al.* (2010), where a strong deviation of measured azimuthal velocity from the theoretical solution near the cylinder was observed as well. The measurements conducted by Ravelet *et al.* (2010) showed reliability only within the range of  $0.1 \leq (r - r_i) / d \leq 0.85$ . The reason given was due to the refraction close to the curved wall that causes measurement errors. However, in the present experiment, a refractive index matching reservoir was employed to mitigate refraction, yet the deviation was still observed. This suggests that refraction might not be the primary factor contributing to this error. This thesis suggests another potential factor that is attributed to the inherent mechanism that SPIV relies on a finite-thickness light sheet to reconstruct the out-of-plane velocity, combined with the cylindrical flow rig used. The error that arises from the light sheet is typically considered negligible in most cases (if all in-

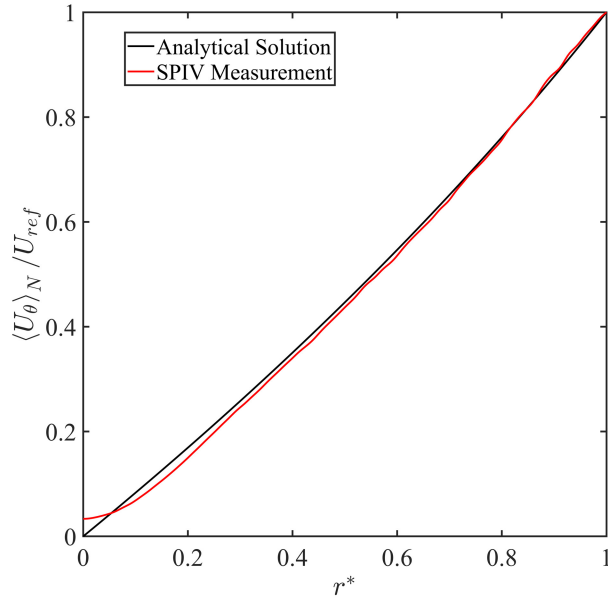


Figure 2.5: Plot of Normalized azimuthal velocity profile for  $\text{Re} \approx 10$ .

plane motions can be considered identical), but in Taylor-Couette turbulence the light sheet thickness could affect the accuracy of the near-wall velocity measurement. Since the Taylor-Couette geometry is cylindrical, the in-plane fluid motions illuminated by the light sheet can have a discrepancy, and this discrepancy can be non-negligible at the near-wall region. The cameras can notice this discrepancy from two different orientations. Each camera can determine an in-plane velocity field, and the out-of-plane velocity is reconstructed based on the two different in-plane velocity fields (ideally should be the same), which leads to a high reconstruction uncertainty, especially at the walls. The present study mainly focuses on regions in the bulk, where the velocity measurements of laminar flow show good agreement with the theoretical azimuthal velocity profile to guarantee measurement accuracy.

# Chapter 3

## Results

### 3.1 Overview

This chapter discusses the nonlinear effect of shear-thinning polymers on the TTC regime. Experimental results of three velocity components were obtained from SPIV measurement of Taylor-Couette turbulence at  $Re = 1.50 \times 10^4$  for water, PAM-200 ppm, and PAM-400 ppm solutions. Turbulent statistics from SPIV measurements were used to demonstrate and verify the statistical convergence of the flow. Instantaneous and ensemble-averaged velocity and vorticity of water and PAM-200 ppm solutions in the  $r - z$  directions were calculated to investigate Newtonian and non-Newtonian secondary vortical structures. Turbulent statistics including Reynolds normal and shear stresses were investigated and discussed. Locations and sizes of secondary Taylor vortices were obtained by using the  $\Gamma_1$  and  $\Gamma_2$  vortex identification algorithm, respectively. The statistics and distributions of vortex cores in space were discussed. To get a better understanding of the vortical structures of the turbulent Taylor vortices (TTV) regime and the spatial organizations, snapshot Proper Orthogonal Decomposition (POD) was implemented. The energetic modes and the energy distribution associated with the modes are discussed. Two spatial correlations in the  $r$  and  $z$  directions were investigated by calculating the two-point correlation of velocity fluctuations. Two dimensional energy and dissipation spectra for three solutions were calculated and discussed to understand the energy and dissipation distribution under different shear-thinning effects.

## 3.2 Statistical Convergence

Statistical convergence refers to the point at which the statistical properties of the measured velocity field become consistent and stable. In practice, statistical convergence is typically assessed by analyzing the convergence of statistical moments of the velocity field (Ullum *et al.* 1998; Westerweel 1997). This section is divided mainly into two subsections that discuss the estimation of the time span and the number of samples necessary to achieve statistical convergence.

### 3.2.1 Estimation of Time Span

Turbulent statistics (first and second-order statistics) were computed based on the averaging of the instantaneous velocity. This study introduces two different turbulent fluctuations based on two different averaging, as defined by Smith and Townsend (1982). The fluctuation  $u$  that is defined merely based on the ensemble average was adopted as shown in Equation 1.24. This fluctuation  $u$  represents the fluctuation resulting from turbulence.

Besides, another definition of fluctuation  $u'$  is introduced based on both ensemble and axial averaging:

$$u' = U - \langle U \rangle_{z,N}, \quad (3.1)$$

where  $u'$  represents the velocity fluctuation in time (due to turbulence) combined with the local deviation away from the axially averaged mean TV motion. This definition is slightly different compared to literature (Bilson and Bremhorst 2007) wherein the velocity components are spatially averaged over the azimuthal direction as well. Pirro and Quadrio (2008) studied turbulent Taylor-Couette regime at  $Re = 10500$  by DNS technique assuming two spatially homogeneous directions (axial and azimuthal direction) for simplification and computational efficiency and the results have been validated by previous simulation and experiments. Given the assumption of Taylor-Couette turbulence can be considered spatially homogeneous in the azimuthal direction, the discrepancy between these two averaging can

almost be neglected (Errante *et al.* 2024).

Turbulent flows are characterized by velocity fluctuations over a range of length and time scales (Pope 2001). To characterize these fluctuations faithfully as an ergodic process, the PIV system must acquire velocity data over a sufficiently long time span. Insufficient measurement duration leads to ensemble averages which are not representative of the entire population of data.

Determination of the optimal time span for investigating turbulent Taylor-Couette flow relies on certain premises to simplify the analysis. First, Taylor-Couette turbulence is assumed to be statistically stationary, indicating that all multi-time statistics remain invariant under a shift in time (Pope 2001). This assumption facilitates the characterization of Taylor-Couette turbulence as a stochastic process, which is available to be explored through an examination of multi-time statistics. To guarantee the statistical stationarity, the Taylor-Couette flow rig was operated with the flow before data collection to ensure the turbulence was fully developed, allowing the system to reach a statistically stationary state. Second, it is presumed that Taylor-Couette turbulence can attain an ergodic state. Under the assumption of statistically stationary flows, ergodicity denotes the equivalence between the statistical properties of a true ensemble average and the time average over an extended duration (Aubinet *et al.* 2012). To achieve ergodicity, the selected time span  $T$  needs to be an order of magnitude larger than the integral timescale, which can be estimated prior to the experiment. In this study, the estimated integral timescale is taken by the time for the inner cylinder to complete one revolution (Bilson and Bremhorst 2007):

$$\bar{\tau}_{est} = \frac{2\pi}{\omega_i}. \quad (3.2)$$

The time span  $T$  for each experiment lasted over 10 minutes which is significantly greater than the integral timescale, indicating the condition of the ergodicity hypothesis was satisfied. Ensemble averaging was performed over the entire span of the process which was separated by a timescale  $\tau_e$  slightly greater than the estimated integral timescale  $\bar{\tau}_{est}$ , e.g., for water at  $\text{Re} = 1.50 \times 10^4$ ,  $\tau_e = 3/f \geq \bar{\tau}_{est}$ , where  $f$  is the image acquisition rate of cameras to

acquire velocity fields.  $f = 5$  Hz for all cases.

### 3.2.2 Estimation of Number of Samples

To obtain accurate ensemble-averaged results using PIV, it is important to determine the necessary number of PIV recordings needed. This determination involves finding a balance between the relatively short time required to take PIV recordings and the time required to maintain constant external experimental conditions (Raffel *et al.* 1998). If too few PIV recordings are taken, the resulting data may not be representative of the overall flow behavior. On the other hand, taking too many PIV recordings may be time-consuming and may result in changes to the external experimental conditions, e.g., changes in temperature or fluid properties (especially for shear-thinning fluids), which can impact the accuracy of the data. In this study, the square of variability was utilized to measure the rate of convergence to obtain the number of samples necessary to achieve a desired accuracy level of statistical convergence (George 2013). The variability of the estimator for mean, variance, and cross-variance of velocity were investigated.

**Variability of estimator for mean** The number of samples  $N$  needed based on the mean is given by (George 2013):

$$N = \frac{1}{\epsilon_{U_N}^2} \left( \frac{\sigma_U}{\langle U \rangle} \right)^2, \quad (3.3)$$

where  $U$  is instantaneous velocity signal,  $\langle U \rangle$  denotes the true mean velocity, and  $\sigma_U$  denotes the standard deviation of a velocity signal.  $\sigma_U / \langle U \rangle$  indicates the ensemble relative fluctuation level. Huisman *et al.* (2013b) investigated the strong T-C turbulence with  $Re$  varies from  $2.5 \times 10^4$  to  $1.5 \times 10^6$ , the results showed that the maximum fluctuation level of azimuthal velocity is around 10%. The ensemble relative fluctuation level of this study was based on this value to get an estimation of the samples needed. Thus the minimum number of independent samples has to satisfy  $N \geq 100$  to obtain statistical convergence of mean value within an accuracy tolerance of 1% ( $\epsilon_{U_N} = 0.01$ ).

**Variability of estimator for variance** The number of samples  $N$  needed based on variance is given by:

$$\epsilon_{\text{var}_N}^2 = \frac{1}{N} \left( \frac{\langle (U - \langle U \rangle)^4 \rangle}{[\text{var}\{U\}]^2} - 1 \right), \quad (3.4)$$

where  $\langle (U - \langle U \rangle)^4 \rangle$  is the 4<sup>th</sup> order central moment, and  $\langle (U - \langle U \rangle)^4 \rangle / [\text{var}\{U\}]^2$  is the kurtosis of random variable  $U$ . It is necessary to know the statistical distribution of the random variable  $U$  in T-C turbulence to determine the value of the kurtosis. Huisman *et al.* (2013a) investigated Newtonian turbulent statistics of T-C flow with  $\text{Re} = 1.38 \times 10^6$  and found that the probability density function of azimuthal velocity behaves like Gaussian and its kurtosis value is close to 3. Here, the assumption was made that the velocity signal  $U$  is a random variable that follows a Gaussian distribution, whose kurtosis value is strictly equal to 3. With this assumption, the number of realizations  $N$  needed is given by:

$$N = \frac{2}{\epsilon_{\text{var}_N}^2}. \quad (3.5)$$

If the variability accuracy  $\epsilon_{\text{var}_N}$  was specified to be 5%, the number of samples  $N$  has to satisfy  $N \geq 800$  images. In the present study,  $N = 3000$  was chosen for cases whose  $\omega_i \leq 250$  rpm and  $N = 5000$  for  $\omega_i = 450$  rpm, It can be seen that more than sufficient samples are collected to satisfy the variability of accuracy and further ensure the reliability of the statistical convergence.

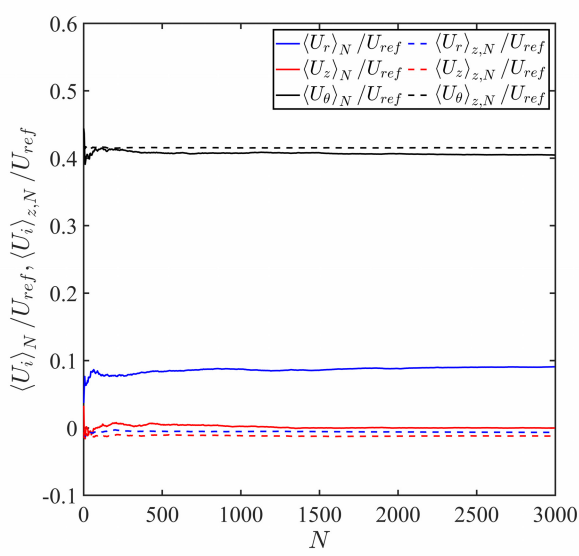
Table 3.1 summarizes the estimated integral timescale  $\bar{\tau}_{est}$ , timescale  $\tau_e$  used for ensemble average, image acquisition rate  $f$ , overall time span  $T$  and number of pairs of images  $N$ .

First and second-order statistics were inspected to demonstrate the statistical convergence at  $\text{Re} = 1.50 \times 10^4$ , which are based on the ensemble average and space-ensemble average mentioned previously. For ensemble average, a single-point ensemble mean  $\langle U_i \rangle_N / U_{ref}$  and variance  $\langle u_i'^2 \rangle_N / U_{ref}^2$  were computed at the midpoint  $P((r_o + r_i)/2, z/2)$  within the field of view. For space-ensemble average, axial and ensemble-averaged statistics  $\langle U_i \rangle_{z,N} / U_{ref}$  and  $\langle u_i'^2 \rangle_{z,N} / U_{ref}^2$  at midline  $r = (r_o + r_i)/2$  were inspected. Figure 3.1 to Figure 3.3 show the

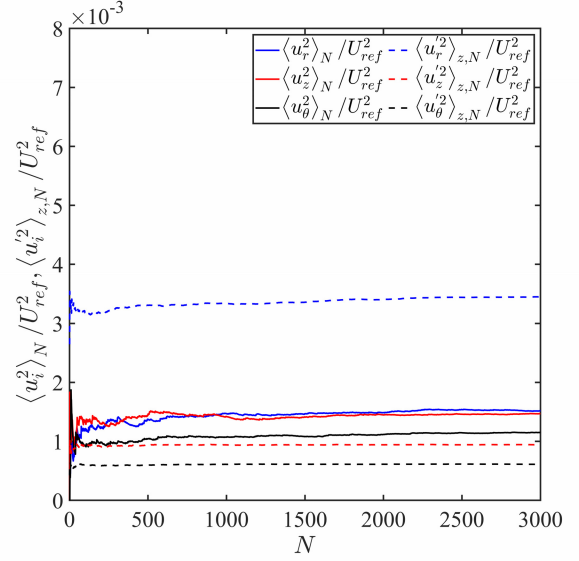
Table 3.1: List of experimental parameters of number of samples and number of images in each experiment.

Solution	Re	$\omega_i$ (rpm)	$\bar{\tau}_{est}$ (s)	$\tau_e$ (s)	$f$ (Hz)	$T$ (min)	$N$
Water	15000	125	0.48	0.6	5	10	3000
PAM-200ppm	15000	250	0.24	0.4	5	10	3000
PAM-400ppm	15000	450	0.13	0.2	5	16.7	5000

variability of statistics for three different fluids under  $Re = 1.50 \times 10^4$ . It can be seen that all statistics converge after 3000 samples, indicating an appropriate time span  $T$  selection. Figure 3.2a and Figure 3.3a show that with the addition of polymers, the ensemble mean of radial velocity  $\langle U_r \rangle_N / U_{ref}$  is significantly reduced. Figure 3.3a demonstrates a notable increase in the second-order statistics of  $\langle u_i'^2 \rangle_{z,N} / U_{ref}^2$  for PAM-400 ppm compared to pure water in Figure 3.1b and PAM-200 ppm in Figure 3.2b. This increase can be attributed to the stronger axial motion of Taylor vortices as the concentration of polymer increases.

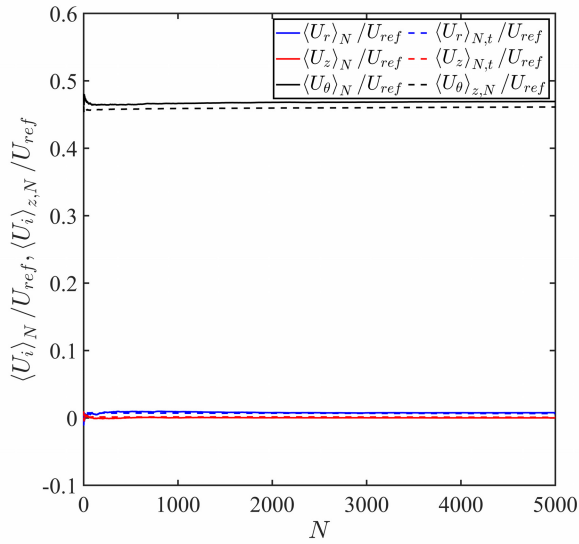


(a)

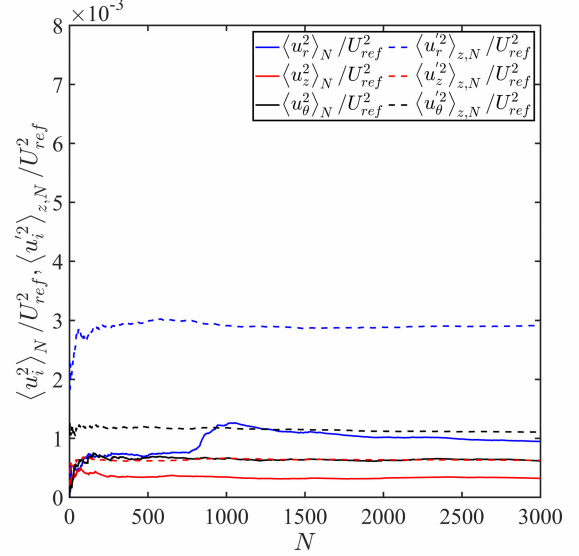


(b)

Figure 3.1: Variability of statistics for water at  $Re = 1.50 \times 10^4$ . (a) Mean statistics based on ensemble average and axial-ensemble average. (b) Variance statistics based on ensemble average and axial-ensemble average.



(a)



(b)

Figure 3.2: Variability of statistics for PAM-200ppm at  $Re = 1.50 \times 10^4$ . (a) Mean statistics based on ensemble average and axial-ensemble average. (b) Variance statistics based on ensemble average and axial-ensemble average.

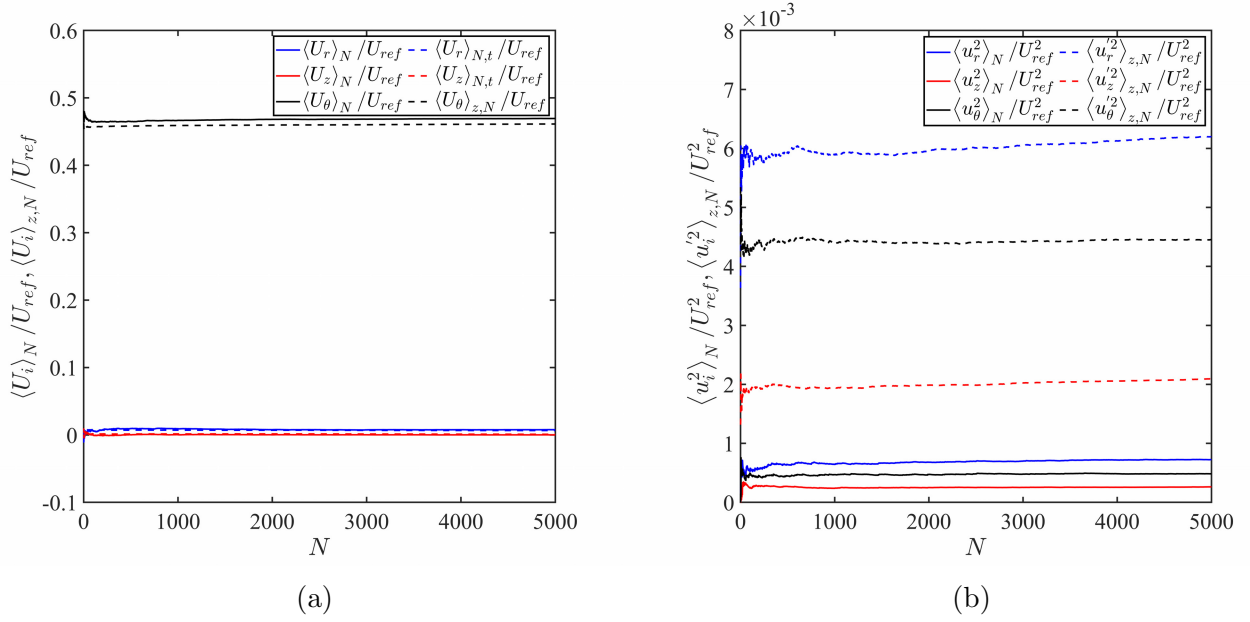


Figure 3.3: Variability of statistics for PAM-400ppm at  $Re = 1.50 \times 10^4$ . (a) Mean statistics based on ensemble average and axial-ensemble average. (b) Variance statistics based on ensemble average and axial-ensemble average.

### 3.3 Skin Friction and Prandtl-von Kármán Law

A turbulent regime for polymeric flows is usually associated with drag reduction (Mohamadtabar *et al.* 2017; Warholic *et al.* 1999). In Taylor-Couette turbulence, the skin-friction coefficient is defined as (Srinivasan *et al.* 2015):

$$C_{f,s} = \frac{\tau_{w,i}}{\frac{1}{2}\rho U_{ref}^2}, \quad (3.6)$$

where  $\tau_{w,i}$  is the average inner wall shear stress.

The average inner wall shear stress in T-C flow is given by: (Huisman *et al.* 2013b):

$$\tau_{w,i} = \frac{\langle T_z \rangle_t}{2\pi r_i^2 l_c}, \quad (3.7)$$

where  $T_z$  is the measured torque.

Another definition of skin coefficient  $C_{f,l}$  was given by Lathrop *et al.* (1992), and the relation between  $C_{f,s}$  and  $C_{f,l}$  is shown as (detail derivation see Appendix B.1):

$$\frac{C_{f,l}}{C_{f,s}} = \frac{\pi r_i^2}{d^2}. \quad (3.8)$$

Based on the definition of  $C_{f,l}$ , the relation between  $C_{f,l}$  and Re is given by:

$$\frac{1}{\sqrt{C_{f,l}}} = N \log_{10} \left( \text{Re} \sqrt{C_{f,l}} \right) + M, \quad (3.9)$$

where  $M$  and  $N$  are the two fitting coefficients:

$$N = \frac{(1 - \eta_r^2) \ln 10}{\eta_r \kappa \sqrt{2\pi}}, \quad M = N \left\{ \left[ \ln \left( \frac{1 - \eta_r}{1 + \eta_r} \right) \frac{1}{y_0^+ \sqrt{2\pi}} \right] + \kappa y_0^+ \right\}, \quad (3.10)$$

where  $\kappa$  is the von- Kármán constant, and  $y_0^+$  is the dimensionless distance of the viscous sublayer from the wall. The equation 3.9 is referred to as the Prandtl-von Kármán equation which works for Taylor-Couette turbulence.

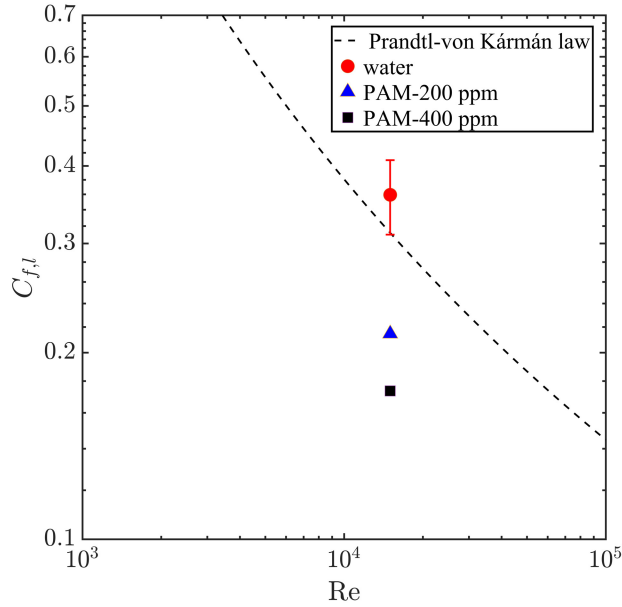


Figure 3.4: Plot of skin friction coefficient vs Re.

Figure 3.4 shows the skin friction factor  $C_{f,l}$  versus Re. It can be seen that the friction factor for water is in agreement with the fitted Prandtl-Kármán equation where the fitting coefficients  $M = 3.218$  and  $N = -1.276$ . The von Kármán constant  $\kappa = 0.4$  and  $y_0^+ = 5$ . The obtained  $C_{f,l}$  for water, PAM-200 ppm, and PAM-400 ppm is 0.36, 0.21 and 0.17,

respectively. The error bar of water shows a 14% difference with the theoretical Newtonian Prandtl-von Kármán law.

The percentage of drag reduction  $DR\%$  is defined as:

$$DR = \frac{C_{f,l\_water} - C_{f,l\_PAM}}{C_{f,l\_water}} \times 100\%. \quad (3.11)$$

The drag reduction for PAM-200 ppm is  $DR \sim 41\%$ , and for PAM-400 ppm is  $DR \sim 52\%$ . Overall it can be seen that the addition of polymers increases the percentage of drag reduction, which can be attributed to the reduction of Reynolds shear stresses at the wall (Warholic *et al.* 1999).

### 3.4 Observations of Instantaneous and Mean Taylor Vortices

Instantaneous in-plane velocity fields using streamlines  $\mathbf{U}(U_r, U_z)$  and the ensemble-averaged velocity field  $\langle \mathbf{U}(U_r, U_z) \rangle_N$  of water at  $Re = 1.50 \times 10^4$  are shown in Figure 3.5 below.

Figure 3.5a and 3.5b shows two instantaneous snapshots of the turbulent Taylor-Couette regime. A pair of counter-rotating Taylor vortices are observed, which are the primary vortex structures in the flow. A smaller vortex is identified close to the outer cylinder in Figure 3.5a, positioned between the two primary Taylor vortices. Earlier observations made by Barcilon and Brindley (1984), who noted the existence of smaller-scale coherent motions in high Reynolds number Taylor-Couette turbulence, called Görtler vortices. Bilson and Bremhorst (2007) used direct numerical simulation (DNS) and detected a pair of secondary vortex motions of a smaller scale alongside the primary Taylor Vortex (TV) motions at  $Re = 3200$ . The emergence of smaller-scale vortices is attributed to the shear occurring between the primary vortex motions.

Figure 3.5c shows that the mean vortex centre is situated at around  $r^* = 0.5$ . It can be seen that the primary Taylor vortex motions remain whereas the small-scale vortex motion is averaged out. Compared with the mean Taylor vortices, it can be found that instantaneous

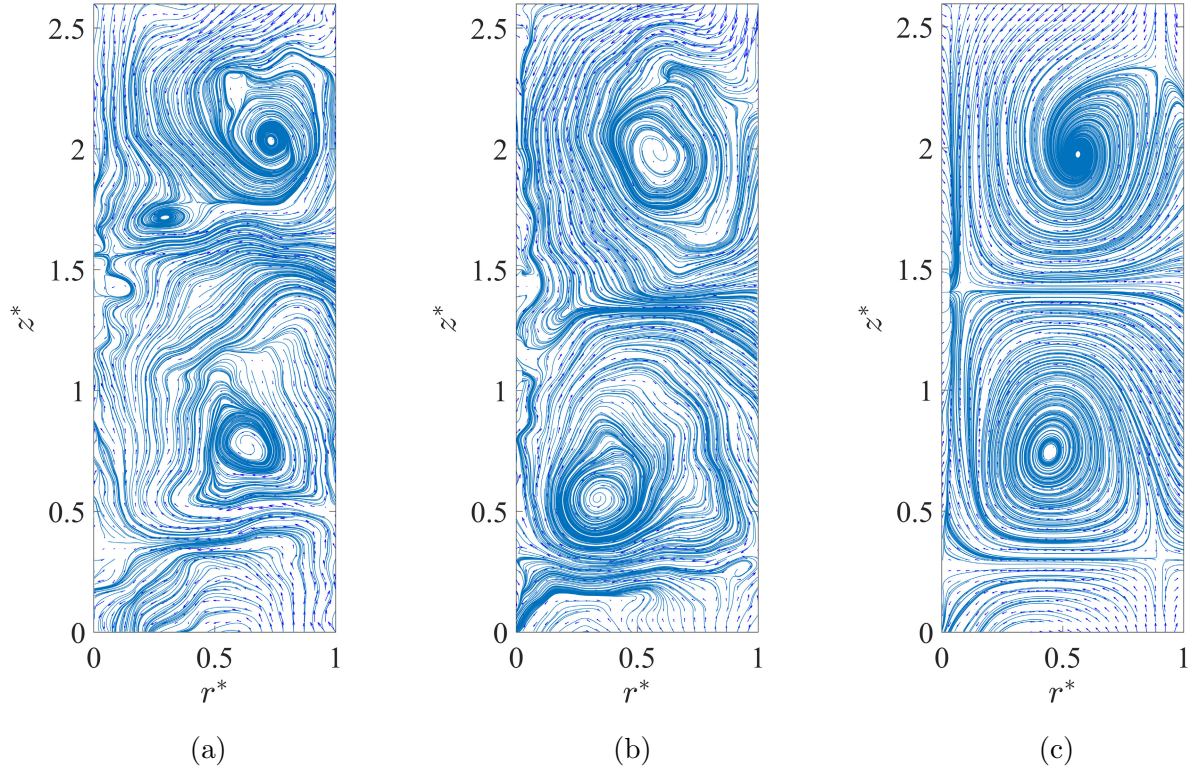


Figure 3.5: Plot of streamlines of turbulent Taylor-Couette vortical structures for water at  $\text{Re} = 1.50 \times 10^4$ . (a-b) Streamlines of instantaneous velocity  $\mathbf{U}(U_r, U_z)$ . (c) Streamlines of ensemble-averaged velocity  $\langle \mathbf{U}(U_r, U_z) \rangle_N$ .

Taylor vortices have both radial and axial motions.

Instantaneous and ensemble-averaged velocity fields of PAM-200ppm at  $\text{Re} = 1.50 \times 10^4$  are presented in Figure 3.6. It can be seen that the instantaneous positions of vortices do not match the mean vortex location, and a pronounced axial displacement of vortex centres is found. Thus it is reasonable to postulate that secondary vortices display considerable deformation and meandering. Figure 3.6c shows that the mean vortex cores are positioned closer to the inner cylinder wall. This aligns with earlier findings reported in the literature for T-C flow with shear-thinning polymers at a lower Reynolds number (Cagney and Balabani 2019; Topayev *et al.* 2019).

Figure 3.7a to 3.7c show three instantaneous in-plane velocity fields  $\mathbf{U}(U_r, U_z)$  of PAM-400 ppm at  $\text{Re} = 1.50 \times 10^4$ . Vortical structures of different length scales are shown to undergo

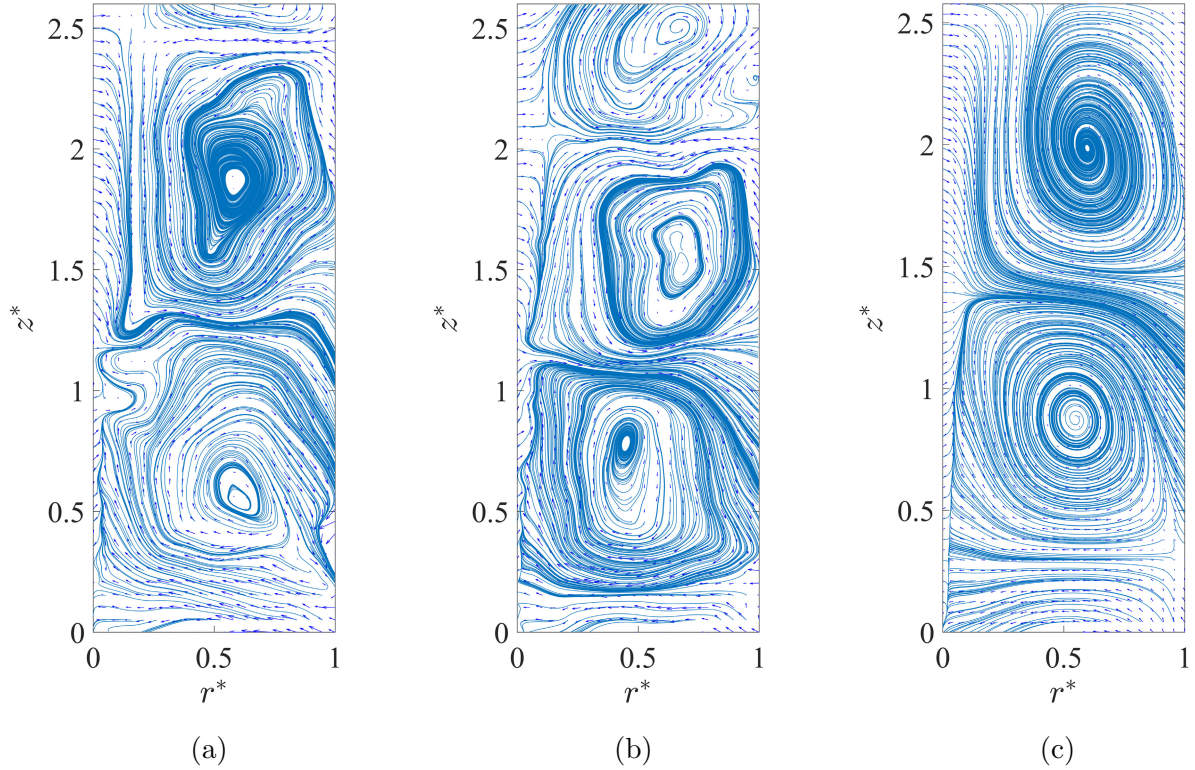


Figure 3.6: Plot of streamlines of Taylor-Couette vortical structures for PAM-200 ppm at  $\text{Re} = 1.50 \times 10^4$ . (a-b) Streamlines of instantaneous velocity. (c) Streamlines of ensemble-averaged velocity  $\langle \mathbf{U}(U_r, U_z) \rangle_N$ .

deformation with different patterns in time. These secondary vortices exhibit dynamic behavior of continuously stretching and shrinking in size, which can be related to the elastic characteristics of PAM solution and the non-linear effects induced by the varying viscosity of the shear-thinning fluid. It is also noticed that the number of vortices increases for PAM-400 ppm compared to the other two cases. The reason is that due to the shear-thinning effect, the jet between two neighboring vortices induces a sharper shear rate. It is already known that shear is essential for vortex formation. This leads to the vortices tend to get closer to the radial jet, which eventually leads to more compacted distribution of vortices within the FOV. Since the shear is more concentrated for high shear-thinning concentration, the large-scale vortex deformation is easier. It can be concluded that at this concentration the non-linearity of the viscosity effect alters the flow regimes and reshapes the evolving vortical

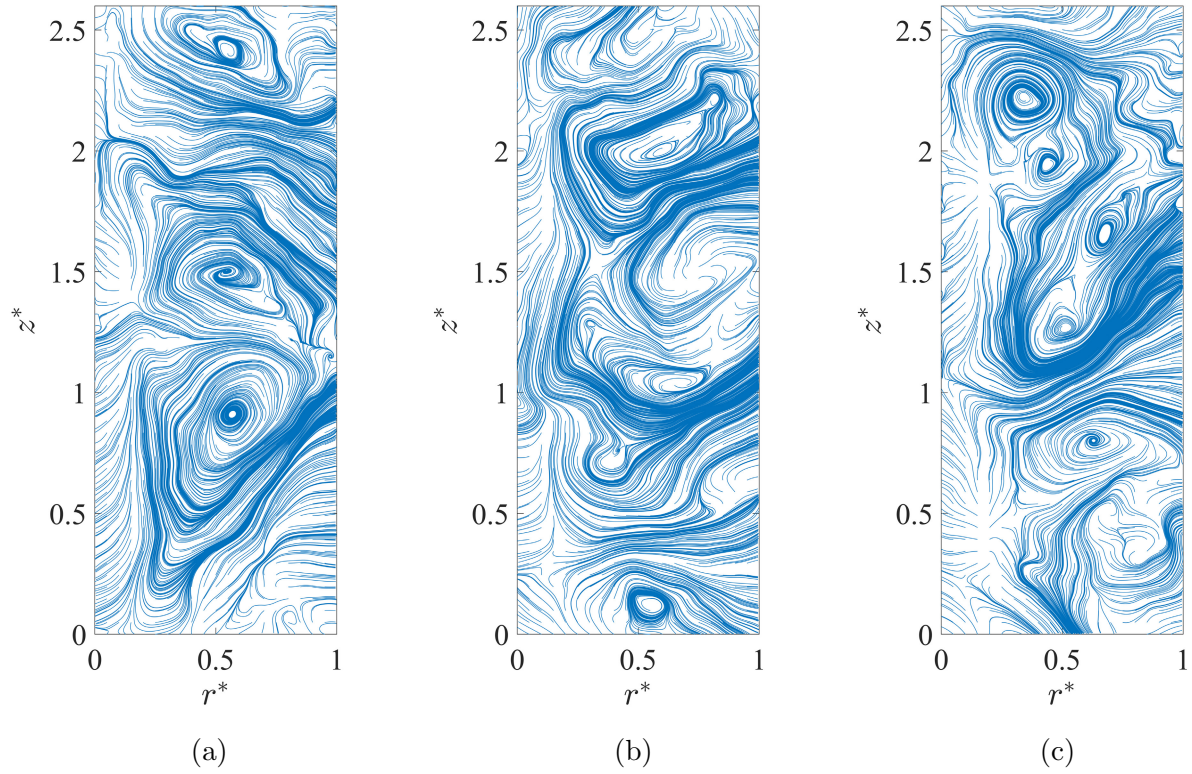


Figure 3.7: Plot of streamlines of turbulent Taylor-Couette vortical structures for PAM-400ppm at  $\text{Re} = 1.50 \times 10^4$ . (a-c) Streamlines of instantaneous velocity  $\mathbf{U}(U_r, U_z)$ .

structures, leading to deformation for large-scale structures over time.

## 3.5 Turbulence Statistics

### 3.5.1 Radial and Axial Fluctuation Statistics

The second-order statistics of variance and covariance of velocity fluctuation was investigated.

The Reynolds stress tensor with a constant density is given by the form:

$$\overline{\tau_{ij}} = \langle u_i u_j \rangle_N, i, j = 1, 2, 3. \quad (3.12)$$

The two in-plane velocity fluctuations  $\langle u_r^2 \rangle_N / U_{ref}^2$  and  $\langle u_z^2 \rangle_N / U_{ref}^2$ , which corresponds to the radial and axial components of Reynolds normal stresses, were investigated for three solutions as shown in Figure 3.8 to 3.10.

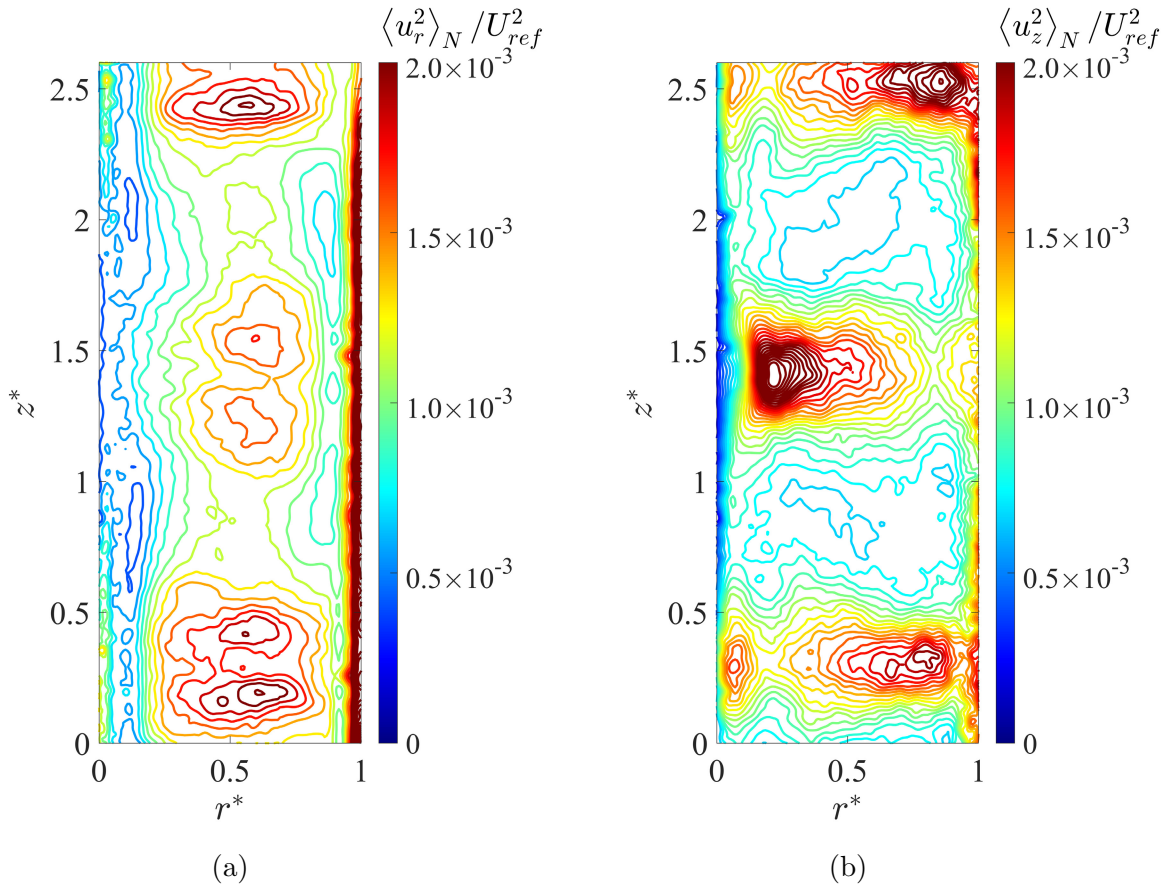


Figure 3.8: Plot of second order statistics of water at  $Re = 1.50 \times 10^4$ . (a) Contour of variances of radial velocity  $\langle u_r^2 \rangle_N / U_{ref}^2$ . (b) Contour of variances of axial velocity  $\langle u_z^2 \rangle_N / U_{ref}^2$ .

Figure 3.8a shows the distributions  $\langle u_r^2 \rangle_N / U_{ref}^2$  of water. It can be seen that most of the

variances occur at locations close to the radial jets and the inner cylinder wall. The radial jet flow structures resemble the free jet flow turbulent structures, where the velocity at the centreline reaches its maximum due to the highest kinetic energy at the centre. The velocity decreases rapidly as moves away from the centerline, and thus leads to the formation of a shear layer around the jet (Pope 2001). It has been found that the shear layer is important in terms of contributing to turbulence production (Johansson *et al.* 1991; Rogers and Moin 1987). Also, it is found that the magnitude of variances is larger at the outer jet region ( $z^* = 0.25$ ) than the inner jet ( $z^* = 1.40$ ). This coincides with the previous finding that the outer jet has larger momentum since it brings high-momentum fluid from the inner cylinder. Thus the jet intensity is greater than the inner jet, and therefore generates stronger shear around.

Figure 3.8a shows that at the axial location where the maximum mean radial velocity occurs, the variance of radial velocity is relatively small compared to its adjacent regions axially. The distribution of  $\langle u_z^2 \rangle_N / U_{ref}^2$  is shown in Figure 3.8b. The regions highlighted are where strong oscillations of axial velocity occur. The separation and convergence of radial jets at the vortex boundaries causes a large magnitude of variance of axial velocity  $\langle u_z^2 \rangle_N / U_{ref}^2$ .

Figure 3.9a shows the radial variance distributions  $\langle u_r^2 \rangle_N / U_{ref}^2$  of PAM-200 ppm. It can be seen that most of the radial velocity variances are concentrated against the inner cylinder, and are also found to reach the local maximum in the bulk flow. The magnitude of the variances is mitigated and smeared out compared to the Newtonian case. Figure 3.9b show the distribution of axial variance  $\langle u_z^2 \rangle_N / U_{ref}^2$  of PAM-200 ppm solution. The axial variances are mostly concentrated near the wall as well. Since the radial jet separates into two streams flowing in two opposite directions along the  $z$ -direction when it is close to the wall, and usually the jet separation leads to a large variance of axial velocity. Similarly, the location where the borders of two vortices converge together close to the wall has large magnitude of axial velocity variance. From Figure 3.9b, it can be seen that the separation and convergence motions close to the wall can still be captured, but the magnitude is reduced compared to

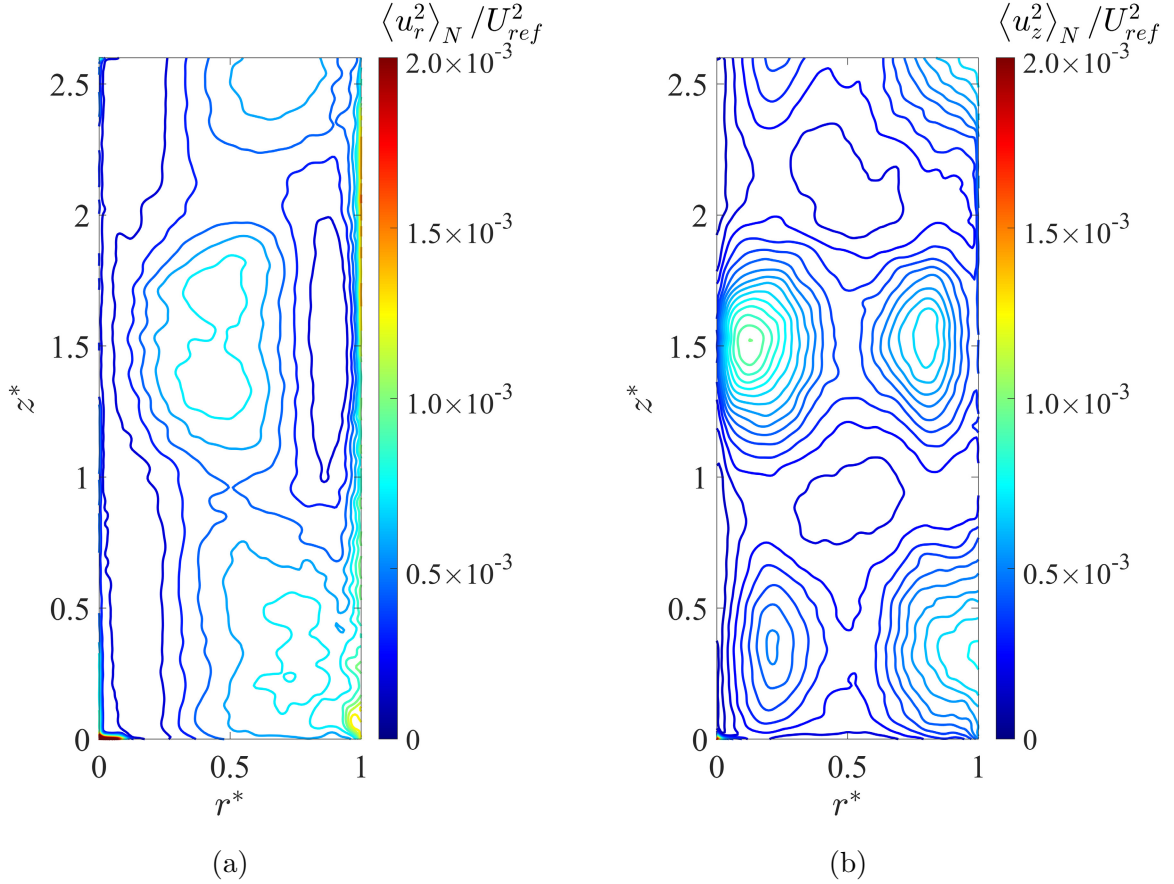


Figure 3.9: Plot of second-order statistics of PAM-200 ppm at  $Re = 1.50 \times 10^4$ . (a) Contour of variances of radial velocity  $\langle u_r^2 \rangle_N / U_{ref}^2$ . (b) Contour of variances of axial velocity  $\langle u_z^2 \rangle_N / U_{ref}^2$ .

the Newtonian case.

Figure 3.10a shows the distributions  $\langle u_r^2 \rangle_N / U_{ref}^2$  of PAM-400 ppm. Similar to PAM-200 ppm, the radial velocity variance is concentrated against the inner cylinder. Figure 3.10b shows that the axial velocity variance  $\langle u_z^2 \rangle_N / U_{ref}^2$  is mitigated further compared to PAM-200 ppm and is smeared out in the axial direction. This aligns with the previous findings that shear-thinning polymer decreases the wall-normal ( $r$ ) and spanwise ( $z$ ) turbulence intensities in wall-bounded flows (Zadrazil *et al.* 2012). Besides, it is interesting to notice that the contour lines are almost straight in the  $z$  direction, indicating both these two  $2^{nd}$  order central moments are almost invariant under a shift in the axial direction. This suggests the shear-thinning effect increases the statistical homogeneity in the axial direction in T-C turbulence

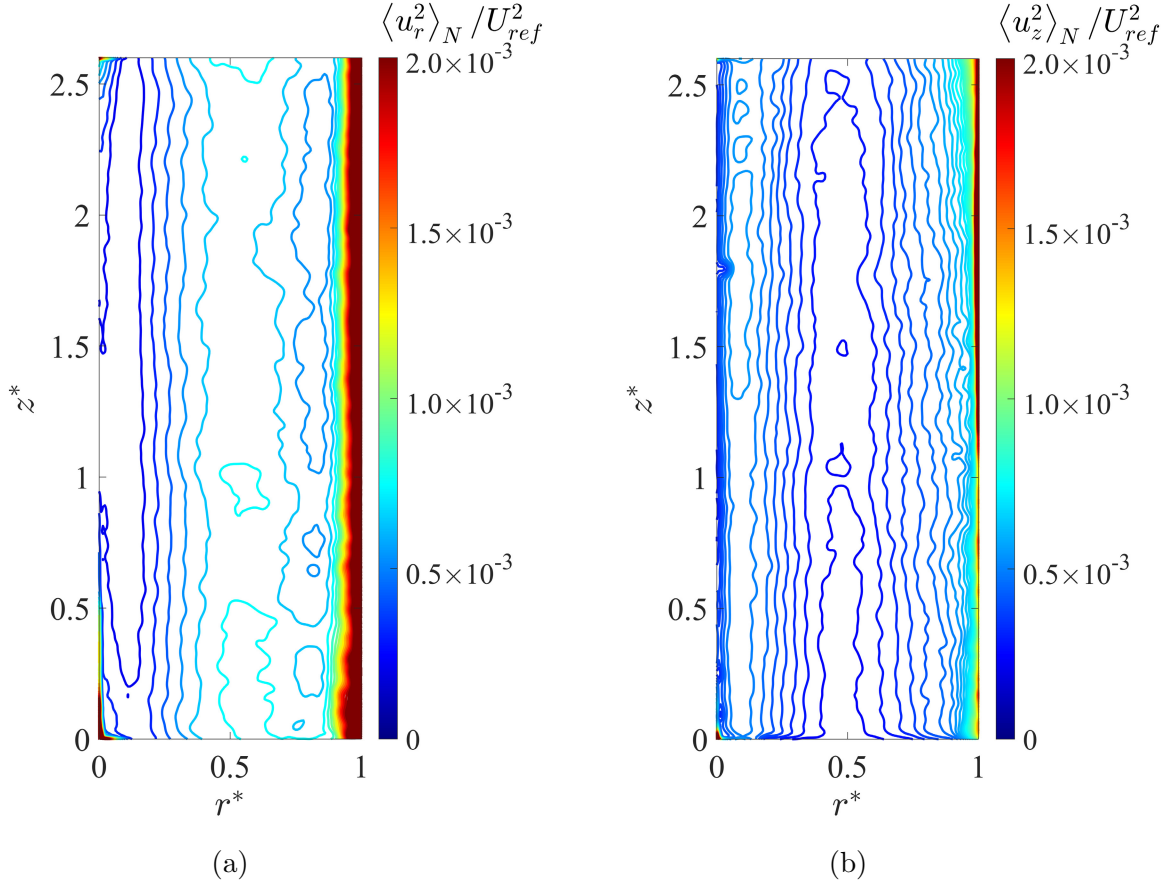


Figure 3.10: Plot of second-order statistics of PAM-400 ppm at  $Re = 1.50 \times 10^4$ . (a) Contour of variances of radial velocity  $\langle u_r^2 \rangle_N / U_{ref}^2$ . (b) Contour of variances of axial velocity  $\langle u_z^2 \rangle_N / U_{ref}^2$ .

and makes the secondary flow behave like ‘laminar’. The observations above coincide with the previous findings that shear-thinning polymer is able to compact the shear effect into smaller volumes in the axial direction, and under the influence of secondary vortices, the shear gets spread axially and leads to a statistically homogeneous state of turbulence in the axial direction. However, along the radial direction, the statistics are observed not homogeneous due to the inherent nature of the existence of shear in T-C turbulence in the radial direction.

### 3.5.2 Reynolds Shear Stress Statistics

There are three combinations of Reynolds shear stresses  $\overline{\tau_{ij}}$ , namely  $\langle u_r u_\theta \rangle_N$ ,  $\langle u_r u_z \rangle_N$  and  $\langle u_\theta u_z \rangle_N$  in T-C cylindrical coordinates. In a wall-bounded turbulence, the production term

that describes the generation of turbulence kinetic energy can be expressed as:

$$P_k = -\rho \langle u_i u_j \rangle \frac{\partial U_i}{\partial x_j}. \quad (3.13)$$

It can be seen that the shear stresses are closely related to turbulence production. It is worth mentioning that in most of the wall-bounded flows where the walls are stationary, and under the effect of a boundary layer profile, the covariance of velocity (Reynolds shear stress) formed by streamwise and wall-normal fluctuation components is negative, as shown in Figure 3.11a. In Taylor-Couette flows, the production is generated by the inner cylinder, thus the covariance formed by streamwise and wall-normal fluctuation components is positive as shown in Figure 3.11b.

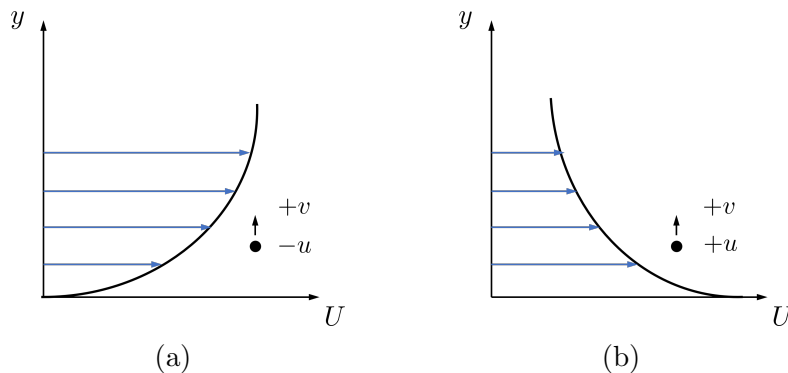


Figure 3.11: Schematic of demonstration of the sign of  $u_i u_j$  in streamwise-wall-normal direction. (a) stationary wall-bounded flows (b) moving wall-bounded flows.

Since the gradient of azimuthal velocity along radial direction, i.e.,  $dU_\theta/dr$  in T-C flow always exists, it might be of interest to only investigate the distributions of Reynolds shear stresses term  $\langle u_r u_\theta \rangle_N$ . Figure 3.12 shows the  $\langle u_r u_\theta \rangle_N$  for water, PAM-200 ppm, and PAM-400 ppm. For water, it can be seen that  $\langle u_r u_\theta \rangle_N$  is mostly concentrated close to the inner wall and at the region where borders of neighboring vortices merge. Two local maximums of  $\langle u_r u_\theta \rangle_N$  can be found adjacent to the jet. PAM-200 ppm shows a similar pattern, the magnitude of  $\langle u_r u_\theta \rangle_N$  is reduced, and only one local maximum is observed. PAM-400 ppm shows the Reynolds shear stress distribution is mainly concentrated at the inner cylinder wall and gradually reduces towards the outer cylinder.

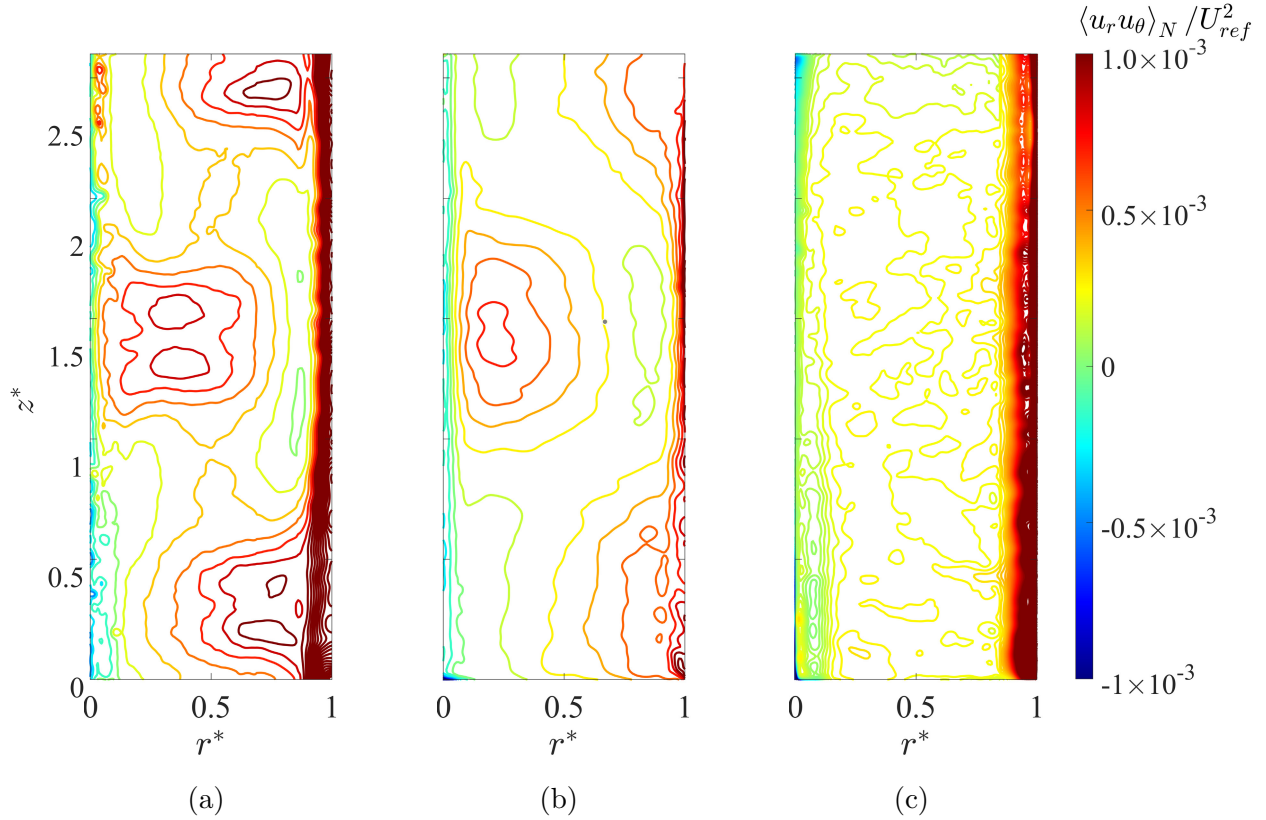


Figure 3.12: Plot of statistics  $\langle u_r u_\theta \rangle_N$  in the  $r - z$  plane for (a) water, (b) PAM-200 ppm, and (c) PAM-400 ppm.

Figure 3.13 shows the fluctuation statistics  $u_r u_\theta$  in the  $r - z$  plane for water, PAM-200ppm, and PAM-400ppm. Regions for which  $u_r u_\theta$  is greater than  $\langle u_r u_\theta \rangle_N$  is denoted by the enclosed contours (for  $u_r < 0$  the region is enclosed with solid lines, and for  $u_r > 0$  the region is enclosed with dashed lines). The statistics  $u_r u_\theta > \langle u_r u_\theta \rangle_N$  can be appreciated as the structures that actively contribute to the production of turbulence (Warholic *et al.* 2001). These structures with high momentum transfer the kinetic energy with fluid regions of low kinetic energy. It can be seen that for water in Figure 3.13a, the structures mainly responsible for turbulence generation are mostly concentrated at the inner wall and around the jets. These are also the regions where more shear occurs. The structures in the central region are relatively large in size. Distinct features could be found by comparing Newtonian and non-Newtonian solutions. Figure 3.13b shows for 200 ppm, a few bulk structures are observed in the middle. The number of small-scale structures is significantly reduced compared to

Newtonian in the central region. As the concentration increases, PAM-400 ppm similarly shows a reduced number of small-scale structures, which indicates the activity of turbulent production by small-scale structures is dampened induced by the shear-thinning polymer. The distribution of large structures becomes more irregular in space, that they can be more concentrated and sparsed as shown in Figure 3.13c.

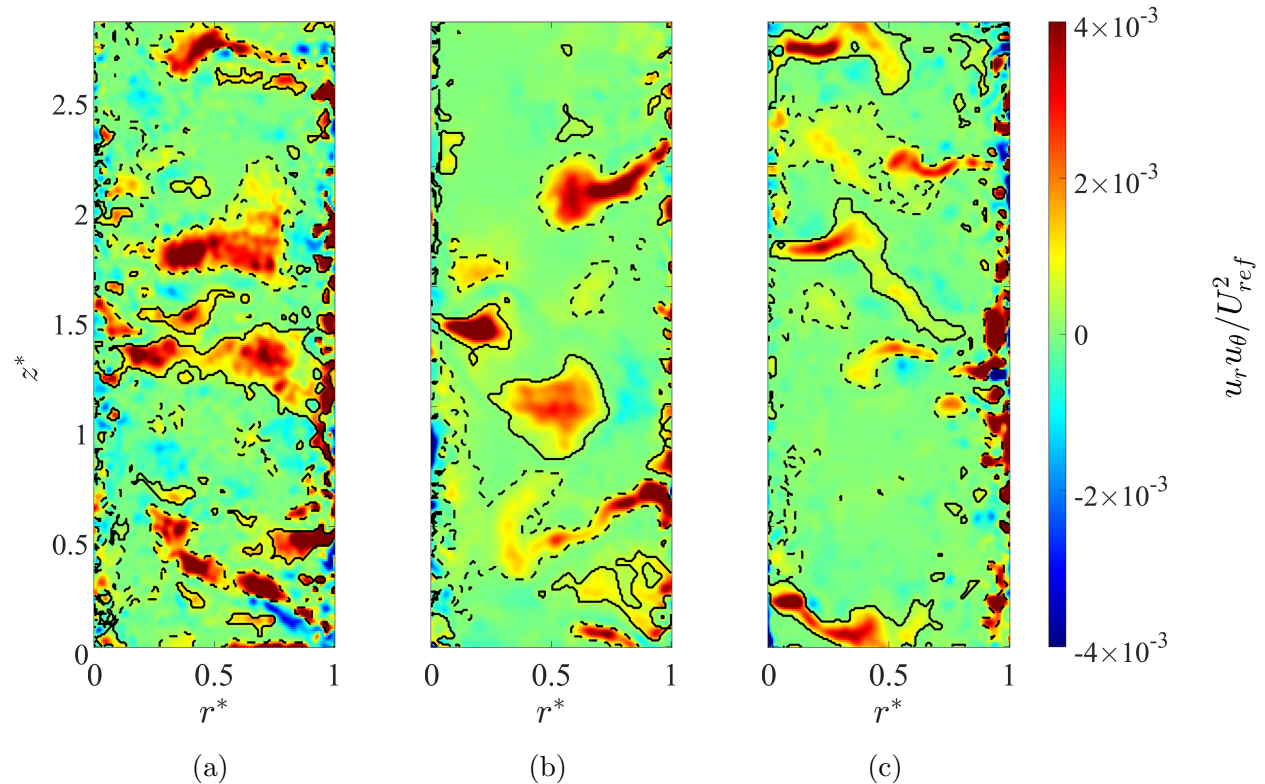


Figure 3.13: Plot of example of fluctuation statistics  $u_r u_\theta$  in the  $r - z$  plane for (a) water, (b) PAM-200ppm, and (c) PAM-400ppm. Regions that  $u_r u_\theta$  is greater than  $\langle u_r u_\theta \rangle_N$  is highlighted (for  $u_r < 0$  the region is enclosed with solid lines, and for  $u_r > 0$  the region is enclosed with dashed lines).

### 3.6 Radial Jet Instability

Taylor vortices are situated between radial jets, and the instabilities and motions of the radial jets have a significant influence on the shape and positions of the vortices. An examination of radial jet motion and intensity to demonstrate the temporal evolution of radial velocity

was performed. The spatial average of the radial velocity, denoted as  $\langle U_r \rangle_r$ , was obtained by averaging radial velocity  $U_r$  in the radial direction.

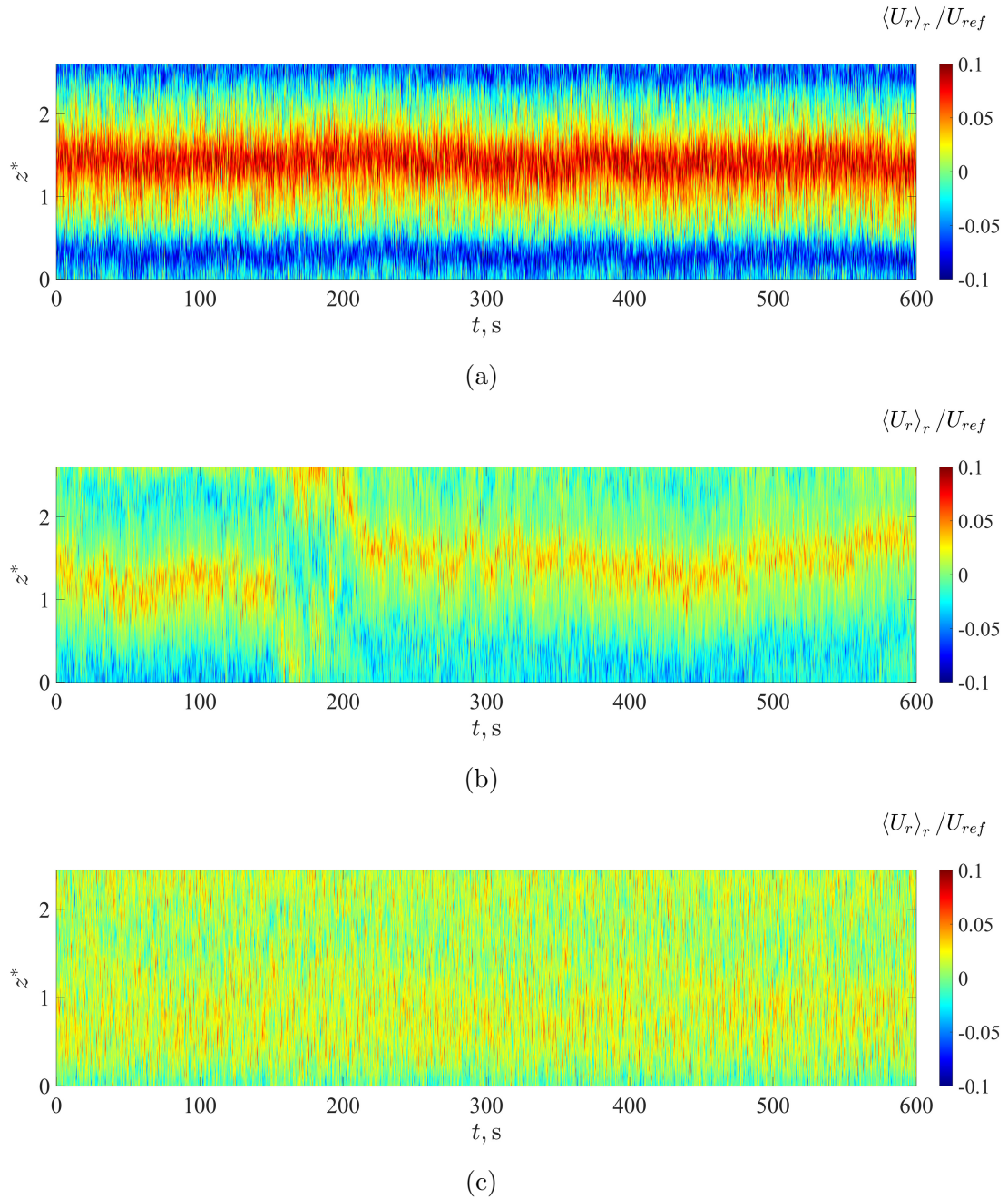


Figure 3.14: Plot of time evolution of radially-averaged quantity  $\langle U_r \rangle_r$  at  $Re = 1.50 \times 10^4$ . (a)Water. (b)PAM-200 ppm. (c)PAM-400 ppm .

The temporal evolution of the averaged radial velocity of three fluids under the same Reynolds number  $Re = 1.50 \times 10^4$  is shown in Figure 3.14. For the purpose of comparison,

the same length of 3000 radially-averaged instantaneous snapshots of  $\langle U_r \rangle_r$  are presented with an entire time span of 600 s. It can be seen that despite under the same nominal Re, the variations of  $\langle U_r \rangle_r$  are quite different. For water solution, an inward jet and two outward jets are captured. They all show a strong jet intensity. PAM-200 ppm solution exhibits reduced jet intensity compared to the Newtonian case, The PAM-400 ppm case demonstrates a strong turbulent motion in the  $r - z$  direction, with attenuated jet intensity. It can be concluded that within the turbulent Taylor-Couette regime and under the current definition of Re, an increase in the nonlinear viscosity effect results in reduced jet intensity and more complex flow regimes.

### 3.7 Vorticity Magnitude

The vorticity magnitude was investigated for the mean flow of water and PAM-200 ppm solutions. The vorticity vector can be calculated by taking the curl of the velocity vector:

$$\boldsymbol{\omega} = \nabla \times \mathbf{U}. \quad (3.14)$$

The  $\theta$ -direction vorticity component is expressed as shown below:

$$\omega_\theta = \frac{\partial U_r}{\partial z} - \frac{\partial U_z}{\partial r}. \quad (3.15)$$

The ensemble-averaged azimuthal vorticity  $\langle \omega_\theta \rangle_N$  is calculated:

$$\langle \omega_\theta \rangle_N = \frac{\partial \langle U_r \rangle_N}{\partial z} - \frac{\partial \langle U_z \rangle_N}{\partial r}. \quad (3.16)$$

Figure 3.15 shows the  $\langle \omega_\theta \rangle_N$  distribution for both water and PAM-200 ppm solution at  $\text{Re} = 1.50 \times 10^4$ .  $\langle \omega_\theta \rangle_N$  was normalized by the angular velocity of the inner cylinder  $\omega_i$ .

Observations reveal distinctions in normalized azimuthal vorticity magnitudes between Newtonian and shear-thinning fluids at  $\text{Re} = 1.50 \times 10^4$ . The Newtonian fluid exhibits a greater vorticity magnitude in the regions where the mean Taylor vortices are located, contrasting with a significant reduction in the azimuthal vorticity  $\omega_\theta$  for the PAM-200 ppm

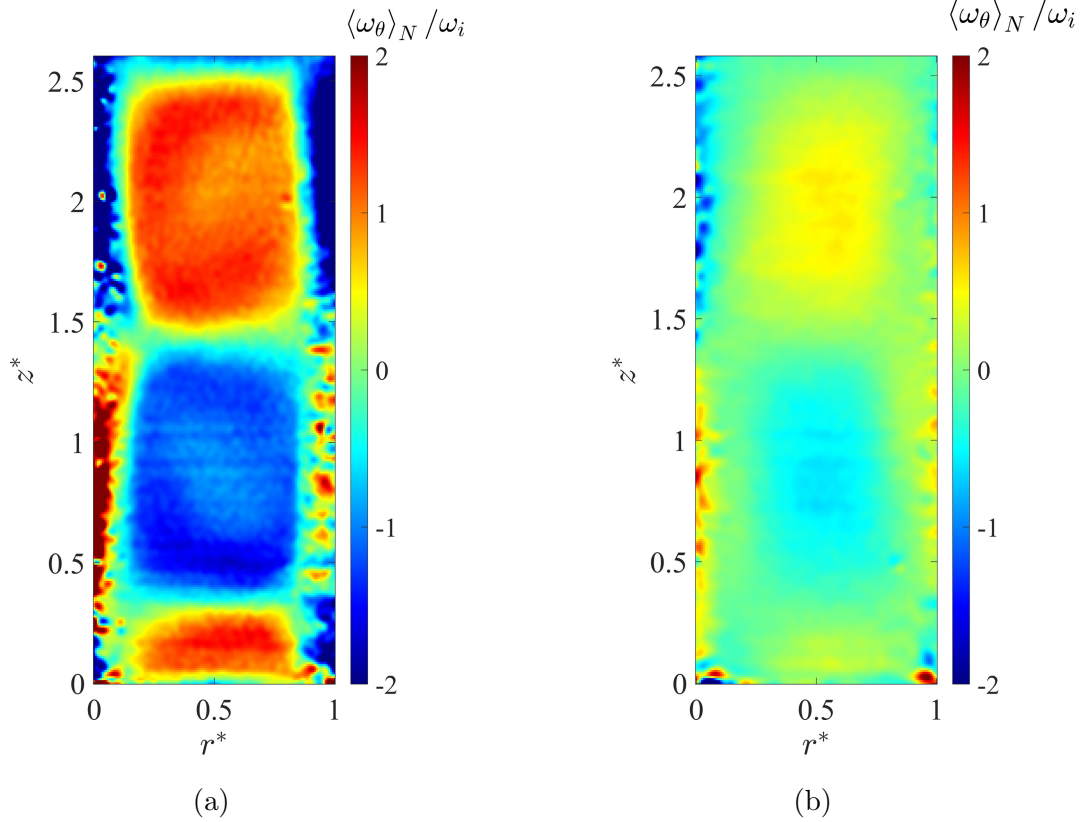


Figure 3.15: Plot of contour of ensemble-averaged azimuthal vorticity  $\langle \omega_\theta \rangle_N$  distribution. (a) Water,  $\text{Re} = 1.50 \times 10^4$ . (b) PAM-200 ppm,  $\text{Re} = 1.50 \times 10^4$ .

solution. This suggests the capacity of shear-thinning fluids to mitigate the secondary vorticity associated with secondary flows. The results show that rheological properties of fluids are important in influencing the dynamics of vortical structures, with shear-thinning characteristics contributing to the attenuation of secondary flow vorticity.

Furthermore, it is noteworthy that, even in the presence of Taylor-Couette vortices, the highest magnitude of vorticity in the azimuthal direction is not observed at the vortex centre but instead occurs at the regions close to the wall of inner and outer cylinders where there is substantial turbulence production. Consequently, the maximum azimuthal vorticity is located close to the walls of both the inner and outer cylinders. The spatial distribution of vortices challenges the applicability of the maximum vorticity method for vortex detection in this context. Therefore, alternative criteria, namely the  $\Gamma_1$  and  $\Gamma_2$  criterion, were adopted, as elaborated in the subsequent section.

## 3.8 Vortex Centre Location, Core Size and Circulation

In turbulent Taylor-Couette flow, the vortex centre and core sizes are constantly changing over time. The characterization of Taylor vortices, including their locations and sizes, is pivotal for comprehending the dynamic nature of vortex motion. A vortex detection algorithm based on  $\Gamma_1$  and  $\Gamma_2$  criterion was implemented. following the study by Graftieaux *et al.* (2001). This vortex identification approach involves vortex centre location detection and vortex core size detection, respectively based on the scalar quantity  $\Gamma_1$  and  $\Gamma_2$ . This vortex detection approach has the advantage of eliminating the small-scale turbulent intermittency which is superimposed on the large-scale vortices, and has been proven robust in various vortex detection applications (De Gregorio and Visingardi 2020). This vortex identification algorithm was implemented to the entire datasets of instantaneous in-plane velocity fields to get the ensemble vortices information.

### 3.8.1 Vortex Centre location

The vortex centre detection is based on scalar quantity  $\Gamma_1$  which is given by (Graftieaux *et al.* 2001):

$$\Gamma_1(P) = \frac{1}{S} \iint_S \sin(\theta_M) dS, \quad (3.17)$$

where  $P$  is a center point located within the region of measurement.  $S$  is a rectangular domain of a certain size where  $P$  is centered.  $\theta_M$  is the angle between radius vector  $\overrightarrow{PM}$  and any arbitrary velocity vector  $\overrightarrow{U_M}$  inside domain  $S$ . Thus:

$$\sin(\theta_M) = \frac{\|\overrightarrow{PM} \times \overrightarrow{U_M}\|}{\|\overrightarrow{PM}\| \|\overrightarrow{U_M}\|}, \quad (3.18)$$

where symbol  $\times$  represents the cross product, and  $\|\cdot\|$  represents the magnitude (or Euclidean norm) of the vector.

From Equation 3.17 it can be seen that  $\Gamma_1$  is bounded by 1. For an ideal circular vortex,  $\Gamma_1 = 1$  if  $P$  is at the vortex centre and the radius vector  $\overrightarrow{PM}$  is perpendicular to all the

velocity vectors  $\vec{U}_M$ .

Computationally Equation 3.17 is computed by:

$$\Gamma_1(P) = \frac{1}{N} \sum_S \frac{\left\| \overrightarrow{PM} \times \vec{U}_M \right\|}{\left\| \overrightarrow{PM} \right\| \left\| \vec{U}_M \right\|}, \quad (3.19)$$

where  $N$  is the number of points within domain  $S$ . A threshold of  $\Gamma_1 > 0.9$  was set as a prescreen condition to define a vortex, and vortex core was defined to be the local maximum of  $\Gamma_1$  (Graftieaux *et al.* 2001). It has been found that the value of  $N$  can be extremely useful for removing fine-scale fluctuations and make  $\Gamma_1$  an integral quantity, which helps remove noise and increase the accuracy of vortex detection (Graftieaux *et al.* 2001).

The algorithm successfully identified vortex centre locations of all instantaneous velocity fields over the entire time span. The number of vortices detected per instantaneous snapshot differed for water, PAM-200 ppm, and PAM-400 ppm solutions, with values of 2.3, 2.4, and 3.9, respectively. This suggests that for Newtonian solutions, the primary vortex motion is Taylor vortices, whereas for non-Newtonian fluid, the large-scale vortices undergo deformation and are broken up into smaller structures induced by the shear-thinning effect, which leads to a higher average number of vortices per frame detected.

The scatter plot of vortex centres for Newtonian and non-Newtonian solutions are shown in Figure 3.16a-3.16c below. Kernel probability density estimate was used for scatter points of vortex centres to indicate regions of higher probability density in space. This method assigns a probability density to each data point and smooths them to get a continuous surface of probability density, allowing for emphasis of areas with higher vortex centre concentrations.

Figure 3.16a shows the distribution of vortex centres of water. It can be seen that vortex centres are dominantly concentrated in three distinct regions: two within the Taylor vortex cells and one positioned at the jet location near the outer cylinder wall. The primary vortices show relatively fixed locations of distribution, which is attributed to the finite length of the apparatus and the boundary conditions imposed by the top and bottom plates. The vortex centres that cluster at the jet corresponds to the previously mentioned smaller vortices, whose

emergence is attributed to the shear between the primary motions. The spatial distribution of vortex centres for the primary Taylor vortices is noted to center around the ensemble-mean vortex centre locations. Each distribution exhibits an elliptical spatial distribution for both Taylor vortices captured as shown in Figure 3.16a, with a longer axis in the  $z$  direction and a comparatively shorter one in the  $r$  direction. This observation suggests a higher degree of freedom in the axial motions of the Taylor vortices. The long axis for the upper vortex is slightly tilted, whereas the lower one is more perpendicular, indicating motions of these two neighboring Taylor vortices are not identical and mirrored about the jet. The two primary vortex centre regions are clearly separated, indicating vortices do not trespass over the radial jet. Due to the end effect of boundary conditions by the top and bottom plates as well as the inner and outer cylinder walls, the observed Taylor vortices meander a little, but their large sizes lock them in place because of the apparatus geometry.

For PAM-200 ppm, Figure 3.16b shows that the distribution of vortex centres is mainly concentrated in the central region and forms a long thin distribution along the axial direction. Here the radial jet intensity is lower than for Newtonian flow. This causes the partition effect of the radial jet for neighboring Taylor vortices is reduced, giving them more ability to meander and not create a repeatable core anchored in one place. Thus, the motion between neighboring vortices is less restricted, and so the vortex centre distribution smears out the border of neighboring vortices as shown in Figure 3.16b.

For PAM-400 ppm, a wider distribution in both radial and axial direction is observed, indicating even more stochastic movement of the vortex cores; this is induced by the shear-thinning effect.

### 3.8.2 Vortex Core Size

Instantaneous vortex core size was determined by  $\Gamma_2$ , which is another scalar quantity based on  $\Gamma_1$  but considering an extra convection velocity  $U_P$  (Graftieaux *et al.* 2001) to account for the effects of fluid motion or convection on the vortex characteristics. Vortices in fluid dynamics are often influenced by the flow field, the convection velocity represents the speed

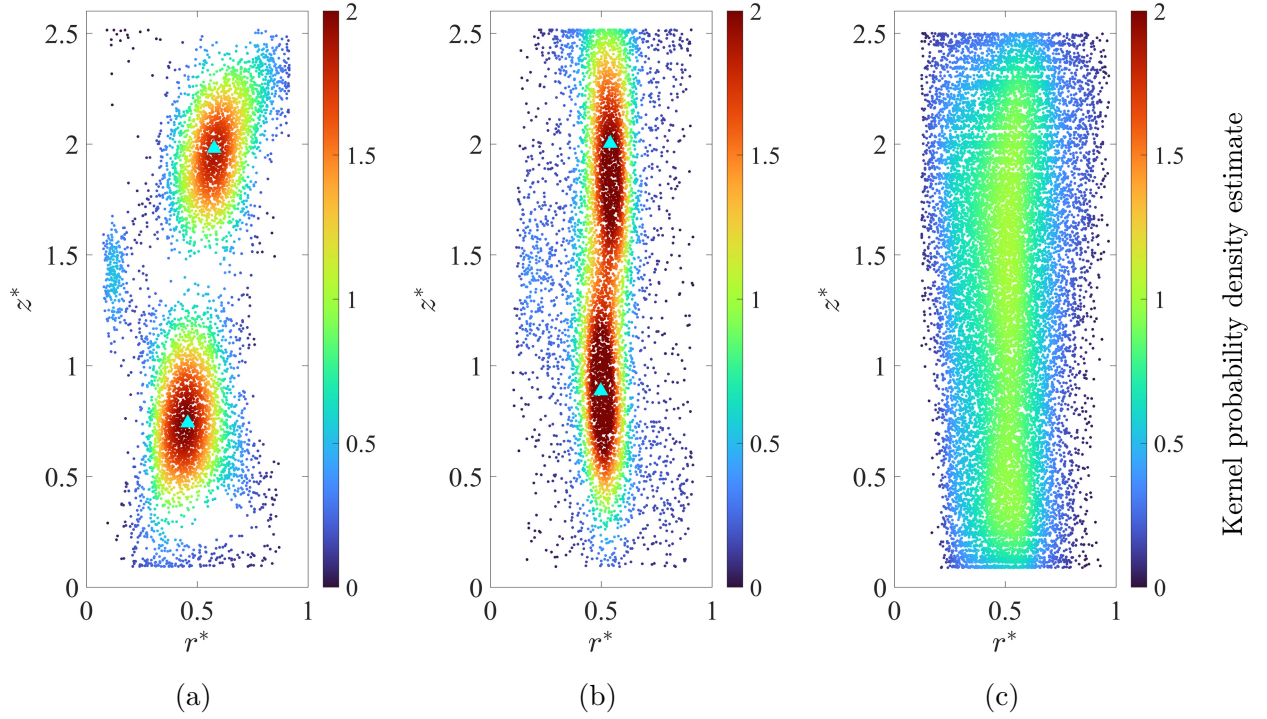


Figure 3.16: Plot of scatter of spatial distributions of vortex centre locations at  $\text{Re} = 1.50 \times 10^4$ . The scatter of vortex centre locations is colored by Kernel probability density estimate. The triangles indicate the ensemble-mean vortex centre locations. (a) Water. (b) PAM-200 ppm. (c) PAM-400 ppm.

at which the vortices are being transported by the overall flow.  $\Gamma_2$  is given by:

$$\Gamma_2(P) = \frac{1}{S} \iint_S \frac{\left\| \overrightarrow{PM} \times (\overrightarrow{U}_M - \overrightarrow{U}_P) \right\|}{\left\| \overrightarrow{PM} \right\| \left\| (\overrightarrow{U}_M - \overrightarrow{U}_P) \right\|} dS, \quad (3.20)$$

where the local convection velocity  $\overrightarrow{U}_P$  is computed by averaging the surrounding velocity vector within domain  $S$ :

$$\overrightarrow{U}_P = \frac{1}{S} \iint_S \mathbf{U} dS. \quad (3.21)$$

It has been shown that  $\Gamma_2$  is a local scalar quantity that only depends on local strain rate  $D_{ij}$  and rotation  $\Omega_{ij}$ , which are the symmetric and anti-symmetric parts of the velocity gradient tensor (Graftieux *et al.* 2001). It is found that if  $|\Omega/D| > 1$ , the flow is dominant by the rotation, and  $|\Gamma_2| > 2/\pi$  (Graftieux *et al.* 2001), which defines the vortex core size.

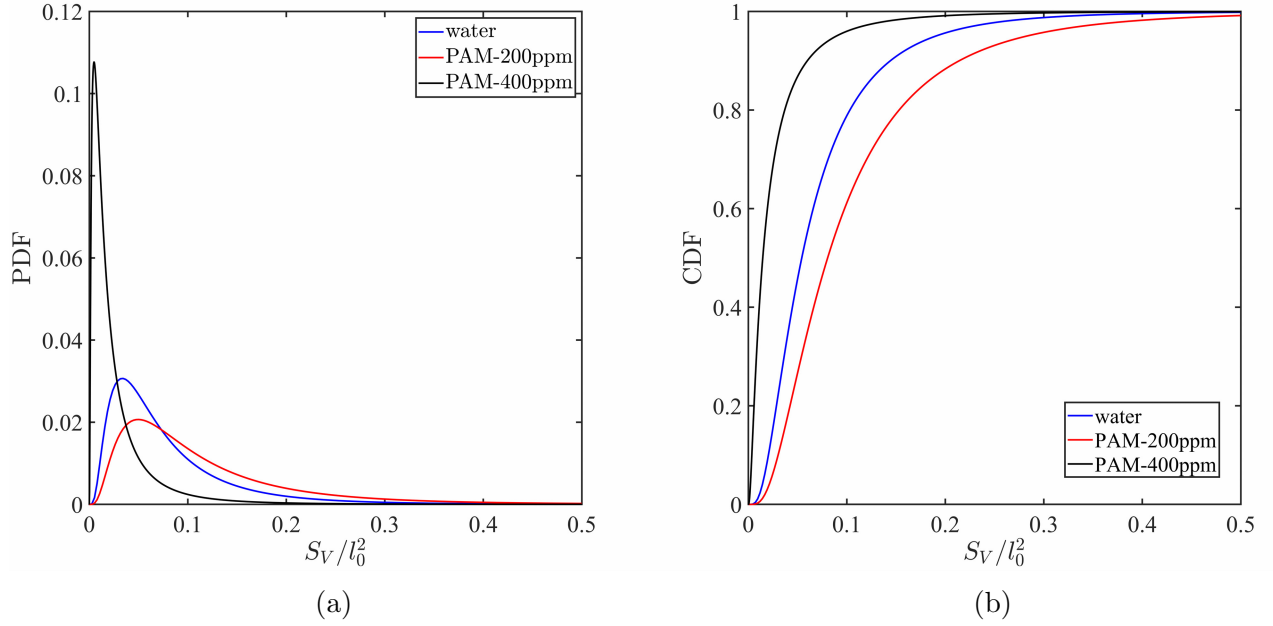


Figure 3.17: Plot of the probability density function of vortex core sizes. (a) Lognormal probability density function (PDF) of vortex sizes. (b) Lognormal probability cumulative density function (CDF) of vortex core sizes.

Figure 3.17 shows the fitted lognormal distribution and cumulative density distribution of vortex core sizes for the three fluids. A lognormal distribution function was used to fit the data. Vortex core size  $S_V$  found by the algorithm was normalized by the square of characteristic lengthscale  $l_0$ .  $l_0$  was selected as the gap width  $d$ , i.e.,  $l_0 = d = 19.1$  mm. Table 3.2 summarizes the mean and standard deviation of distributions for three fluids. PAM-200 ppm shows almost the same mean size and standard deviation of vortex centres. PAM-400 ppm solution exhibits a decrease in mean vortex core size and a larger standard deviation compared to water.

Table 3.2: Mean and standard deviation of vortex core sizes for three fluids.

	Water (mm <sup>2</sup> )	PAM-200 ppm (mm <sup>2</sup> )	PAM-400 ppm (mm <sup>2</sup> )
$\mu$	3.127	3.522	1.819
$\sigma$	0.763	0.764	1.094

### 3.8.3 Circulation

The circulation of a vortex  $\Gamma_S$  is defined (Davidson 2015):

$$\Gamma_S = \oint_C \mathbf{U} \cdot d\mathbf{l}, \quad (3.22)$$

where  $C$  is a curve that encircles the vortex determined by the threshold of  $|\Gamma_2| > 2/\pi$ . According to Stokes' theorem, the line integral of velocity is equal to the surface integral of the curl of  $U$  over the surface  $S$  that  $C$  encircles:

$$\Gamma_S = \iint_S \omega_\theta \cdot d\mathbf{S}, \quad (3.23)$$

and the discretized form of Equation 3.23 used for numerical computation is given by:

$$\Gamma_S = \sum_{i=1}^N \sum_{j=1}^M \omega_\theta(i, j) \times d\mathbf{S}, \quad (3.24)$$

where  $\omega_\theta$  is the azimuthal vorticity value at position  $(i, j)$  within the vortex area,  $N$  and  $M$  are the dimensions of the vorticity field matrix, and  $d\mathbf{S}$  is the differential area. So computationally, it is summing up the vorticity values within the vortex region and then multiplying by the differential area to obtain the circulation. Figure 3.18 shows the histogram distribution of the magnitude of circulation for water, PAM-200 ppm and PAM-400 ppm. It can be seen that the distribution for all three solutions is roughly symmetric about  $\Gamma_S = 0$ , meaning the probability of clockwise and counterclockwise rotating vortices occurring are close within the FOV. For water, the circulation is mainly concentrated at  $3 \times 10^{-4} \text{ m}^2/\text{s} < |\Gamma_s| < 1.5 \times 10^{-3} \text{ m}^2/\text{s}$ . This range of circulation can be considered as the range where Taylor vortex circulation mostly concentrated. The percentage of vortices with the circulation within this range is 28.8%. PAM-200 ppm shows a similar trend of distribution of  $\Gamma_S$ , however, the percentage of vortices within the same range of circulation is reduced to 23.8%. PAM-400 ppm shows that the mean circulation is reduced significantly, besides, the percentage of vortices within the same range of circulation is reduced to 17.0%.

The distribution of PAM-200 ppm in the middle looks like a linear combination of Figure 3.18(a) and Figure 3.18(c).

Overall, it can be concluded that the addition of shear-shearing polymer tends to reduce the proportion of circulation of Taylor vortices compared to Newtonian flow.

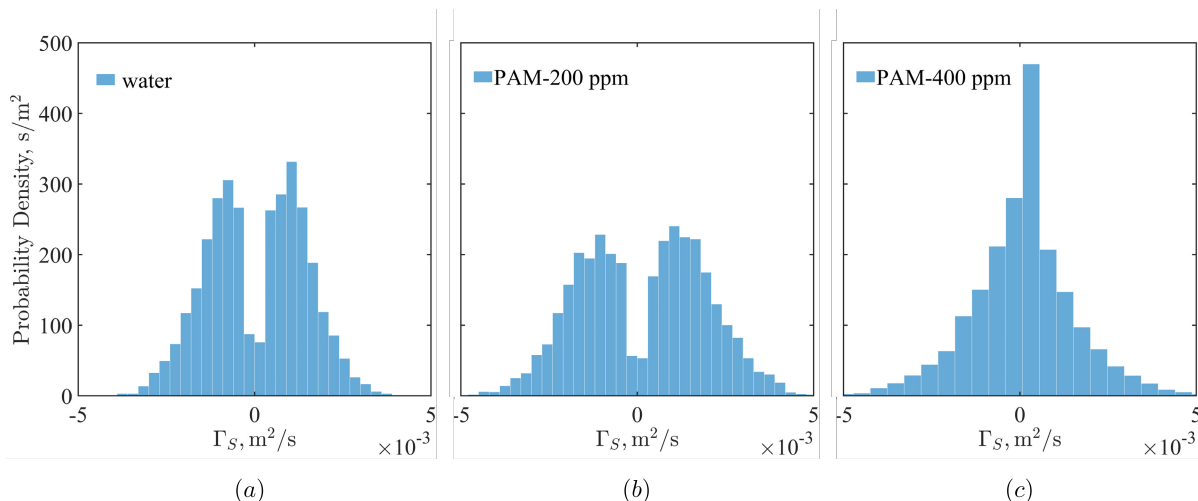


Figure 3.18: Probability density histogram of the magnitude of circulation for (a) water. (b) PAM-200 ppm. (c) PAM-400 ppm.

### 3.9 Spatial Organization of Energetic Modes

In this study, proper Orthogonal Decomposition (POD) was implemented to understand the spatial coherent structures. POD is a dimensionality reduction technique widely used in various fields, including fluid dynamics, structural mechanics, image processing, and data analysis. POD is a mathematical tool that aims to extract the dominant modes or patterns from a dataset, reducing its complexity while preserving its essential features (Brunton and Kutz 2022). Proper Orthogonal Decomposition exists for any given matrix. The decomposition is based on the singular value decomposition (SVD), which can be performed on any matrix, square or rectangular.

POD is able to decompose the data matrix into orthogonal basis sets and their corresponding temporal coefficients. This decomposition results in the extraction of dominant eigenmodes and their corresponding temporal coefficients as shown below (Sirovich 1987):

$$u(x, t) = \sum_{k=1}^N a^k(t) \phi^k(x), \quad (3.25)$$

where  $u(x, t)$  is the velocity fluctuation,  $a(t)$  is temporal coefficient, and  $\phi(x)$  is spatial mode matrix.  $\phi(x)$  is a basis set that contains a collection of spatial modes, i.e., eigenmodes. They represent the most significant variations within the data. These modes are essentially a set of orthogonal vectors that capture the primary patterns in the data. The basis vectors are ordered hierarchically by importance, with the first mode capturing the most significant variation, the second mode capturing the second-most significant variation, and so on. The ‘importance’ is reflected by the magnitude of the eigenvalue. Each mode can be thought of as a spatial shape that characterizes how the flow evolves in space. Lumley (1967) proposed that spatial modes signify coherent structures and the first mode that captures the most of the turbulence kinetic energy often reveals the large coherent structures in the flow.

Snap-shot POD (Sirovich 1987) was implemented to obtain the spatial modes and their corresponding energy and temporal coefficients. Snap-shot POD is a more computationally efficient method compared to the standard Singular Value Decomposition (SVD). The mean of the velocity data was subtracted from each column of the data matrix and a velocity fluctuation field  $\mathbf{D}$  over time could be obtained:

$$\mathbf{D} = [\mathbf{u}_1 \mathbf{u}_2 \dots \mathbf{u}_M], \quad (3.26)$$

where  $\mathbf{u}_i$  indicates the  $i^{th}$  instantaneous velocity fluctuation field in time which contains several velocity directions that are shaped into a single column. By subtracting the mean flow, the data was centered and bias was removed, ensuring that the modes capture variations around the mean. Covariance matrix was computed as:

$$\mathbf{C} = \frac{1}{M} \mathbf{D}^T \mathbf{D}. \quad (3.27)$$

The  $j^{th}$  spatial POD mode was calculated as:

$$\boldsymbol{\phi}_j = \frac{\sum_{m=1}^M A_{m,j} \mathbf{u}_m}{\left\| \sum_{m=1}^M A_{m,j} \mathbf{u}_m \right\|}, \quad j = 1, 2, \dots, r, \quad (3.28)$$

where  $\mathbf{A}_j$  is the  $j^{\text{th}}$  left eigenvector of covariance matrix  $\mathbf{C}$ , and  $r$  is the rank of velocity fluctuation matrix  $\mathbf{D}$ , i.e,  $r = \text{rank}(\mathbf{D})$ .  $A_{m,j}$  denotes the  $m^{\text{th}}$  component of the eigenvector  $\mathbf{A}_j$ .  $\|\cdot\|$  denotes Euclidean norm. It is worth mentioning that  $\boldsymbol{\phi}_j$  is an eigenvector with a unit length after the normalization, i.e.,  $\boldsymbol{\phi}_j = (\phi_{j,r}, \phi_{j,\theta}, \phi_{j,z})$ , and  $\|\boldsymbol{\phi}_j\| = 1$ .

### 3.9.1 Spatial Modes Based on In-plane Velocities

In this section, the two in-plane velocity fluctuation components  $u_r$  and  $u_z$  were incorporated into covariance matrix to understand the coherent turbulent structures in  $r - z$  plane.

The first three dominant modes for water at  $\text{Re} = 1.50 \times 10^4$  are shown in Figure 3.19 and 3.20 below. Notably, the eigenvectors in the first mode exhibit vortical shape structures. These energetic structures have a circular, vortical shape but do not meet the definition of a vortex. It can be appreciated that these vortical-shape energetic structures are the shape of turbulent fluctuations that statistically contribute to most of the turbulence kinetic energy (TKE) (Kostas *et al.* 2005). These vortical structures of velocity fluctuations show a phase lag of  $\pi/2$  in axial direction compared to the spatial location of mean Taylor vortices as shown in Figure 3.5c. The mean flow is related to this POD mode. It has been proven that in the case of implementing the POD without subtracting the ensemble mean, the first mode is an excellent estimate of the flow pattern of the ensemble average (El-Adawy *et al.* 2018). Thus the mean Taylor vortices are the structures of ‘0’ mode revealed using POD (or mode 1 if the mean was not subtracted before forming the covariance matrix). It can be concluded that the mean kinetic energy is mainly representative of the mean Taylor vortex structures, and the TKE is mainly comprised of the vortex-shaped structures shown in the vector plot in Figure 3.20. The two different structures are all circular-shaped, with a phase lag of  $\pi/2$  in the axial direction.

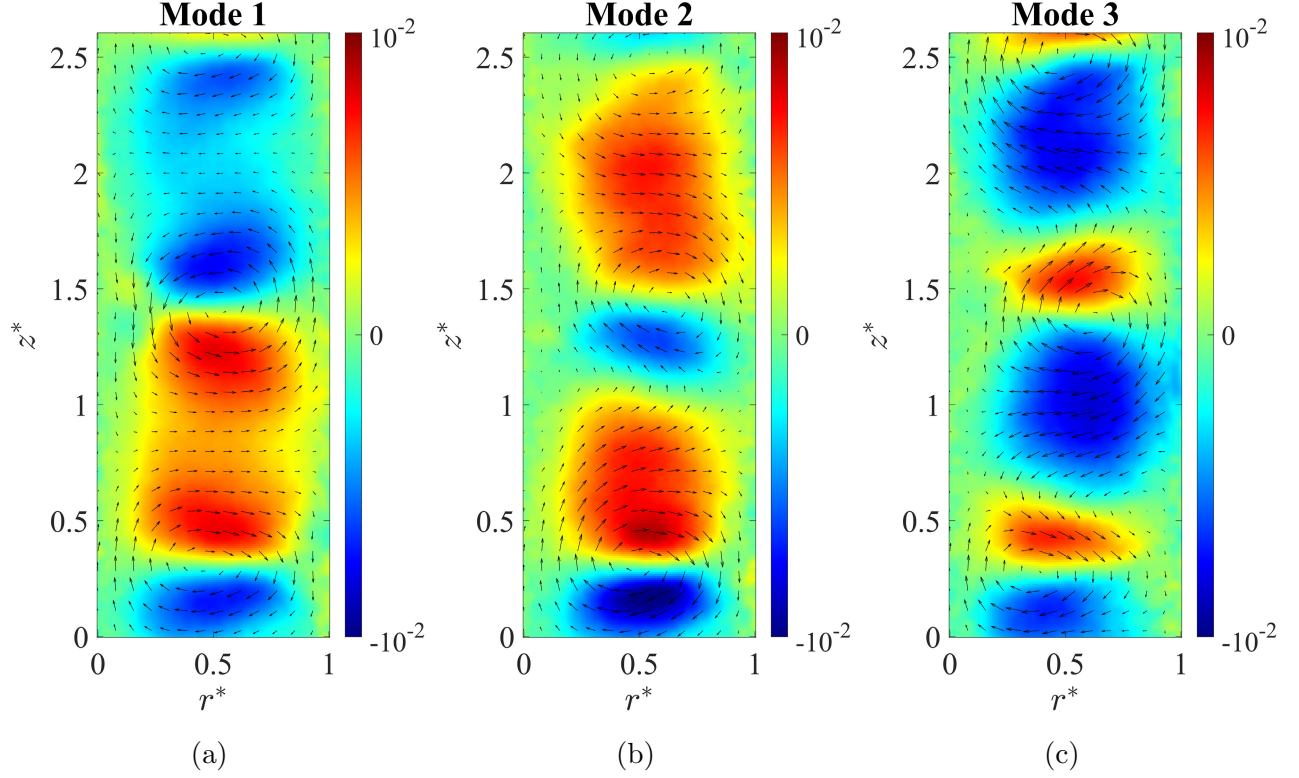


Figure 3.19: Plot of spatial modes of radial velocity fluctuation of water at  $\text{Re} = 1.5 \times 10^4$ . (a) mode 1. (b) mode 2. (c) mode 3. The vector shows  $\phi_j(\phi_{j,r}, \phi_{j,z})$  and background shows the value of  $\phi_{j,r}$ .

The first mode based on the radial velocity for water in Figure 3.19a shows the large-scale coherent structure clusters. As seen, two primary clusters of radial fluctuation are observed. It can be appreciated that these clusters represent regions where radial fluctuations contribute to most of the TKE. The regions where observed clusters match the spatial position of mean Taylor vortices are seen in Figure 3.5c. Additionally, for the dominant mode(first mode), the radial fluctuation pattern shows an opposite sign in a pair of cells. However, It should be noted that the mode only shows the shape of spatial structures and the true direction of fluctuation is dependent on the sign of the temporal coefficient  $a^1(t)$  (Mohammadtabar *et al.* 2017). It can be concluded that the region of mean Taylor vortices (a counter-rotating pair is where radial fluctuation mainly contributes to TKE, however, the fluctuation direction in each vortex cell is opposite to the other in a statistical sense.

The first mode based on the axial velocity for water is shown in Figure 3.20a. It can be

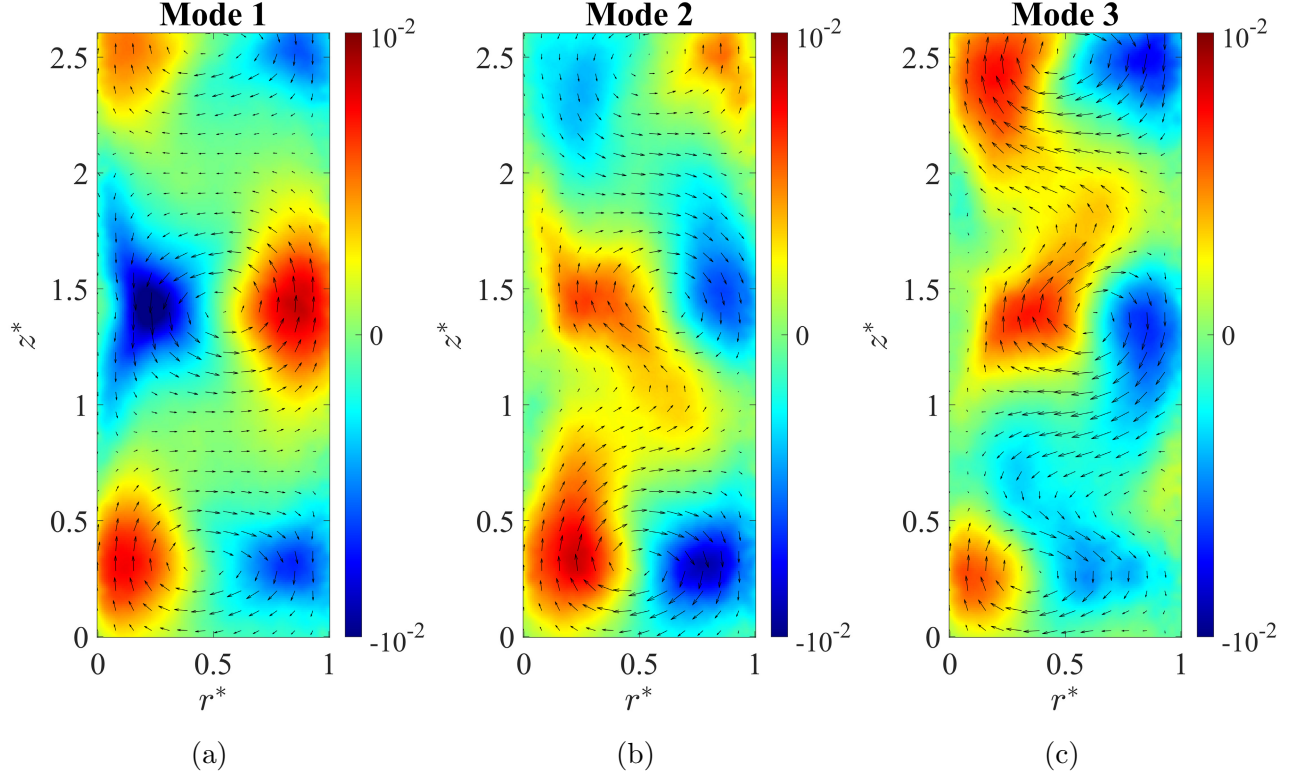


Figure 3.20: Plot of spatial modes of axial velocity fluctuation of water at  $\text{Re} = 1.5 \times 10^4$ . (a) mode 1. (b) mode 2. (c) mode 3. The vector shows  $\phi_j(\phi_{j,r}, \phi_{j,z})$  and background shows the value of  $\phi_{j,z}$ .

found that those highlighted regions are located close to the boundaries, and it can be appreciated that the first mode captures the convergence and separation motions of Taylor vortices at radial jets near the boundaries, which coincides with the axial velocity variance distribution discussed previously. The combination of the radial and axial fluctuation motions directly results in the formation of energetic vortex-shaped structures that are responsible for TKE, which eventually leads to the formation of turbulent Taylor vortices.

The second mode based on the radial velocity for water captures the dominant structures that are subjected to shear for Newtonian fluid. Figure 3.21 shows an example of the instantaneous radial velocity field and the POD reconstruction by just using the second spatial mode. It is apparent that the structures within the second mode were situated between the regions characterized by high radial velocity fluctuation magnitude. Notably, structures lying between velocity fluctuations of the same direction yield a positive radial eigenvector,

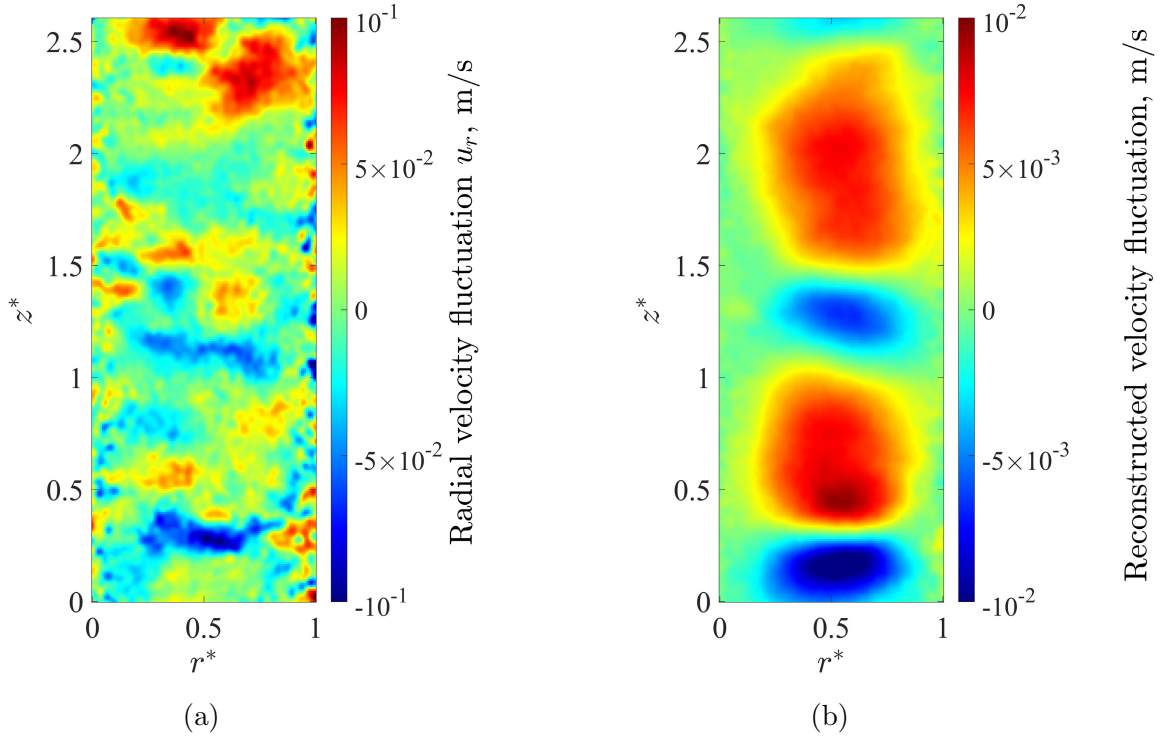


Figure 3.21: Plot of demonstration of the second mode structure. (a) An instantaneous radial velocity fluctuation (b) Reconstruction of the radial velocity component by using only the second mode.

while those between fluctuations of opposite directions result in a negative eigenvector value. Specifically, this structure is the jet between Taylor vortices in the present case. A relevant observation from Mohammadtabar *et al.* (2017), who proposed that the second mode of a wall-bounded channel flow bears resemblance to shear layer structures. These results further reinforce the significance of the second mode in capturing shear-related phenomena in Newtonian turbulent shear flows.

Figure 3.22 and 3.23 show the first 3 dominant modes for PAM-200 ppm solution at  $Re = 1.50 \times 10^4$  based on radial and axial velocity, respectively. The first mode still exhibits a pattern of vortical shape. It is striking to notice that the structures of axial motion in Figure 3.23 extend longer axially compared to water in both modes 1 and 2. This indicates a stronger axial variance of axial motion induced by the nonlinear viscosity effect. The convergence and separation motions can still be observed but are less intense compared to

the Newtonian case.

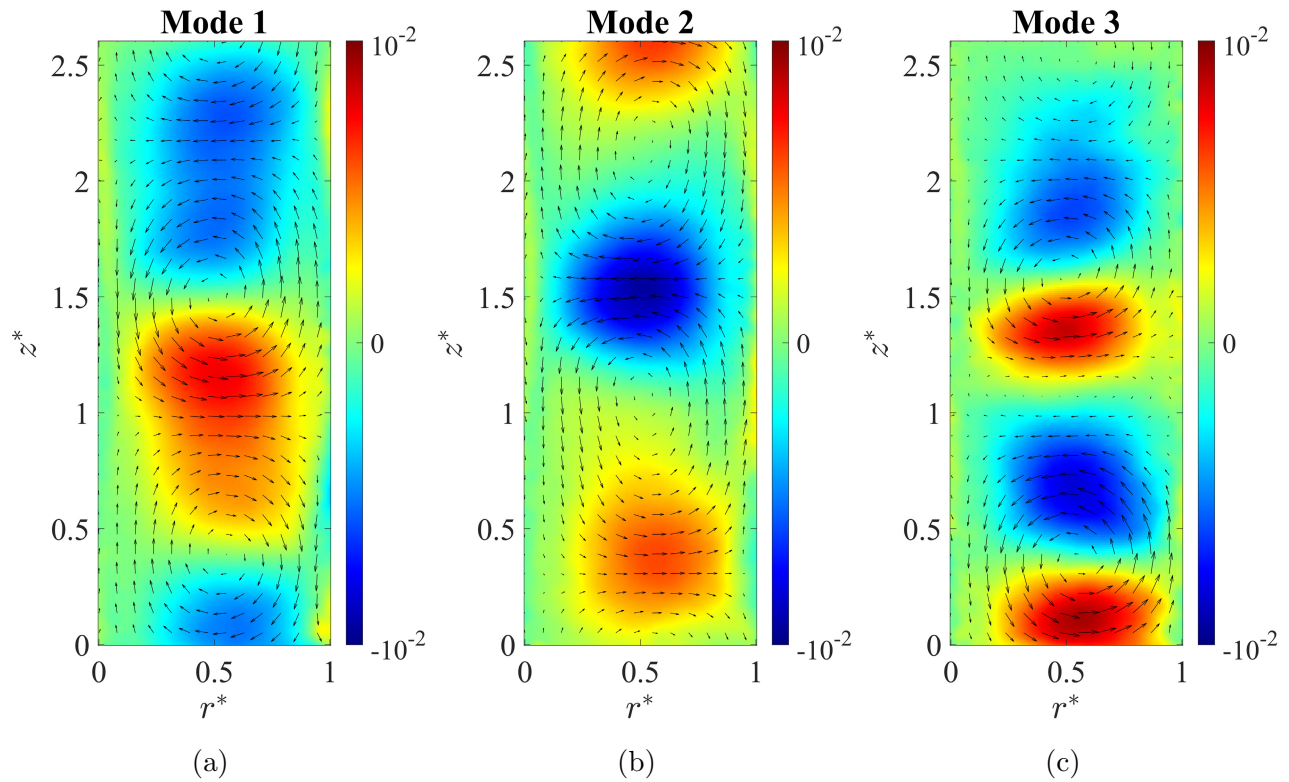


Figure 3.22: Plot of spatial modes of radial velocity fluctuation of PAM-200 ppm solution at  $\text{Re} = 1.50 \times 10^4$ . (a) mode 1. (b) mode 2. (c) mode 3. The vector shows  $\phi_j(\phi_{j,r}, \phi_{j,z})$  and background shows the value of  $\phi_{j,r}$ .

The first 3 dominant modes for PAM-400 ppm solution based on radial velocity and axial velocity fluctuation at  $\text{Re} = 1.50 \times 10^4$  are shown in Figure 3.24 and Figure 3.25. It can be observed that for the Newtonian solution in Figure 3.20, from mode 2 and onwards, the size of energetic structures of different signs are different. This is related to shear effect. However, for shear-thinning fluids, pronounced size change in the energetic structures starts from mode 3 as shown in Figure 3.24c. This could be appreciated as the decrease of importance of shear structures in the bulk in terms of TKE contributions. This coincides with the findings previously that the turbulent production is mitigated as the increase in the concentration of shear-thinning polymer.

Generally, the spatial modes of both Newtonian and non-Newtonian fluids exhibit a comparable distribution for the first mode, despite the nonlinear viscosity effects of non-

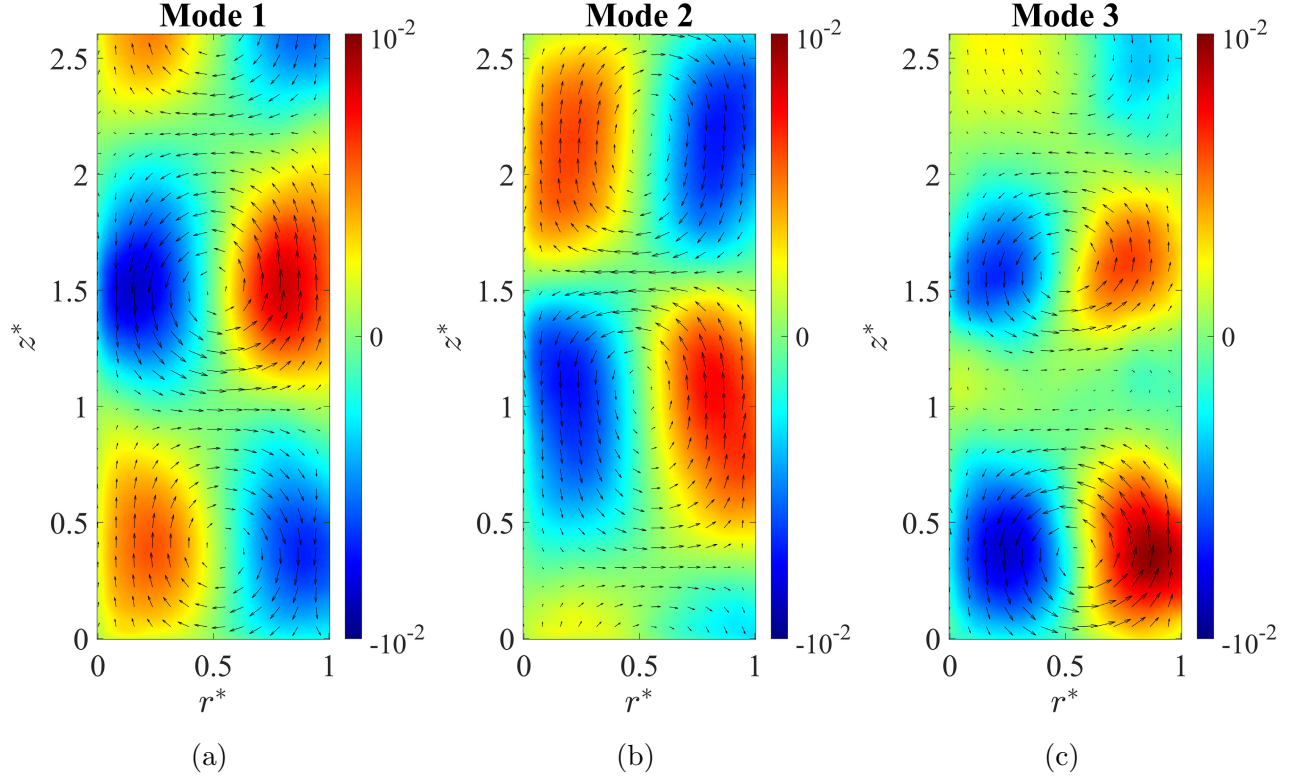


Figure 3.23: Plot of spatial modes of axial velocity fluctuation of PAM-200 ppm solution at  $\text{Re} = 1.50 \times 10^4$ . (a) mode 1. (b) mode 2. (c) mode 3. The vector shows  $\phi_j(\phi_{j,r}, \phi_{j,z})$  and background shows the value of  $\phi_{j,z}$ .

Newtonian fluids. Vortex-shaped structures are observed in the first mode for all cases. For the spatial modes based on radial velocity, both Newtonian and non-Newtonian fluids exhibit one column of vertical distribution of structures, with the number of structures increasing as the mode number rises.

The spatial modes associated with axial velocity mainly display two columns of structures aligned along the axial direction. For mode 1, the spacing between two neighboring structures vertically is the size of the coherent structures (Gul *et al.* 2018). It can be seen that the axial mode structures of non-Newtonian fluids are smoother compared to the Newtonian case. This can be attributed to shear-thinning fluid dampening the wall-normal and axial fluctuations near the wall.

Figure 3.26 illustrates the singular values  $\sigma_r$  and cumulative energy associated with the first  $r$  modes. In turbulent Taylor-Couette flow regimes for both Newtonian and non-

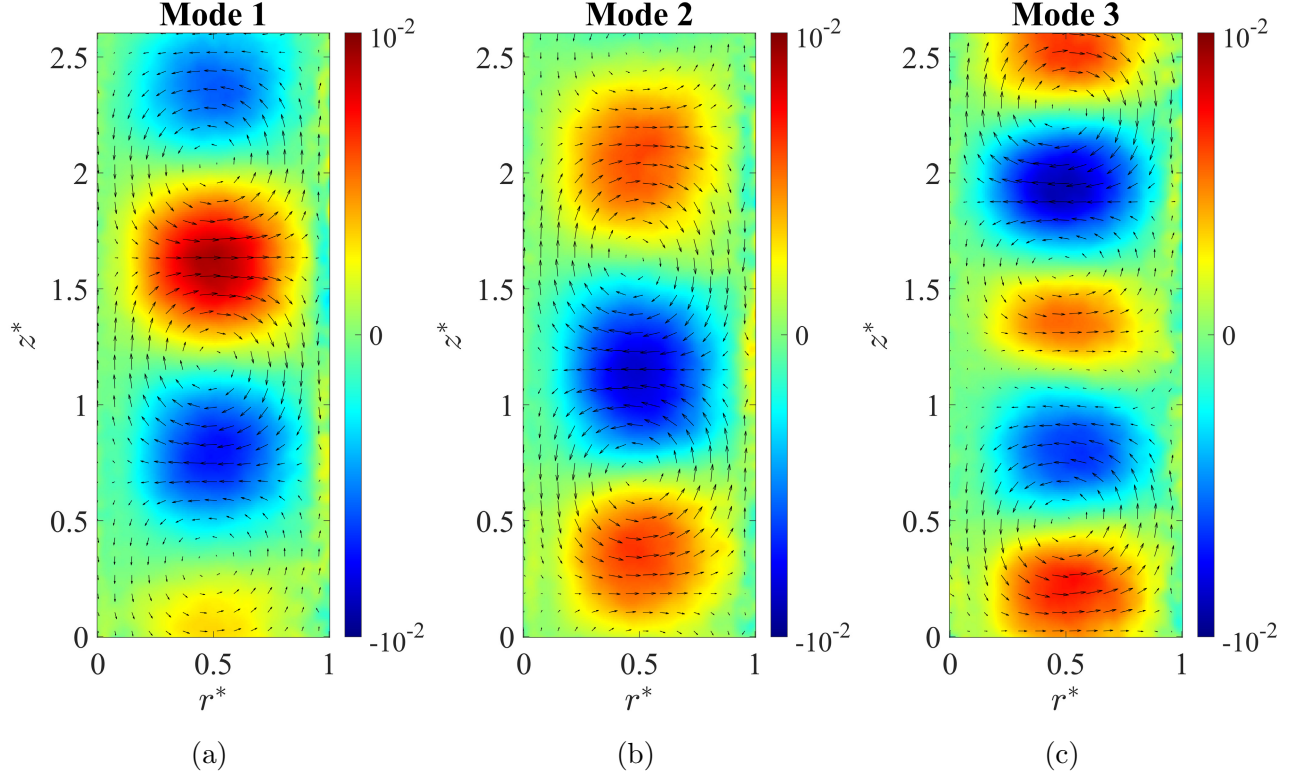


Figure 3.24: Plot of spatial of radial velocity fluctuation of PAM-400 ppm solution at  $Re = 1.50 \times 10^4$ . (a) mode 1. (b) mode 2. (c) mode 3. The vector shows  $\phi_j(\phi_{j,r}, \phi_{j,z})$  and background shows the value of  $\phi_{j,r}$ .

Newtonian fluids, it is observed that the mode of energy is relatively low for all cases. Specifically, the first mode contributes to less than 25% of the total TKE for all cases, as depicted in Figure 3.26b, and to reconstruct up to 75% of the total energy, 103 modes, 32 modes, and 122 modes are needed. This phenomenon of slow convergence of mode energy is attributed to the lower turbulence kinetic energy of secondary flows in comparison to the mean kinetic energy of secondary flow, with the majority of the energy residing in the mean flow (0 mode). It is also related to the range of lengthscales of turbulence. A large variety of scales usually leads to more modes to reach the same cumulative energy level.

The first few modes typically describe turbulent flow structures of large-scale energetic structures where shear is generated. The lengthscales of structures decrease as the mode number increases. Examination of Figure 3.26b reveals that PAM-200 ppm requires the fewest number of modes to describe large-scale structures. A possible reason that a local

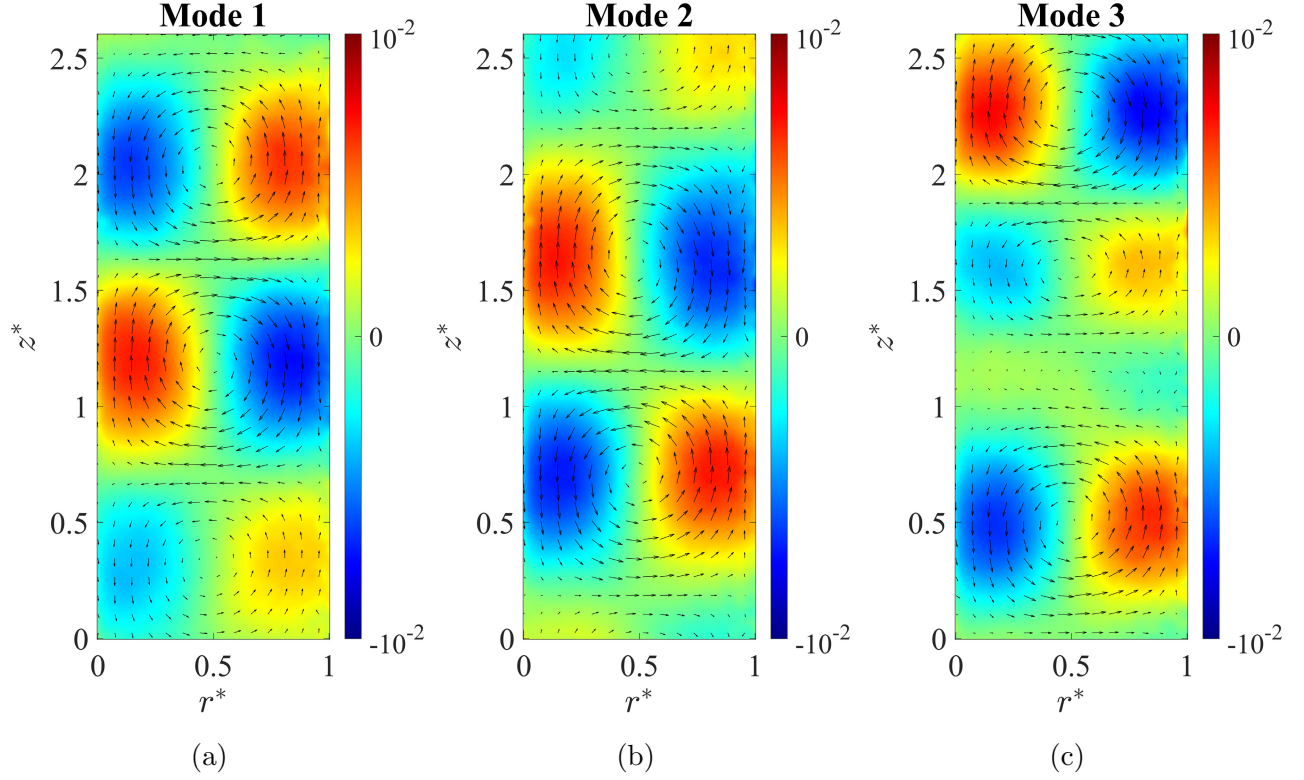


Figure 3.25: Plot of spatial modes of axial velocity fluctuation of PAM-400 ppm solution at  $\text{Re} = 1.50 \times 10^4$ . (a) mode 1. (b) mode 2. (c) mode 3. The vector shows  $\phi_j(\phi_{j,r}, \phi_{j,z})$  and background shows the value of  $\phi_{j,z}$ .

maximum of PAM additive occurs is that the axial motion of Taylor vortices at 200 ppm is important. The velocity fluctuation matrix  $\mathbf{D}$  which was provided into the POD algorithm represents turbulence fluctuation that the axial motions were not separated out, i.e, this part of motion was maintained within the data of fluctuation matrix. It can be seen that in Figure 3.23a and 3.23b, a longer axial velocity fluctuation pattern is observed for mode 1 and 2 compared to water and PAM-400 ppm which can be caused by the axial movement of Taylor vortices. Additionally, due to the shear-thinning effect, the small-scale fluctuation components are dampened, and TKE tends to be contributed by larger structures. PAM-200 ppm also contains a great proportion of large-scale structures over time. These combining effects lead to the fewest modes of TKE reconstruction for PAM-200 ppm.

For PAM-400 ppm, due to the stronger nonlinear viscosity effect, the secondary vortices tend to have a wider span of lengthscales which leads to a dispersion of total energy across

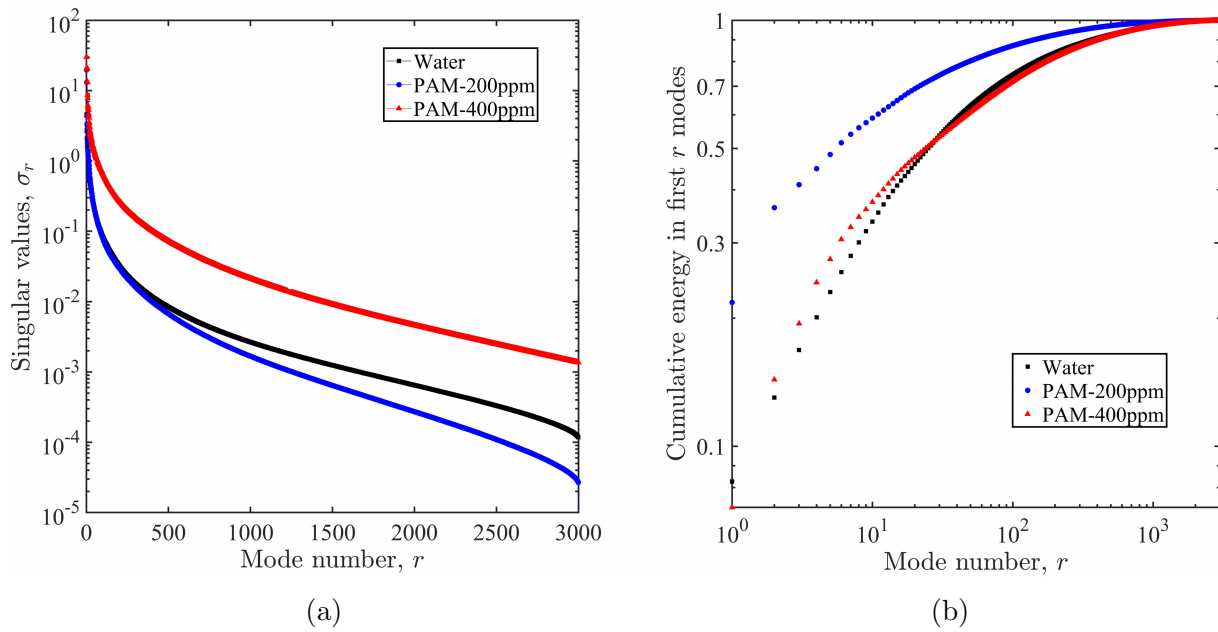


Figure 3.26: Plot of singular values and cumulative energy as a function of mode number. (a) Singular values  $\sigma_r$ . (b) Cumulative energy in first  $r$  modes.

all modes, and thus the most number of modes is needed to reconstruct the same level of TKE (Kostas *et al.* 2005).

### 3.9.2 Spatial Modes Based on Azimuthal Velocity

As discussed, the previous investigations were based on the in-plane velocity fluctuations, and the results of the first mode is relatively less distinctive between Newtonian and non-Newtonian solutions since vortex-shaped energetic structures remain the same for all cases. In this study, snapshot Proper Orthogonal Decomposition (POD) was implemented on the azimuthal fluctuation component. As previously mentioned, spatial modes are proven effective in capturing regions that contribute to TKE. It is also known that TKE is significantly influenced by regions subjected to shear or velocity gradients. Thus it can be hypothesized that the first few spatial modes can capture the most important shear flow structures, i.e., regions subjected to strong shear. For non-Newtonian fluid, regions that are subjected to strong shear should exhibit a pronounced shear-thinning effect (fluid viscosity becomes lower and moves actively). Thus it can be postulated that the region given by POD mode should be located mainly close to the wall where the shear rate is large.

For Newtonian fluid, Akonur and Lueptow (2003) showed that the azimuthal velocity in a wavy Taylor-Couette turbulence presents a jet-like velocity profile where at the outer/inner jet, the azimuthal velocity reaches the local maximum. Strong gradients were found adjacent to the jet and at both cylinder walls, thus these locations can be identified by POD modes in the Newtonian case. Figure 3.27 shows the first spatial mode of azimuthal velocity fluctuation for three fluids. In the case of water, as shown in Figure 3.27a, the highlighted areas are predominantly situated at near-wall regions and regions adjacent to the radial jet location as expected. A demarcation line in Figure 3.27a can be seen between the structures, indicating the position of the maximum mean azimuthal velocity in the inner jet. The structures show an increasing inclination angle with the outer wall as moving axially toward the inner cylinder and eventually becoming perpendicular to the wall. As the solution concentration increases to 200 ppm, the highlighted regions distribute against both the inner and outer cylinder walls. A striking feature of Figure 3.27b when compared with Figure 3.27a is that the inclination angle of the highlighted structures becomes smaller, and the structures tend to stay closer

to the wall, as would be expected due to the shear-thinning viscosity effect. Figure 3.27c for 400 ppm shows that the dominant regions are completely adjacent and parallel to the inner and outer cylinder walls. This means The distribution of the azimuthal Reynolds normal stresses is compressed towards the inner and outer wall where the shear is generated as the concentration increases. Overall the observation aligns with the understanding that the first POD mode of azimuthal velocity fluctuation effectively illustrates the regions where the shear effect is pronounced (i.e., where TKE is generated). For non-Newtonian fluid, regions where the shear-thinning effect is prominent are identified.

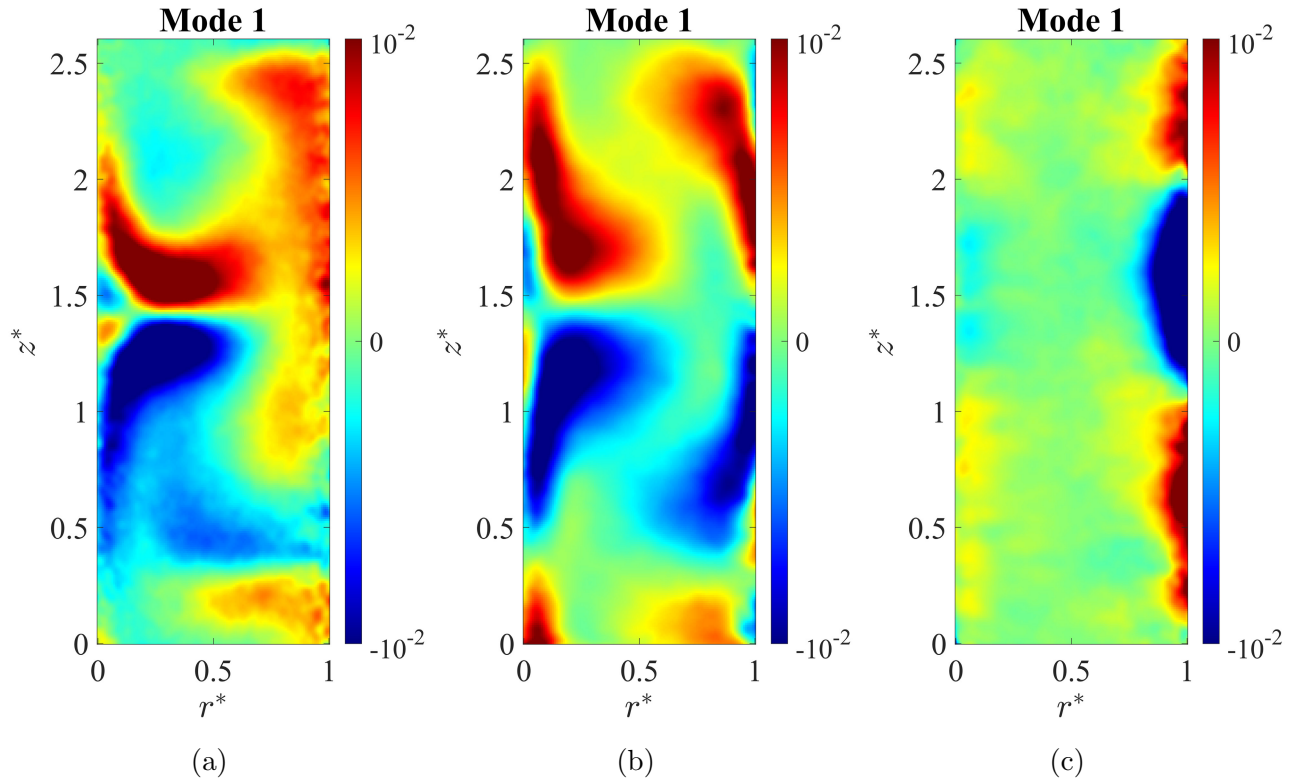


Figure 3.27: Plot of spatial mode 1 of azimuthal velocity fluctuation of different fluids at  $Re = 1.50 \times 10^4$ . (a) Water. (b) PAM-200 ppm. (c) PAM-400 ppm. The background shows the value of  $\phi_{j,\theta}$ .

### 3.10 Two-Point Correlation

Two-point correlation function provides a statistical measure of the relationship between two points within the turbulent flow field. This analysis helps understand the spatial coherence,

lengthscales of eddies, and interdependence of fluid properties at different positions. The two-point correlation function is given by Pope (2001) as shown in Equation 3.29 below:

$$R_{ij}(\mathbf{r}, t) = \langle u_i(\mathbf{x}, t)u_j(\mathbf{x} + \mathbf{r}, t) \rangle, \quad (3.29)$$

where  $\mathbf{r}$  represent the vector displacement between location of interest  $\mathbf{x}$  and  $\mathbf{x} + \mathbf{r}$ . Under the assumption of statistical stationarity:

$$R_{ij}(\mathbf{r}, t) = R_{ij}(\mathbf{r}). \quad (3.30)$$

$R_{ij}(\mathbf{r}, t)$  was normalized by the square root of variance at point  $\mathbf{x}$  and  $\mathbf{x} + \mathbf{r}$ , the normalized two-point correlation  $\tilde{R}_{ij}(\mathbf{r})$  is given by (Ghaemi and Scarano 2013):

$$\tilde{R}_{ij}(\mathbf{r}) = \frac{\langle u_i(\mathbf{x})u_j(\mathbf{x} + \mathbf{r}) \rangle}{\sqrt{\langle u_i^2(\mathbf{x}) \rangle \langle u_j^2(\mathbf{x} + \mathbf{r}) \rangle}}, \quad i, j = 1, 2, 3. \quad (3.31)$$

The two in-plane velocity fluctuation components  $u_r$  and  $u_z$  were used to obtain spatial correlation  $\tilde{R}_{11}$  and  $\tilde{R}_{33}$  to investigate the coherence of these fluctuations in  $r$  and  $z$  direction. Figure 3.28 to Figure 3.30 show the contours of  $\tilde{R}_{11}$ ,  $\tilde{R}_{13}$  and  $\tilde{R}_{33}$  for water, PAM-200 ppm and PAM-400 ppm respectively based on an example reference point at  $r^* = 0.5$  and  $z^* = 1.4$ . It can be seen that with the addition of polymer, the area of spatial correlation  $\tilde{R}_{11}$  and  $\tilde{R}_{13}$  are significantly increased compared to Newtonian solution. This finding aligns with previous Reynolds stress analyses, as shown in Figures 3.8 to 3.10, indicating that the addition of shear-thinning polymers tends to promote statistical homogeneity in T-C turbulent flows in the axial direction. The two-point correlation function quantifies the statistical relationship between two points in a flow field as a function of the distance between them. It can be postulated that the correlation between the two points separated by a certain distance in the axial direction would be higher compared to a less homogeneous flow. This is because in a homogeneous flow, there are no spatial gradients in any averaged quantity, meaning the statistics of the turbulent flow is not a function of space (Chen 2019). In contrast, in less

homogeneous flows, the presence of spatial gradients can introduce anisotropies, affecting the two-point correlations.

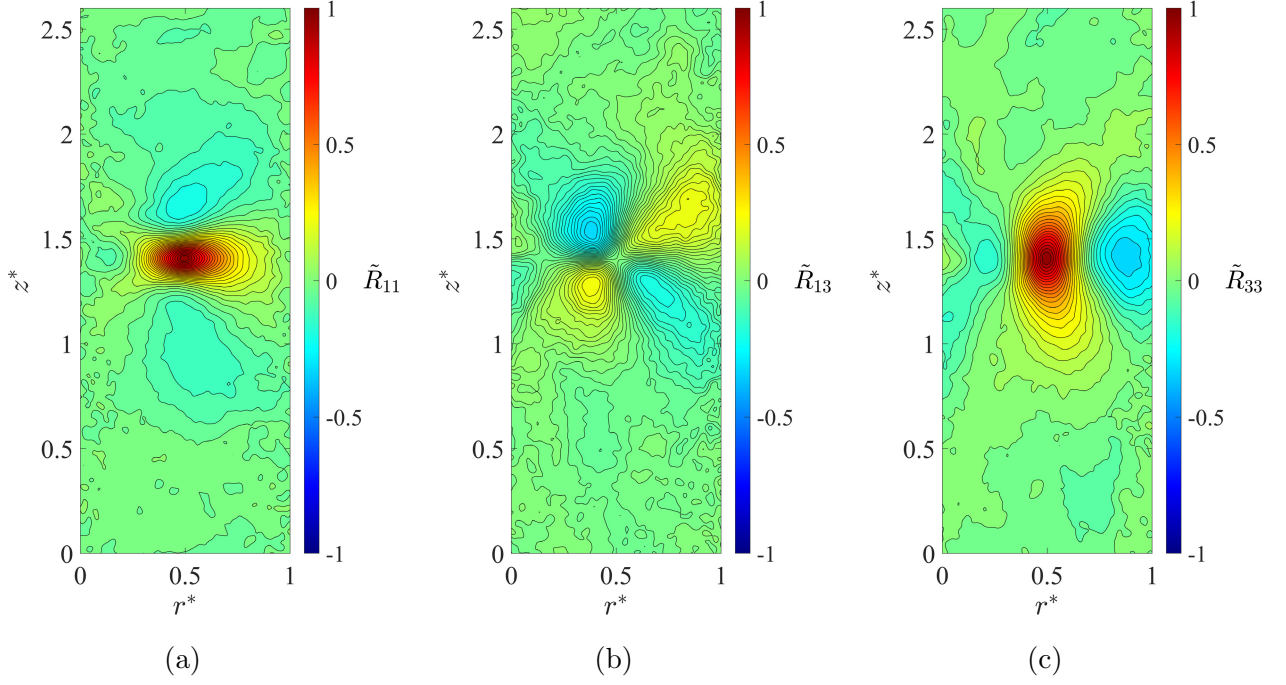


Figure 3.28: Plot of contours of two-point correlation of water based on an example reference point at  $r^* = 0.5$  and  $z^* = 1.4$ . (a) Contour of  $\tilde{R}_{11}$ . (b) Contour of  $\tilde{R}_{13}$ . (c) Contour of  $\tilde{R}_{33}$ .

Integral lengthscale in radial and axial directions were calculated. The integral lengthscale characterizes the range of motion in which coherent structures are significant in the turbulent flow.

The integral lengthscales in radial direction can be defined as (Pope 2001) :

$$L_{11}(x, t) = \frac{1}{R_{11}(0, x, t)} \int_0^\infty R_{11}(\mathbf{e}_1 r, x, t) dr. \quad (3.32)$$

$L_{11}$  can be expressed in terms of normalized two-point correlation  $\tilde{R}_{11}$ :

$$L_{11}(x, t) = \int_0^\infty \tilde{R}_{11}(\mathbf{e}_1 r, x, t) dr. \quad (3.33)$$

Similarly, the integral lengthscale in the axial direction can be defined as :

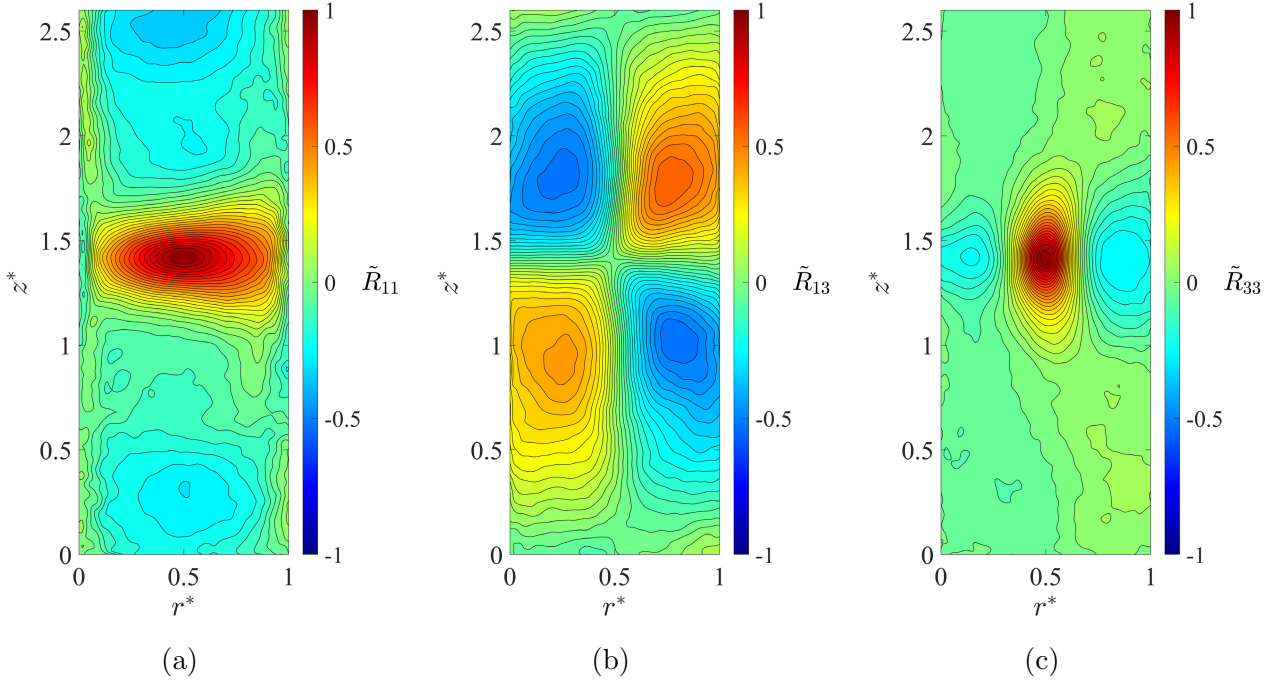


Figure 3.29: Plot of contours of two-point correlation of PAM-200 ppm based on an example reference point at  $r^* = 0.5$  and  $z^* = 1.4$ . (a) Contour of  $R_{11}$ . (b) Contour of  $R_{13}$ . (c) Contour of  $R_{33}$ .

$$L_{33}(x, t) = \int_0^\infty \tilde{R}_{33}(\mathbf{e}_3 r, x, t) dr. \quad (3.34)$$

Figure 3.31 shows the normalized two-point correlation  $\tilde{R}_{11}$  and  $\tilde{R}_{33}$ . The integral length-scale  $L_{11}$  and  $L_{33}$  refer to the area enclosed by the auto-correlation function curve with horizontal axis. As seen, under the same Re at the point in question, increasing the PAM concentration results in a greater  $L_{11}$  in radial direction, though this relationship is not strictly monotonic. Specifically, PAM-200 ppm exhibits the largest  $L_{11}$ . This coincides with the conclusion from POD analysis and the findings from vortex size distribution that at PAM-200 ppm concentration, a large proportion of large-scale structures still existed, and thus within the large structures the two-point correlation can still be strong. Figure 3.31b shows the distribution of lengthscale  $L_{33}$  in  $z$  direction, again based on the example reference point at  $r^* = 0.5$  and  $z^* = 1.4$ . From previous POD mode analysis of axial fluctuation mode as shown in Figure 3.19b, it can be postulated that if two-point correlation of radial fluctu-

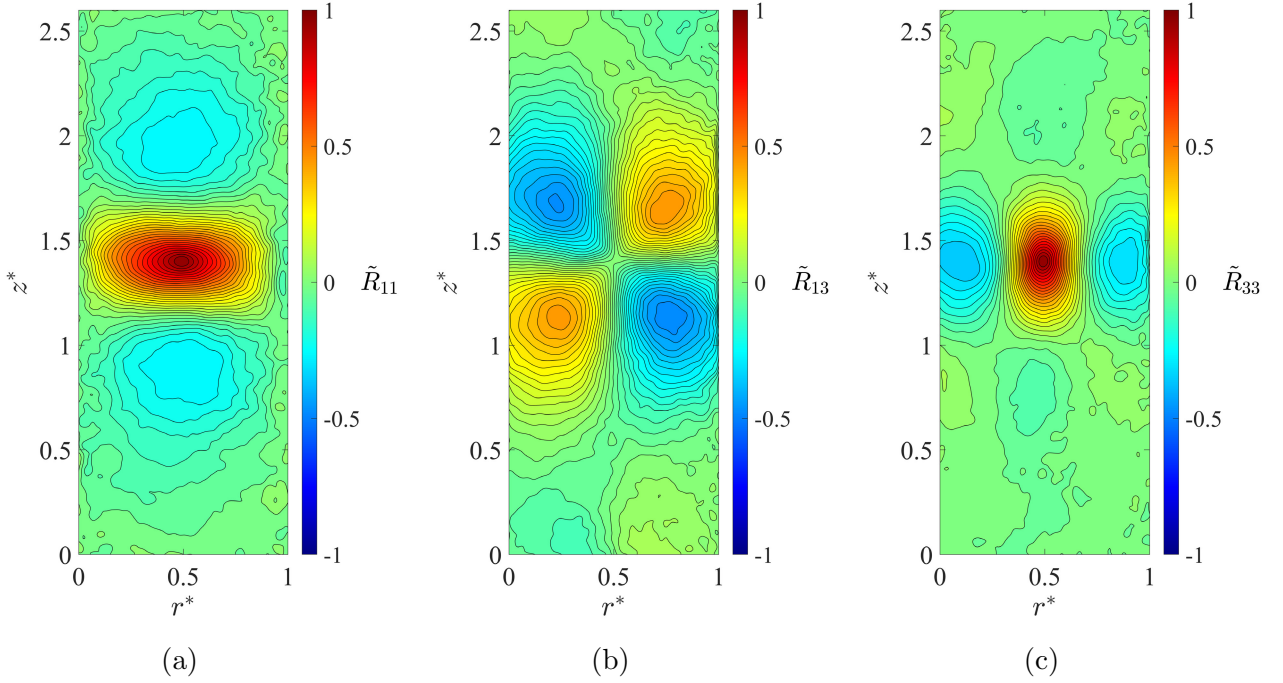


Figure 3.30: Plot of contours of two-point correlation of PAM-400 ppm based on an example reference point at  $r^* = 0.5$  and  $z^* = 1.4$ . (a) Contour of  $R_{11}$ . (b) Contour of  $R_{13}$ . (c) Contour of  $R_{33}$ .

ation were conducted between two neighboring vortices, the value of the correlation would likely be negative. Similarly, if two-point correlation of axial fluctuation were conducted between points at the jet locations close to the wall (e.g.,  $r^* = 0.2$ ,  $z^* = 0.4$  and  $z^* = 0.25$ ), the two-point correlation value would likely be negative. In the present study, the example reference point at  $r^* = 0.5$  and  $z^* = 1.4$  selected was an effort to avoid regions that show a clear correlation relationship caused by the influence of the wall.  $r^* = 0.5$  is very little affected by the wall which can be speculated in the first axial fluctuation POD modes for all the fluids, and it can show how the vortices are distributed in the axial direction.

A consistent decrease in  $L_{33}$  is found along the axial direction as the concentration increases. Interestingly, it is also noticed that for non-Newtonian fluids, a relatively pronounced negative two-point correlation  $\tilde{R}_{33}$  is observed whereas this is not found in Newtonian case. It is important to note that even with anti-correlation, it is still a correlation present, albeit negative. Anti-correlation reduces the integral lengthscale value, but it provides information

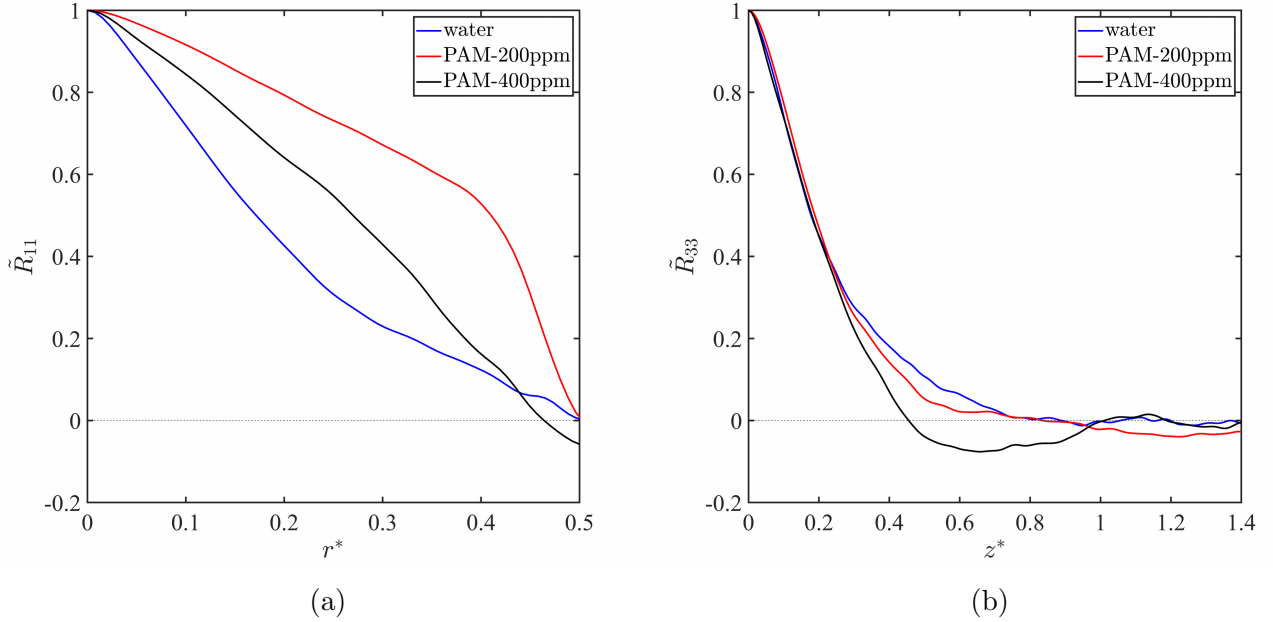


Figure 3.31: Plot of distribution of normalized two-point correlation in radial and axial direction at reference point  $r^* = 0.5, z^* = 1.4$ . (a)  $\tilde{R}_{11}$  distribution in  $r$  direction. (b)  $\tilde{R}_{33}$  distribution in  $z$  direction.

about the scale over which the correlation structure significantly affects the flow dynamics.

For Newtonian fluid, it is noticed that  $z^* = 0 - 1.4$  is a range that starts from the inner jet and extends slightly beyond one vortex cell length in the axial direction. For shear-thinning fluids at 400 ppm, due to the shear-thinning effect, the Taylor vortices tend to concentrate and compactly distribute within the FOV, and  $z^* = 0 - 1.4$  has covered a range that is much greater than the size of non-Newtonian Taylor vortex cell in the axial direction, i.e.,  $z^* = 0 - 1.4$  covers several vortices. Therefore, the sign of the two-point correlation statistics changes when transitioning from one vortex to another with an opposite rotation direction. It can be concluded that the negative two-point correlation  $\tilde{R}_{33}$  of PAM indicates the presence of compacted smaller-scale counter-rotating vortex pairs induced by the shear-thinning effect.

To better evaluate the non-linear viscosity effect on the lengthscale and isotropy of turbulence, a rectangular grid ( $3 \times 5$ ) of points was inspected in the flow field. The radial locations are  $r^* = 0.30, 0.50, 0.70$  and axial locations are  $z^* = 0.52, 0.96, 1.40, 1.84, 2.28$ . Integral lengthscale  $L_{11}$  and  $L_{33}$  were obtained for each point by trapezoidal integration.

The obtained lengthscales were averaged over the 15 points. The relative ratio of averaged lengthscale  $L_{33}/L_{11}$  for three fluids was investigated. For isotropic turbulence, the turbulent properties are the same in all directions, thus  $L_{33}/L_{11} = 1$ . The integral lengthscale  $L_{11}$  and  $L_{33}$  found for three solutions are listed in Table 3.3 below.

Table 3.3: List of integral lengthscales of  $L_{11}$  and  $L_{33}$  for three solutions.

	water	PAM-200 ppm	PAM-400 ppm
$L_{11}$	$0.20d$	$0.34d$	$0.26d$
$L_{33}$	$0.23d$	$0.21d$	$0.17d$

Figure 3.32 shows the relative ratio of  $L_{33}/L_{11}$  for three different fluids at  $Re = 1.50 \times 10^4$ . For water,  $L_{33}/L_{11} = 1.08$ , indicating that the integral lengthscale for water in  $r$  and  $z$  direction are close, and the flow state is close to isotropic flow. For PAM-200 ppm, a reduction in  $L_{33}/L_{11} = 0.60$  was observed, suggesting a strong anisotropic turbulent flow regime. This could be attributed to an extension of radial integral lengthscale whereas a reduction in axial lengthscale compared to water. For PAM-400 ppm,  $L_{33}/L_{11} = 0.76$ . By comparing to PAM-200 ppm in Table 3.3, it can be seen that both  $L_{11}$  and  $L_{33}$  are reduced, which could be attributed to the larger proportion of smaller sizes of the vortices. In general, it can be seen that in the turbulent Taylor vortex regime, with the addition of shear-thinning polymer, a larger radial integral lengthscale in the radial direction and a decreased integral lengthscale (extended space correlation due to anti-correlation) in the axial direction were found.

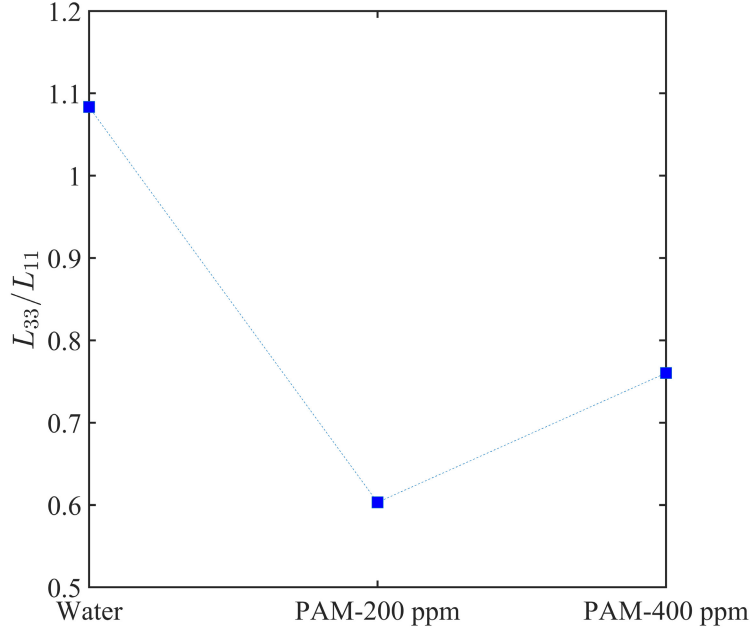


Figure 3.32: Plot of ratio of ratio of integral lengthscales  $L_{33}/L_{11}$  of water, PAM-200 ppm, and PAM-400 ppm.

### 3.11 Energy and Dissipation Spectrum

The turbulence kinetic energy (TKE) spectrum of in-plane velocity fluctuations based on the centre point of interest within the domain was investigated for the three fluids under the same Re. The energy spectrum shows the distributions of turbulence kinetic energy versus wavenumber. The initial step involves acquiring the velocity spectrum tensor, denoted as  $\Phi_{ij}(\boldsymbol{\kappa}, t)$ .  $\Phi_{ij}(\boldsymbol{\kappa}, t)$  is the Fourier transform of the two-point correlation (Pope 2001) :

$$\Phi_{ij}(\boldsymbol{\kappa}, t) = \frac{1}{(2\pi)^2} \iint_{-\infty}^{\infty} e^{-i\boldsymbol{\kappa}\cdot\mathbf{r}} R_{ij}(\mathbf{r}, t) d\mathbf{r}, \quad (3.35)$$

where  $\Phi_{ij}(\boldsymbol{\kappa}, t)$  represents the contribution to the covariance  $\langle u_i u_j \rangle$  of velocity modes with wavenumber  $\boldsymbol{\kappa}$ , and  $R_{ij}(\mathbf{r}, t)$  is the two-point correlation mentioned in Equation 3.29.

For a statistically stationary flow:

$$R_{ij}(\mathbf{r}, t) = \langle u_i(\mathbf{x}) u_j(\mathbf{x} + \mathbf{r}) \rangle. \quad (3.36)$$

The turbulence kinetic energy spectrum is shown as:

$$E(\kappa) \equiv \iint \frac{1}{2} \Phi_{ii}(\boldsymbol{\kappa}) \delta(|\boldsymbol{\kappa}| - \kappa) d\boldsymbol{\kappa}. \quad (3.37)$$

The vector length of  $\boldsymbol{\kappa}$  is calculated by the Euclidean norm of the radial and axial components:

$$\|\boldsymbol{\kappa}\| = \sqrt{\kappa_r^2 + \kappa_z^2}. \quad (3.38)$$

where  $\kappa_r$  represents the radial wavenumber, and  $\kappa_z$  represents the axial wavenumber. Given that the spatial resolution of cameras are equal in the  $r$  and  $z$  directions, the largest value of  $\kappa_r$  should be equal to that of  $\kappa_z$ . In practice, the value of the energy is calculated as:

$$E(\kappa) = \frac{1}{2} \sum_{i=1}^n \iint_{\kappa=|\boldsymbol{\kappa}|} \Phi_{i,i}(\boldsymbol{\kappa}) d\boldsymbol{\kappa}. \quad (3.39)$$

### 3.11.1 Energy Spectrum Based on Radial and Axial Velocity Fluctuation

In the present study, the characteristic lengthscale of the geometry  $l_0$  was selected as the gap width  $d$ , i.e.,  $l_0 = d = 19.1$  mm. The corresponding wavenumber is  $\kappa_0 = 2\pi/l_0 = 329.0 \text{ m}^{-1}$ . Based on Kolmogorov's first similarity hypothesis, a distinction is made between the energy-containing range and the inertial subrange. This is denoted by the characteristic lengthscale  $l_{EI}$ , and it was determined to be approximately 1/6 of the characteristic length scale of the geometry  $l_0$ , i.e.,  $l_{EI} = 1/6 l_0$  (Pope 2001). Here  $l_{EI} = 3.2 \times 10^{-3}$  m, and the corresponding wavenumber  $\lambda_{EI} = 2\pi/l_{EI} = 1963.5 \text{ m}^{-1}$ . The ensemble-averaged turbulence kinetic energy (TKE) spectrum was determined through the computation of the spectrum for each instantaneous velocity field. Subsequently, these individual spectra were averaged over time to obtain the ensemble-averaged TKE spectrum. To prevent aliasing, the Nyquist sampling criterion was ensured throughout the calculation process.

Figure 3.33 shows the energy spectrum based on in-plane velocity fluctuations for three solutions. Energy cascade was observed in the spectrum as wavenumber  $\kappa$  increases. Energy is transferred from larger scales to smaller scales through this process. This process holds true for both Newtonian and non-Newtonian fluids, that the majority of turbulence kinetic energy (TKE) resides within the energy-containing range. All the profiles within the inertial subrange do not follow the Kolmogorov scaling law with slope of  $-5/3$ . Interestingly, in Taylor-Couette turbulence, no scaling law was observed in frequency spectral density (Huisman *et al.* 2013a; Lewis and Swinney 1999). This aligns with the understanding that Taylor-Couette flow is inherently anisotropic, with the presence of a mean shear flow between the inner and outer cylinders. This anisotropy can lead to deviations from the isotropic assumptions made in the Kolmogorov theory. Additionally, in Taylor-Couette turbulence, large-scale coherent structures in T-C turbulence can influence the energy cascade and the scaling of the energy spectrum at the inertial subrange.

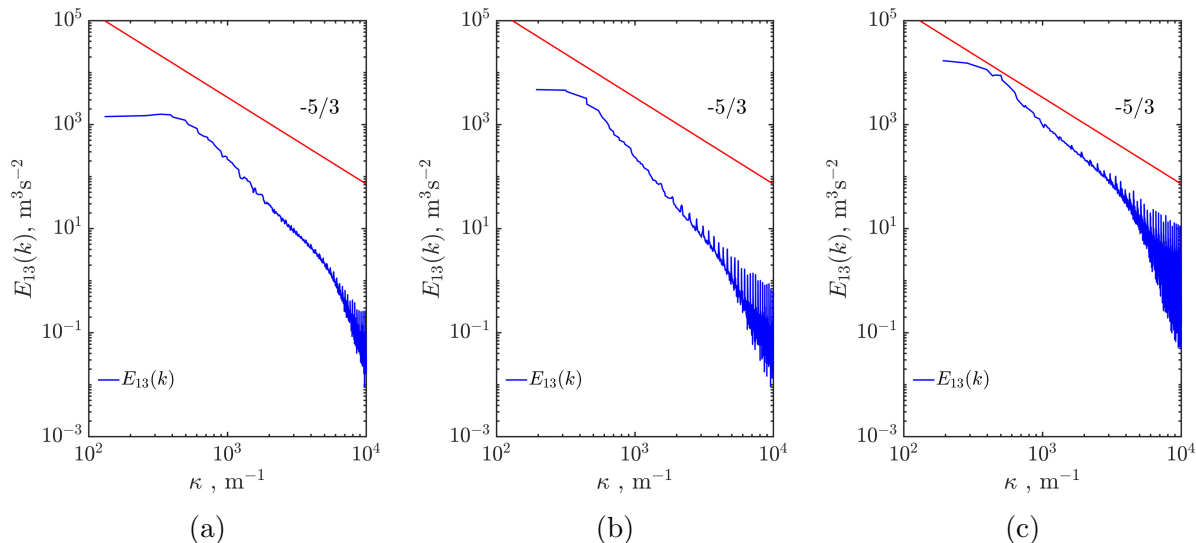


Figure 3.33: Plot of turbulence kinetic energy spectrum over wavenumber with solutions under  $Re = 1.50 \times 10^4$ . (a) Water. (b) PAM-200 ppm. (c) PAM-400 ppm.

The ensemble-averaged energy spectrum of water at  $Re = 1.50 \times 10^4$  is shown in Figure 3.33. A plateau-like behavior was observed in the energy-containing range, however, this is not observed for non-Newtonian cases in Figure 3.33b and 3.33c. As seen, the flat segment

of the plateau reduced as increasing the concentration of polymers. This indicates that in Newtonian T-C turbulence, there exist large-scale structures with a relatively wide span of lengthscales that contribute to the same TKE level. The presence of PAM implies that the polymer changes the turbulent cascade process by facilitating the energy transfer at large-scale structures within the energy-containing range.

For non-Newtonian solutions, an increase in concentration results in higher TKE at small lengthscales, accompanied by more pronounced oscillations compared to the Newtonian case. This behavior is likely attributed to the transition into the dissipative range as approaching the smallest scales in the turbulence spectrum, where the effects of viscosity become dominant. In this range, energy is dissipated as heat, and the fluctuations are influenced by the molecular viscosity of the fluid which leads to intense and oscillatory fluctuations associated with dissipative processes.

### 3.11.2 Energy Spectrum Based on Radial and Azimuthal Fluctuation

Radial and azimuthal velocity fluctuations are of interest since the contribution to the production of turbulence. The spectral density function based on radial and azimuthal velocity fluctuation is denoted by  $E_{12}(k)$ , with unit of  $\text{m}^3\text{s}^{-2}$ . The energy spectrum was normalized by the total sum of  $k^{-1} \langle u_r^2(r, z) \rangle_N^{-1/2} \langle u_\theta^2(r, z) \rangle_N^{-1/2}$  in FOV, where  $\langle u_r^2(r, z) \rangle_N^{-1/2} \langle u_\theta^2(r, z) \rangle_N^{-1/2}$  is the product of the root mean square of the two velocity fluctuations. The obtained quantity is denoted by  $k\tilde{E}_{12}(k)$ , which is dimensionless. The normalized spectral density function was plotted for three fluids as shown in Figure 3.34. It shows that the addition of shear-thinning polymer concentration increases the importance of large-scale structures and decreases the importance of small-scale structures in terms of energy containment.

### 3.11.3 Dissipation Spectrum

For Newtonian fluid, the dissipation density function  $D(k)$  can be calculated as  $D(k) = 2\nu\kappa^2 E(k)$ . It is worth mentioning that the dissipation term was originally derived from

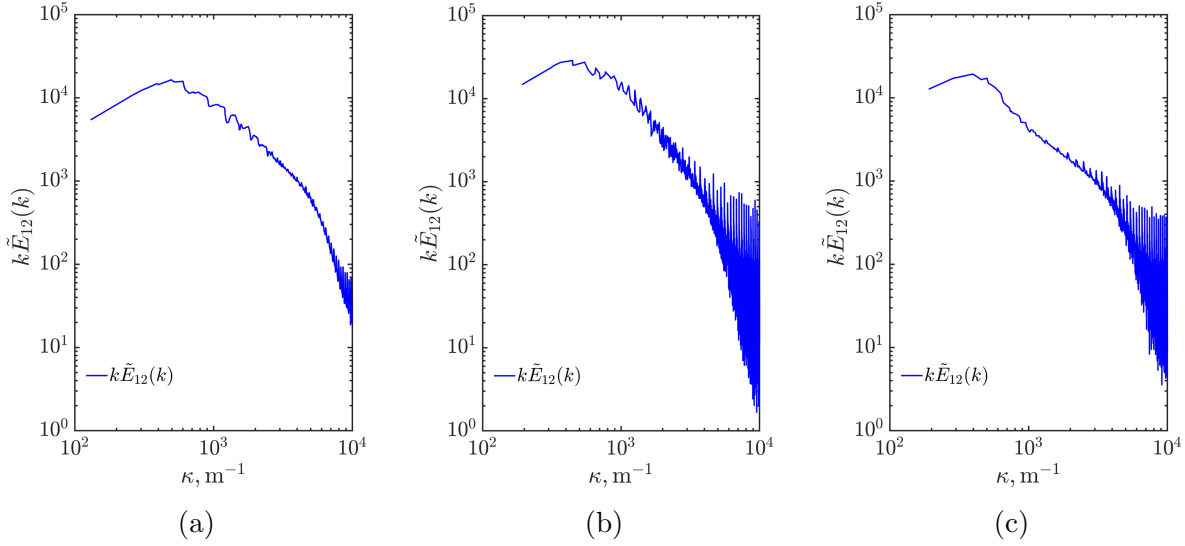


Figure 3.34: Plot of normalized energy spectrum based on radial and azimuthal fluctuation over wavenumber with three solutions under  $Re = 1.50 \times 10^4$ . (a) Water. (b) PAM-200 ppm. (c) PAM-400 ppm.

the Newtonian turbulent kinetic energy equation (Pope 2001). However, for non-Newtonian fluid, there is no expression available for the dissipation term due to a lack of knowledge in non-Newtonian viscosity modeling. Singh *et al.* (2017) investigated the influence of the shear-thinning effect in pipe turbulence, where the power-law model was implemented for viscosity modeling, and it was found that an additional term of dissipation arises from viscosity fluctuations which eventually result in a net viscous dissipation. The present study calculated the dissipation spectrum for non-Newtonian fluid based on the same concept as the Newtonian fluid for simplicity.

Figure 3.35 illustrates the in-plane dissipation spectrum of three solutions. As seen, the dissipation per wavenumber increases across all length scales as the concentration of polymer increases. This increase can be attributed to the acceleration of rotation speed with increasing polymer concentration, necessitating a corresponding increase in dissipation to balance the increased production.

Furthermore, a slower reduction of dissipation rate after the peak is observed as the concentration increases, indicating a more pronounced dissipation at smaller lengthscales. The

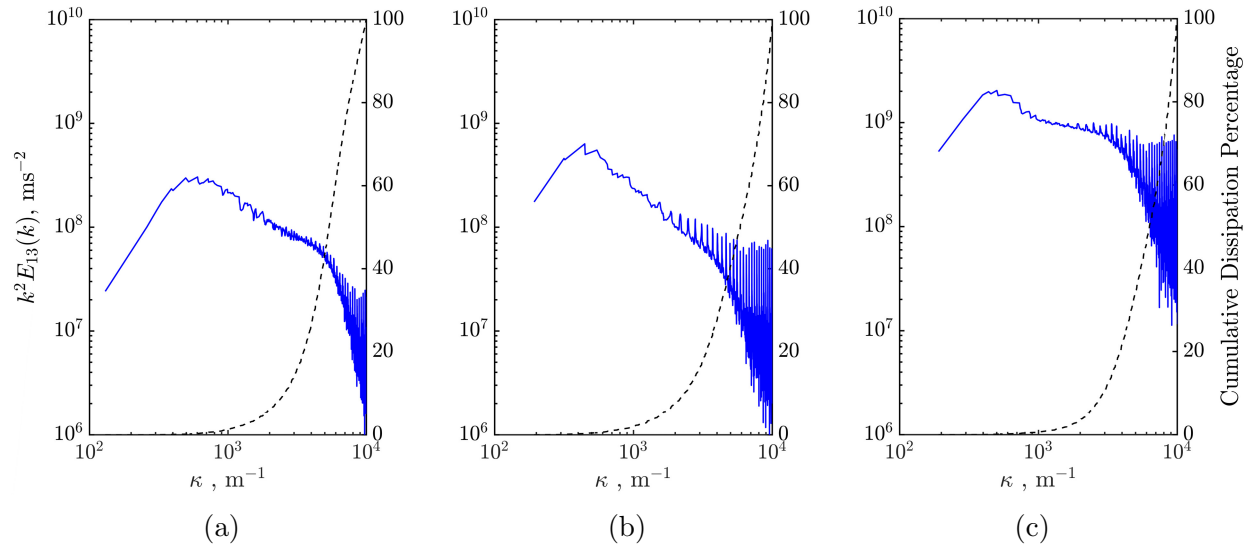


Figure 3.35: Plot of turbulent dissipation spectrum  $k^2 E_{13}(k)$  over wavenumber with solutions under  $\text{Re} = 1.50 \times 10^4$ . (a) Water. (b) PAM-200 ppm. (c) PAM-400ppm. The dashed line shows the cumulative dissipation percentage over the wavenumber.

cumulative dissipation analysis reveals that as the polymer concentration increases, smaller-scale eddies contribute more to dissipation, while dissipation by larger eddies decreases.

# Chapter 4

## Discussion

Statistical measurements of non-Newtonian shear-thinning turbulent Taylor-Couette flows are characterized by a sharper shear rate compacted closer to the inner cylinder regions due to the shear-thinning effect, with less active fluids occupying the bulk domain. The resulting change of secondary flow structure distributions and turbulence statistics has been investigated under the same nominal Reynolds number at  $Re = 1.50 \times 10^4$  and Newtonian fluid as comparison.

Newtonian fluid of turbulent Taylor-Couette flow at  $Re = 1.50 \times 10^4$  still shows the existence of large-scale Taylor vortices. A pair of counter-rotating turbulent Taylor vortices are captured, with a relatively high-speed radial jet flow between them. The regions adjacent to the jet show large magnitude of variance of radial velocity  $\langle u_r^2 \rangle_N / U_{ref}^2$  whereas regions near the vortex centres show a small magnitude of  $\langle u_r^2 \rangle_N / U_{ref}^2$ . For Reynolds shear stress  $\langle u_r u_\theta \rangle_N$ , a non-uniform distribution is observed along the axial direction as well, which is attributed to the non-homogeneous distribution of velocity gradient in space. The varying magnitudes of Reynolds stresses across space result in non-statistically homogeneous turbulent flows. Newtonian Taylor vortices are found relatively stationary in space, which is attributed to the finite apparatus length. Within the finite length, Taylor rolls are arranged next to each other along the axial direction, and as a result, the Taylor rolls are locked because of the end boundary conditions.

Non-newtonian fluids show structural differences compared to the Newtonian fluid. Ob-

servations of instantaneous in-plane velocity structures show the existence of non-Newtonian vortices. The vortices are moving more freely compared to the Newtonian case and exhibit stronger vortex deformation. The reason is that due to the shear-thinning effect, the Taylor vortices do not sense much constraints from the wall compared to the Newtonian case. The T-C instability from the inner cylinder wall which is responsible for the Taylor vortices generation has to go through areas where viscosity gradually increases before reaching the outer wall in non-Newtonian case. The region in the bulk where viscosity gradually increases serves as a buffer zone where turbulence kinetic energy carried by high-momentum fluids is absorbed. Statistical analysis shows that both radial and axial velocity fluctuations are attenuated in the bulk flow and result in a decreased magnitude of Reynolds normal (variances of radial and axial velocity) and shear stresses (covariance of radial and azimuthal velocity). It is also noticed that the stresses are smeared out across the domain and tend to be more uniformly distributed in the axial direction. As the concentration increases to 400 ppm, variances of radial velocity  $\langle u_r^2 \rangle_N / U_{ref}^2$  and axial velocity  $\langle u_z^2 \rangle_N / U_{ref}^2$  are further decreased and show a statistically homogeneous turbulence in the axial direction, which can be considered as an indicator of minimal wall influence from the top and bottom boundary conditions.

Similarly, the radial jet (both inner and outer jets) intensity is reduced with the addition of shear-thinning polymer. The radial jets that carry fluids with high-momentum kinetic energy get attenuated at a higher rate as moving to the other side of the cylinder wall due to the shear-thinning effect. The Taylor vortex cell is formed between a pair of jets that shoot in opposite radial directions. The reduced intensity of radial jets leads to a decreased partition effect of the jet for separating vortices, which enables non-Newtonian vortices to move with higher freedom in the axial direction. The reduced jet intensity also causes a reduction of shear, which eventually causes a decreased magnitude of ensemble-averaged azimuthal vorticity compared to the Newtonian case.

Interesting observations are made in the energetic structures of POD analysis. It has been found that the mean flow of Taylor-vortex structures ('0' mode of POD) are the energetic structures that contribute to the kinetic energy. Here the energetic structures responsible

for TKE are discussed for Newtonian and non-Newtonian cases. It was found that despite the differences in turbulent structures as discussed, the dominant in-plane energetic mode structures that statistically contribute to TKE remain a vortical shape for both Newtonian and non-Newtonian fluids. For water, the dominant energetic structure shows a  $\pi/2$  phase lag in space compared to the mean flow ('0' mode). The radial velocity fluctuation responsible for TKE is mainly captured within Taylor vortices and the axial fluctuation responsible for TKE is mainly captured close to the wall, where the boundary of the vortices merge and separate. The second mode of water based on radial fluctuation emphasizes the importance of the shear-layer structures. The second mode of non-Newtonian fluids shows distinctive energetic structures in size, which means the non-Newtonian fluids alter the shear distribution in space.

In T-C turbulent flows, the variance of the azimuthal (streamwise) direction is the strongest among all three directions. POD was applied over azimuthal velocity fluctuation to capture most of the variances of azimuthal velocity. For Newtonian fluid, the energetic mode structures are distributed close to both cylinder walls and adjacent to the jets. This means the majority of Reynolds normal stress  $\langle u_\theta^2 \rangle_N$  as a part of TKE is mainly generated close to the wall and radial jets. The energetic structures are pronounced at the center of the bulk flow which indicates the non-negligible importance of the bulk flow in the middle. With the addition of shear-thinning polymer to 200 ppm, the energetic structures start to deviate from the bulk flow and gradually approach closer to the cylinder walls. This indicates a decreased importance of the bulk flow in terms of contributing the Reynolds stress  $\langle u_\theta^2 \rangle_N$ . This aligns with the previous finding that the radial jet intensity is reduced, and thus less high momentum fluids can carry the high momentum flux  $\langle u_\theta^2 \rangle_N$  to the middle. Under this concentration, the energetic structure that contributes to  $\langle u_\theta^2 \rangle_N$  mostly at regions where the azimuthal shear is strong, i.e., close to the cylinder walls. As concentration increases further, all the energetic structures by POD captured are compacted against the wall where a high shear rate exists, whereas the bulk flow does not contain any energetic structures, which indicates the fluctuation of the bulk flow is almost negligible in terms of contributing to

TKE. This aligns with the heuristic understanding of shear-thinning effects in turbulence.

With the addition of shear-thinning polymer, the turbulence fluctuations in the radial and axial directions are dampened, and turbulence statistics of the secondary flow tend towards a more statistically homogeneous state in the axial direction. These effects induced by the shear-thinning fluid lead to an extended two-point correlation in the axial direction. Two-point correlation was conducted over a line starting from a selected reference point to the bottom of the FOV, which travels through a distance roughly equal to the size of a Newtonian Taylor vortex. Thus for Newtonian fluid, the two-point correlation mostly remains positive till dropping to around zero. For shear-thinning fluids, due to the shear-thinning effect, vortices are compressed to a small volume and coexist, and the length of the line is large enough to cover more than one vortex, which leads to a relatively pronounced anti-correlation. Due to the anti-correlation, the resulting integral lengthscale  $L_{33}$  decreases for shear-thinning fluids compared to the Newtonian case.

Observations have been made in this study that in the Newtonian turbulent Taylor-Couette flow at  $Re = 1.50 \times 10^4$ , the large structures of Taylor vortices still exist, which indicates a spatial non-homogeneous turbulence. The energy spectrum of Newtonian fluid shows that the  $-5/3$  Kolmogorov law is not applicable, which is valid under the assumption of homogeneous isotropic turbulence. The non-Newtonian energy spectra for PAM 200 ppm and 400 ppm are found not to follow the Kolmogorov  $-5/3$  scaling law either.

For all turbulence, it is universal that turbulence dissipation occurs mostly at small length-scales (high wavenumbers). For non-Newtonian fluid, the viscous effect is pronounced, and turbulence might dissipate at high wavenumber at a higher rate compared to Newtonian fluids, The shape of the dissipation spectrum for non-Newtonian fluid at 400 ppm shows that small lengthscales of turbulence might be more responsible for turbulence dissipation compared to Newtonian fluids.

# Chapter 5

## Conclusion

The experimental investigations of turbulent Taylor-Couette (TTC) flow structures were conducted for non-Newtonian and Newtonian fluid at  $Re = 1.50 \times 10^4$  by using SPIV technique.

Results show that under the same  $Re$ , the skin coefficient  $C_{f,l}$  reduces as the concentration increases. This is attributed to the reduction of Reynolds shear stresses at the inner cylinder wall induced by the drag-reducing polymers.

The shear-thinning polymer Polyacrylamide reduces the radial ( $r$ ) and axial ( $z$ ) velocity fluctuation in the bulk flow, which results in a decreased magnitude of Reynolds normal (variances of radial and axial velocity) and shear stresses (covariance of radial and azimuthal velocity).

In shear-thinning T-C turbulence, Reynolds stresses are smeared out across the domain as the concentration increases, and a statistically homogeneous turbulence state in the axial direction can be achieved, however, turbulence statistics in the radial direction are not homogeneously distributed due to the mean shear gradient.

The locations of Newtonian Taylor vortices are relatively fixed due to the finite length of the apparatus and the end boundary conditions, whereas non-Newtonian Taylor vortices have more flexibility of motion both in the axial and radial direction, which is induced by the shear-thinning effect.

The in-plane turbulent structures that statistically contribute to most of the TKE remain

a vortical shape for both Newtonian and non-Newtonian fluids. The second mode of POD captures the shear layer structures in the Newtonian case, but due to the modification of shear distribution in the flow by shear-thinning polymers, the second mode of Newtonian and non-Newtonian show distinct energetic mode structures.

The energetic structures of azimuthal velocity captured by POD are found closely related to the shear and velocity gradient in space. The first mode of POD of azimuthal velocity fluctuation effectively captures the regions where the shear effect is pronounced. As the concentration of polymer increases, the regions subject to shear are more compacted to the inner and outer cylinder walls due to the shear-thinning effect, and POD mode can capture this shear-thinning behavior.

The presence of shear-thinning polymer alters both the integral lengthscale and isotropy of Taylor-Couette turbulence. A non-monotonic behavior of the integral lengthscale  $L_{11}$  in the radial direction was observed, alongside a consistent reduction of the axial integral lengthscale  $L_{33}$  as the concentration increases. The reduction of the integral lengthscale  $L_{33}$  of non-Newtonian fluid is attributed to the anti-correlation in space. Non-Newtonian fluids show relatively pronounced anti-correlation in the axial direction due to the more compacted distribution and coexistence of more than one vortex axially within the inspected FOV induced by the shear-thinning effect. The shear-thinning effect leads to a more statistically homogeneous turbulence and thus enhances the two-point correlation compared to the Newtonian fluid.

The 2D energy spectrum reveals that the Kolmogorov  $-5/3$  law does not hold for Taylor-Couette turbulence, primarily due to its inherent anisotropy. A notable disparity between Newtonian and non-Newtonian fluids is evident in the energy spectrum based on radial and azimuthal fluctuations, which shows an increased importance of large-scale structures and a decreased importance of motions at small lengthscales in terms of energy containment. Analysis of the dissipation spectrum indicates that the percentage of dissipation rate at smaller lengthscales increases with the concentration of polymer.

# Chapter 6

## Future Work

In recent decades, efforts have been devoted to understanding the shear-thinning effect on turbulent structures in wall-bounded flows. However, due to the complexity of non-Newtonian physics, turbulent modeling of non-Newtonian fluids remains extremely challenging. There is an urgent need for the development of accurate and reliable constitutive models capable of describing the rheological behavior of non-Newtonian fluids in turbulent flows.

Experimentally, the curved surfaces of Taylor-Couette rigs have posed considerable challenges, leading to compounding measurement errors, especially near the wall. Therefore, careful evaluation is essential in the design of experimental flow rigs and velocimetry measurements. A future experimental study focusing on near-wall turbulent structures of shear-thinning fluids with high accuracy is desired with fine spatial resolution, aiming to elucidate the turbulence kinetic energy budget near the wall for shear-thinning cases.

Low concentrations of shear-thinning polymeric flows have been extensively investigated, whereas high concentrations of shear-thinning fluid in Taylor-Couette flows remain relatively unexplored in terms of structures and turbulent statistics. The high concentration of shear-thinning polymers presents additional challenges in Taylor-Couette flows, including seeding, velocimetry measurement, and optical access. It can be postulated that in high-concentration shear-thinning Taylor-Couette flows, the turbulent Reynolds shear stresses will be greatly dampened, and the in-plane motions will be further mitigated, leading to higher uncertainties for 3D velocity reconstruction. These challenges are hoped to be addressed in future research

efforts to bridge this gap.

# Bibliography

- [1] A. Abdel-Alim and A. Hamielec, “Shear degradation of water-soluble polymers. i. degradation of polyacrylamide in a high-shear couette viscometer,” *Journal of Applied Polymer Science*, vol. 17, no. 12, pp. 3769–3778, 1973.
- [2] R. J. Adrian and J. Westerweel, *Particle image velocimetry*, 30. Cambridge university press, 2011.
- [3] M. Afshari, D. J. Sikkema, K. Lee, and M. Bogle, “High performance fibers based on rigid and flexible polymers,” *Polymer Reviews*, vol. 48, no. 2, pp. 230–274, 2008.
- [4] Y Agbessi, B Alibenyahia, C. Nouar, C Lemaitre, and L Choplin, “Linear stability of taylor–couette flow of shear-thinning fluids: Modal and non-modal approaches,” *Journal of Fluid Mechanics*, vol. 776, pp. 354–389, 2015.
- [5] A. Akonur and R. M. Lueptow, “Three-dimensional velocity field for wavy taylor–couette flow,” *Physics of Fluids*, vol. 15, no. 4, pp. 947–960, 2003.
- [6] C Al Christopher, Í. G. da Silva, K. D. Pangilinan, Q. Chen, E. B. Caldona, and R. C. Advincula, “High performance polymers for oil and gas applications,” *Reactive and Functional Polymers*, vol. 162, p. 104878, 2021.
- [7] A. A. Aliabadi, “Statistical description of turbulent flows,” in *Turbulence: A Fundamental Approach for Scientists and Engineers*, Springer, 2022, pp. 17–30.
- [8] B. Alibenyahia, C. Lemaitre, C. Nouar, and N. Ait-Messaoudene, “Revisiting the stability of circular couette flow of shear-thinning fluids,” *Journal of Non-Newtonian Fluid Mechanics*, vol. 183, pp. 37–51, 2012.
- [9] C. D. Andereck, S. Liu, and H. L. Swinney, “Flow regimes in a circular couette system with independently rotating cylinders,” *Journal of Fluid Mechanics*, vol. 164, pp. 155–183, 1986.
- [10] N. Annabi *et al.*, “Hydrogel-coated microfluidic channels for cardiomyocyte culture,” *Lab on a Chip*, vol. 13, no. 18, pp. 3569–3577, 2013.
- [11] R. Astaneh, M. Erfan, H. Moghimi, and H. Mobedi, “Changes in morphology of in situ forming plga implant prepared by different polymer molecular weight and its effect on release behavior,” *Journal of Pharmaceutical Sciences*, vol. 98, no. 1, pp. 135–145, 2009.
- [12] M. Aubinet, T. Vesala, and D. Papale, *Eddy covariance: a practical guide to measurement and data analysis*. Springer Science & Business Media, 2012.

- [13] R. Azadi, “Experimental investigation of viscoelastic cavitating and turbulent channel flows subjected to different pressure gradients,” Ph.D. dissertation, 2023.
- [14] R. Azadi and D. S. Nobes, “Hydrodynamic cavitation reduction in semidilute turbulent polymer solution flows,” *Journal of Fluid Mechanics*, vol. 952, A29, 2022.
- [15] S. A. Bahrani, C. Nouar, and A. Neveu, “Transition to chaotic taylor-couette flow in shear-thinning fluids,” in *CFM 2015-22ème Congrès Français de Mécanique*, AFM, Maison de la Mécanique, 39/41 rue Louis Blanc-92400 Courbevoie, 2015.
- [16] A. Barcilon and J. Brindley, “Organized structures in turbulent taylor-couette flow,” *Journal of Fluid Mechanics*, vol. 143, pp. 429–449, 1984.
- [17] P. Berghout, R. Verzicco, R. J. Stevens, D. Lohse, and D. Chung, “Calculation of the mean velocity profile for strongly turbulent taylor–couette flow at arbitrary radius ratios,” *Journal of Fluid Mechanics*, vol. 905, A11, 2020.
- [18] P. Bhamri, R. Narain, and B. Fleck, “Drag reduction using polysaccharides in a taylor–couette flow,” *Polymers*, vol. 9, no. 12, p. 683, 2017.
- [19] M. Bilson and K. Bremhorst, “Direct numerical simulation of turbulent taylor–couette flow,” *Journal of Fluid Mechanics*, vol. 579, pp. 227–270, 2007.
- [20] E. Bodenschatz, W. Pesch, and G. Ahlers, “Recent developments in rayleigh-benard convection,” *Annual Review of Fluid Mechanics*, vol. 32, no. 1, pp. 709–778, 2000.
- [21] A. Brandstater and H. L. Swinney, “Strange attractors in weakly turbulent couette-taylor flow,” *Physical Review A*, vol. 35, no. 5, p. 2207, 1987.
- [22] S. L. Brunton and J. N. Kutz, *Data-driven science and engineering: Machine learning, dynamical systems, and control*. Cambridge University Press, 2022.
- [23] M. Burin *et al.*, “Reduction of ekman circulation within taylor-couette flow,” *Experiments in Fluids*, vol. 40, pp. 962–966, 2006.
- [24] N. Cagney and S. Balabani, “Taylor-couette flow of shear-thinning fluids,” *Physics of Fluids*, vol. 31, no. 5, p. 053102, 2019.
- [25] J. Chen, “Two-point statistics of coherent structure in turbulent flow,” *arXiv preprint arXiv:1908.05422*, 2019.
- [26] D. Coles and C. Van Atta, “Measured distortion of a laminar circular couette flow by end effects,” *Journal of Fluid Mechanics*, vol. 25, no. 3, pp. 513–521, 1966.
- [27] D. Coles, “Transition in circular couette flow,” *Journal of Fluid Mechanics*, vol. 21, no. 3, pp. 385–425, 1965.
- [28] M. Couette, “Etudes sur le frottement des liquides,” Ph.D. dissertation, 1890.
- [29] P. A. Davidson, *Turbulence: an introduction for scientists and engineers*. Oxford university press, 2015.
- [30] E. De Angelis, C. Casciola, R. Benzi, and R. Piva, “Homogeneous isotropic turbulence in dilute polymers,” *Journal of Fluid Mechanics*, vol. 531, pp. 1–10, 2005.
- [31] P. De Gennes, “Towards a scaling theory of drag reduction,” *Physica A: Statistical Mechanics and its Applications*, vol. 140, no. 1-2, pp. 9–25, 1986.

- [32] F. De Gregorio and A. Visingardi, “Vortex detection criteria assessment for piv data in rotorcraft applications,” *Experiments in Fluids*, vol. 61, pp. 1–22, 2020.
- [33] R. Di Prima and H. L. Swinney, “Instabilities and transition in flow between concentric rotating cylinders,” in *Hydrodynamic instabilities and the transition to turbulence*, Springer, 1981, pp. 139–180.
- [34] C. D. Dimitropoulos, R Sureshkumar, and A. N. Beris, “Direct numerical simulation of viscoelastic turbulent channel flow exhibiting drag reduction: Effect of the variation of rheological parameters,” *Journal of Non-Newtonian Fluid Mechanics*, vol. 79, no. 2-3, pp. 433–468, 1998.
- [35] S Dong, “Direct numerical simulation of turbulent taylor–couette flow,” *Journal of Fluid Mechanics*, vol. 587, pp. 373–393, 2007.
- [36] C. S. Dutcher and S. J. Muller, “Spatio-temporal mode dynamics and higher order transitions in high aspect ratio newtonian taylor–couette flows,” *Journal of Fluid Mechanics*, vol. 641, pp. 85–113, 2009.
- [37] B. Eckhardt, S. Grossmann, and D. Lohse, “Torque scaling in turbulent taylor–couette flow between independently rotating cylinders,” *Journal of Fluid Mechanics*, vol. 581, pp. 221–250, 2007.
- [38] M. El-Adawy *et al.*, “On the application of proper orthogonal decomposition (pod) for in-cylinder flow analysis,” *Energies*, vol. 11, no. 9, p. 2261, 2018.
- [39] H. Elçiçek and B. Güzel, “Effect of shear-thinning behavior on flow regimes in taylor–couette flows,” *Journal of Non-Newtonian Fluid Mechanics*, vol. 279, p. 104 277, 2020.
- [40] M. Errante, M. Klein, A. Ferrero, F. Larocca, G. Scovazzi, and M. Germano, “Mixed averaging procedures,” *Flow, Turbulence and Combustion*, pp. 1–8, 2024.
- [41] M. Escudier, I. Gouldson, and D. Jones, “Flow of shear-thinning fluids in a concentric annulus,” *Experiments in Fluids*, vol. 18, pp. 225–238, 1995.
- [42] M. Escudier, I. Gouldson, and D. M. Jones, “Taylor vortices in newtonian and shear-thinning liquids,” *Proceedings of the Royal Society of London. Series A: Mathematical and Physical Sciences*, vol. 449, no. 1935, pp. 155–176, 1995.
- [43] A. Esser and S. Grossmann, “Analytic expression for taylor–couette stability boundary,” *Physics of Fluids*, vol. 8, no. 7, pp. 1814–1819, 1996.
- [44] A. Fischer, “Imaging flow velocimetry with laser mie scattering,” *Applied Sciences*, vol. 7, no. 12, p. 1298, 2017.
- [45] J. R. Fried, *Polymer science and technology*. Pearson Education, 2014.
- [46] Z. Fu and Y. Kawaguchi, “A short review on drag-reduced turbulent flow of inhomogeneous polymer solutions,” *Advances in Mechanical Engineering*, vol. 5, p. 432 949, 2013.
- [47] W. K. George, “Lectures in turbulence for the 21st century,” *Chalmers University of Technology*, vol. 550, 2013.

- [48] S Ghaemi and F Scarano, “Turbulent structure of high-amplitude pressure peaks within the turbulent boundary layer,” *Journal of Fluid Mechanics*, vol. 735, pp. 381–426, 2013.
- [49] L. Graftieaux, M. Michard, and N. Grosjean, “Combining piv, pod and vortex identification algorithms for the study of unsteady turbulent swirling flows,” *Measurement Science and technology*, vol. 12, no. 9, p. 1422, 2001.
- [50] M. D. Graham, “Drag reduction in turbulent flow of polymer solutions,” *Rheology Reviews*, vol. 2, no. 2, pp. 143–170, 2004.
- [51] S. Grossmann, D. Lohse, and C. Sun, “High–reynolds number taylor-couette turbulence,” *Annual Review of Fluid Mechanics*, vol. 48, pp. 53–80, 2016.
- [52] M Gul, G. Elsinga, and J Westerweel, “Experimental investigation of torque hysteresis behaviour of taylor–couette flow,” *Journal of Fluid Mechanics*, vol. 836, pp. 635–648, 2018.
- [53] B. Hanson, R. Jamshidi, A. Redfearn, R. Begley, and C. M. Steele, “Experimental and computational investigation of the iddsi flow test of liquids used in dysphagia management,” *Annals of Biomedical Engineering*, vol. 47, pp. 2296–2307, 2019.
- [54] G. Herth, G. Schornick, and F. L. Buchholz, “Polyacrylamides and poly (acrylic acids),” *Ullmann’s Encyclopedia of Industrial Chemistry*, pp. 1–16, 2000.
- [55] S. Hijazi, M. Freitag, and N. Landwehr, “Pod-galerkin reduced order models and physics-informed neural networks for solving inverse problems for the navier–stokes equations,” *Advanced Modeling and Simulation in Engineering Sciences*, vol. 10, no. 1, pp. 1–38, 2023.
- [56] K. D. Hinsch, “Three-dimensional particle velocimetry,” *Measurement Science and Technology*, vol. 6, no. 6, p. 742, 1995.
- [57] R. Hollerbach and A. Fournier, “End-effects in rapidly rotating cylindrical taylor-couette flow,” in *AIP Conference proceedings*, American Institute of Physics, vol. 733, 2004, pp. 114–121.
- [58] K. D. Housiadas and A. N. Beris, “Polymer-induced drag reduction: Effects of the variations in elasticity and inertia in turbulent viscoelastic channel flow,” *Physics of Fluids*, vol. 15, no. 8, pp. 2369–2384, 2003.
- [59] S. G. Huisman, D. P. van Gils, S. Grossmann, C. Sun, and D. Lohse, “Ultimate turbulent taylor-couette flow,” *Physical Review Letters*, vol. 108, no. 2, p. 024 501, 2012.
- [60] S. G. Huisman, D. Lohse, and C. Sun, “Statistics of turbulent fluctuations in counter-rotating taylor-couette flows,” *Physical Review E*, vol. 88, no. 6, p. 063 001, 2013.
- [61] S. G. Huisman, S. Scharnowski, C. Cierpka, C. J. Kähler, D. Lohse, and C. Sun, “Logarithmic boundary layers in strong taylor-couette turbulence,” *Physical Review Letters*, vol. 110, no. 26, p. 264 501, 2013.
- [62] A. V. Johansson, P. H. Alfredsson, and J. Kim, “Evolution and dynamics of shear-layer structures in near-wall turbulence,” *Journal of Fluid Mechanics*, vol. 224, pp. 579–599, 1991.

- [63] C. J. Kähler, “The significance of coherent flow structures for the turbulent mixing in wall-bounded flows,” Ph.D. dissertation, Citeseer, 2004.
- [64] K Kataoka, H Doi, and T. Komai, “Heat/mass transfer in taylor vortex flow with constant axial flow rates,” *International Journal of Heat and Mass Transfer*, vol. 20, no. 1, pp. 57–63, 1977.
- [65] R. D. Keane and R. J. Adrian, “Theory of cross-correlation analysis of piv images,” *Applied Scientific Research*, vol. 49, pp. 191–215, 1992.
- [66] H. H. Khan, S. F. Anwer, N. Hasan, and S. Sanghi, “Proper orthogonal decomposition of turbulent flow in a straight square duct,” in *Proceedings of 16th Asian Congress of Fluid Mechanics*, Springer, 2021, pp. 545–553.
- [67] J. Kim, P. Moin, and R. Moser, “Turbulence statistics in fully developed channel flow at low reynolds number,” *Journal of Fluid Mechanics*, vol. 177, pp. 133–166, 1987.
- [68] K. Kim, C.-F. Li, R. Sureshkumar, S Balachandar, and R. J. Adrian, “Effects of polymer stresses on eddy structures in drag-reduced turbulent channel flow,” *Journal of Fluid Mechanics*, vol. 584, pp. 281–299, 2007.
- [69] J Kostas, J. Soria, and M. S. Chong, “A comparison between snapshot pod analysis of piv velocity and vorticity data,” *Experiments in Fluids*, vol. 38, pp. 146–160, 2005.
- [70] M. C. Krygier, J. L. Pughe-Sanford, and R. O. Grigoriev, “Exact coherent structures and shadowing in turbulent taylor-couette flow,” *arXiv preprint arXiv:2105.02126*, 2021.
- [71] D. P. Lathrop, J. Fineberg, and H. L. Swinney, “Transition to shear-driven turbulence in couette-taylor flow,” *Physical Review A*, vol. 46, no. 10, p. 6390, 1992.
- [72] LaVision, *Product manual for DaVis 8.4: FlowMaster*, 2013.
- [73] P. LeDuc, C. Haber, G. Bao, and D. Wirtz, “Dynamics of individual flexible polymers in a shear flow,” *Nature*, vol. 399, no. 6736, pp. 564–566, 1999.
- [74] H.-K. Lee, J. Chung, S.-I. Chang, and E. Yoon, “Normal and shear force measurement using a flexible polymer tactile sensor with embedded multiple capacitors,” *Journal of Microelectromechanical Systems*, vol. 17, no. 4, pp. 934–942, 2008.
- [75] G. S. Lewis and H. L. Swinney, “Velocity structure functions, scaling, and transitions in high-reynolds-number couette-taylor flow,” *Physical Review E*, vol. 59, no. 5, p. 5457, 1999.
- [76] L. Lu and V. Sick, “High-speed particle image velocimetry near surfaces,” *JoVE (Journal of Visualized Experiments)*, no. 76, e50559, 2013.
- [77] T. Luchik and W. Tiederman, “Turbulent structure in low-concentration drag-reducing channel flows,” *Journal of Fluid Mechanics*, vol. 190, pp. 241–263, 1988.
- [78] J. L. Lumley, “Drag reduction by additives,” *Annual Review of Fluid Mechanics*, vol. 1, no. 1, pp. 367–384, 1969.
- [79] J. L. Lumley, “The structure of inhomogeneous turbulent flows,” *Atmospheric Turbulence and Radio Wave Propagation*, pp. 166–178, 1967.

- [80] B. Martínez-Arias, J. Peixinho, O. Crumeyrolle, and I. Mutabazi, “Effect of the number of vortices on the torque scaling in taylor–couette flow,” *Journal of Fluid Mechanics*, vol. 748, pp. 756–767, 2014.
- [81] G. Mie, “Beiträge zur optik trüber medien, speziell kolloidaler metallösungen,” *Annalen der physik*, vol. 330, no. 3, pp. 377–445, 1908.
- [82] T. Min, J. Y. Yoo, H. Choi, and D. D. Joseph, “Drag reduction by polymer additives in a turbulent channel flow,” *Journal of Fluid Mechanics*, vol. 486, pp. 213–238, 2003.
- [83] R. S. Mitishita, G. J. Elfring, and I. A. Frigaard, “Statistics and spectral analysis of turbulent duct flows with flexible and rigid polymer solutions,” *Journal of Non-Newtonian Fluid Mechanics*, vol. 311, p. 104952, 2023.
- [84] M Mohammadtabar, R. Sanders, and S Ghaemi, “Turbulent structures of non-newtonian solutions containing rigid polymers,” *Physics of Fluids*, vol. 29, no. 10, p. 103101, 2017.
- [85] S. D. Muralidhar, B. Podvin, L. Mathelin, and Y. Fraigneau, “Spatio-temporal proper orthogonal decomposition of turbulent channel flow,” *Journal of Fluid Mechanics*, vol. 864, pp. 614–639, 2019.
- [86] M. Nemri, S. Charton, and E. Climent, “Mixing and axial dispersion in taylor–couette flows: The effect of the flow regime,” *Chemical Engineering Science*, vol. 139, pp. 109–124, 2016.
- [87] F. Nieuwstadt and J. Den Toonder, *Drag reduction by additives: a review*. Springer, 2001.
- [88] R. Ostilla-Mónico, E. P. Van Der Poel, R. Verzicco, S. Grossmann, and D. Lohse, “Boundary layer dynamics at the transition between the classical and the ultimate regime of taylor-couette flow,” *Physics of Fluids*, vol. 26, no. 1, p. 015114, 2014.
- [89] R. Pandit, P. Perlekar, and S. S. Ray, “Statistical properties of turbulence: An overview,” *Pramana*, vol. 73, no. 1, pp. 157–191, 2009.
- [90] J Parker and P Merati, “An investigation of turbulent taylor-couette flow using laser doppler velocimetry in a refractive index matched facility,” 1996.
- [91] A. S. Pereira, R. M. Andrade, and E. J. Soares, “Drag reduction induced by flexible and rigid molecules in a turbulent flow into a rotating cylindrical double gap device: Comparison between poly (ethylene oxide), polyacrylamide, and xanthan gum,” *Journal of Non-Newtonian Fluid Mechanics*, vol. 202, pp. 72–87, 2013.
- [92] P. Perlekar, D. Mitra, and R. Pandit, “Manifestations of drag reduction by polymer additives in decaying, homogeneous, isotropic turbulence,” *Physical Review Letters*, vol. 97, no. 26, p. 264501, 2006.
- [93] D. Pirro and M. Quadrio, “Direct numerical simulation of turbulent taylor–couette flow,” *European Journal of Mechanics-B/Fluids*, vol. 27, no. 5, pp. 552–566, 2008.
- [94] S. B. Pope, *Turbulent flows*, 11. 2001, vol. 12, pp. 2020–2021.
- [95] A. K. Prasad, “Stereoscopic particle image velocimetry,” *Experiments in Fluids*, vol. 29, no. 2, pp. 103–116, 2000.

- [96] A. K. Prasad and K. Jensen, “Scheimpflug stereocamera for particle image velocimetry in liquid flows,” *Applied Optics*, vol. 34, no. 30, pp. 7092–7099, 1995.
- [97] I. Procaccia, V. S. Lvov, and R. Benzi, “Colloquium: Theory of drag reduction by polymers in wall-bounded turbulence,” *Reviews of Modern Physics*, vol. 80, no. 1, p. 225, 2008.
- [98] M. Raffel, C. E. Willert, and J. Kompenhans, *Particle image velocimetry: a practical guide*. Springer, 1998, vol. 2.
- [99] F. Ravelet, R. Delfos, and J. Westerweel, “Influence of global rotation and reynolds number on the large-scale features of a turbulent taylor–couette flow,” *Physics of Fluids*, vol. 22, no. 5, p. 055103, 2010.
- [100] L. Rayleigh, “On the dynamics of revolving fluids,” *Proceedings of the Royal Society of London. Series A, Containing Papers of a Mathematical and Physical Character*, vol. 93, no. 648, pp. 148–154, 1917.
- [101] W. E. Rochefort and S. Middleman, “Rheology of xanthan gum: Salt, temperature, and strain effects in oscillatory and steady shear experiments,” *Journal of Rheology*, vol. 31, no. 4, pp. 337–369, 1987.
- [102] M. M. Rogers and P. Moin, “The structure of the vorticity field in homogeneous turbulent flows,” *Journal of Fluid Mechanics*, vol. 176, pp. 33–66, 1987.
- [103] A. Rollin and F. Seyer, “Velocity measurements in turbulent flow of viscoelastic solutions,” *The Canadian Journal of Chemical Engineering*, vol. 50, no. 6, pp. 714–718, 1972.
- [104] M. Rovira, K. Engvall, and C. Duwig, “Proper orthogonal decomposition analysis of the large-scale dynamics of a round turbulent jet in counterflow,” *Physical Review Fluids*, vol. 6, no. 1, p. 014701, 2021.
- [105] C. W. Rowley, “Model reduction for fluids, using balanced proper orthogonal decomposition,” *International Journal of Bifurcation and Chaos*, vol. 15, no. 03, pp. 997–1013, 2005.
- [106] H. Royer and M. Stanislas, “Stereoscopic and holographic approaches to get the third velocity component in piv,” *Lecture series-van Karman Institute for Fluid Dynamics*, vol. 3, pp. I1–I56, 1996.
- [107] M. Rudd, “Velocity measurements made with a laser dopplermeter on the turbulent pipe flow of a dilute polymer solution,” *Journal of Fluid Mechanics*, vol. 51, no. 4, pp. 673–685, 1972.
- [108] M. Rudman and H. Blackburn, “Turbulence modification in shear thinning fluids: Preliminary results for power law rheology,” in *18th Australian Fluid Mechanics Conference. Launceston, Australia*, 2012.
- [109] D. Samanta, Y. Dubief, M. Holzner, C. Schäfer, A. N. Morozov, and Wagner, “Elastoinertial turbulence,” *Proceedings of the National Academy of Sciences*, vol. 110, no. 26, pp. 10557–10562, 2013.

- [110] W. R. dos Santos, E. S. Caser, E. J. Soares, and R. N. Siqueira, “Drag reduction in turbulent flows by diutan gum: A very stable natural drag reducer,” *Journal of Non-Newtonian Fluid Mechanics*, vol. 276, p. 104 223, 2020.
- [111] B Schnurr, F Gittes, F. MacKintosh, and C. Schmidt, “Determining microscopic viscoelasticity in flexible and semiflexible polymer networks from thermal fluctuations,” *Macromolecules*, vol. 30, no. 25, pp. 7781–7792, 1997.
- [112] M. Schrimpf, J. Esteban, H. Warmeling, T. Färber, A. Behr, and A. J. Vorholt, “Taylor-couette reactor: Principles, design, and applications,” *AIChE Journal*, vol. 67, no. 5, e17228, 2021.
- [113] I. Shabaka, M Abdel Wahab, S. Hamza, M. El-Bakry, and S Hashem, “On rheological behavior of aqueous polyacrylamide solution empirical relation of the viscosity as a function of concentration and shear rate,” *Int. J. Adv. Res.*, vol. 4, no. 7, pp. 1499–1507, 2016.
- [114] R. Shaw, C. D. Andereck, L. Reith, and H. L. Swinney, “Superposition of traveling waves in the circular couette system,” *Physical Review Letters*, vol. 48, no. 17, p. 1172, 1982.
- [115] J Singh, M Rudman, and H. Blackburn, “The influence of shear-dependent rheology on turbulent pipe flow,” *Journal of Fluid Mechanics*, vol. 822, pp. 848–879, 2017.
- [116] L. Sirovich, “Turbulence and the dynamics of coherent structures. i. coherent structures,” *Quarterly of Applied Mathematics*, vol. 45, no. 3, pp. 561–571, 1987.
- [117] G. Smith and A. Townsend, “Turbulent couette flow between concentric cylinders at large taylor numbers,” *Journal of Fluid Mechanics*, vol. 123, pp. 187–217, 1982.
- [118] T. R. Smith, J. Moehlis, and P. Holmes, “Low-dimensional modelling of turbulence using the proper orthogonal decomposition: A tutorial,” *Nonlinear Dynamics*, vol. 41, pp. 275–307, 2005.
- [119] S. Srinivasan, J. A. Kleingartner, J. B. Gilbert, R. E. Cohen, A. J. Milne, and G. H. McKinley, “Sustainable drag reduction in turbulent taylor-couette flows by depositing sprayable superhydrophobic surfaces,” *Physical Review Letters*, vol. 114, no. 1, p. 014 501, 2015.
- [120] R Sureshkumar, A. N. Beris, and R. A. Handler, “Direct numerical simulation of the turbulent channel flow of a polymer solution,” *Physics of Fluids*, vol. 9, no. 3, pp. 743–755, 1997.
- [121] G. I. Taylor, “Viii. stability of a viscous liquid contained between two rotating cylinders,” *Philosophical Transactions of the Royal Society of London. Series A, Containing Papers of a Mathematical or Physical Character*, vol. 223, no. 605-615, pp. 289–343, 1923.
- [122] L. Thais, A. Tejada-Martinez, T. Gatski, and G. Mompean, “Temporal large eddy simulations of turbulent viscoelastic drag reduction flows,” *Physics of Fluids*, vol. 22, no. 1, p. 013 103, 2010.

- [123] W. Thielicke and R. Sonntag, “Particle image velocimetry for matlab: Accuracy and enhanced algorithms in pivlab,” *Journal of Open Research Software*, vol. 9, no. 1, 2021.
- [124] D Thirumalai and J. Bhattacharjee, “Polymer-induced drag reduction in turbulent flows,” *Physical Review E*, vol. 53, no. 1, p. 546, 1996.
- [125] W. G. Tiederman, “The effect of dilute polymer solutions on viscous drag and turbulence structure,” *Structure of Turbulence and Drag Reduction*, pp. 187–200, 1990.
- [126] S Topayev, C Nouar, D Bernardin, A Neveu, and S. Bahrani, “Taylor-vortex flow in shear-thinning fluids,” *Physical Review E*, vol. 100, no. 2, p. 023 117, 2019.
- [127] S. Topayev, C. Nouar, and J. Dusek, “Secondary instabilities in taylor–couette flow of shear-thinning fluids,” *Journal of Fluid Mechanics*, vol. 933, 2022.
- [128] U. Ullum, J. J. Schmidt, P. S. Larsen, and D. McCluskey, “Statistical analysis and accuracy of piv data,” *Journal of Visualization*, vol. 1, no. 2, pp. 205–216, 1998.
- [129] D. P. Van Gils, S. G. Huisman, G.-W. Bruggert, C. Sun, and D. Lohse, “Torque scaling in turbulent taylor-couette flow with co-and counterrotating cylinders,” *Physical Review Letters*, vol. 106, no. 2, p. 024 502, 2011.
- [130] H. S. Virk Mickley and Smith, “The ultimate asymptote and mean flow structure in toms phenomenon,” 1970.
- [131] P. S. Virk, “Drag reduction fundamentals,” *AIChE Journal*, vol. 21, no. 4, pp. 625–656, 1975.
- [132] R. Vitkovicova, Y. Yokoi, and T. Hyhlik, “Identification of structures and mechanisms in a flow field by pod analysis for input data obtained from visualization and piv,” *Experiments in Fluids*, vol. 61, pp. 1–21, 2020.
- [133] A. Volk and C. J. Kähler, “Density model for aqueous glycerol solutions,” *Experiments in Fluids*, vol. 59, no. 5, p. 75, 2018.
- [134] L.-W. Wang, C. Pan, and J.-J. Wang, “Wall-attached and wall-detached eddies in proper orthogonal decomposition modes of a turbulent channel flow,” *Physics of Fluids*, vol. 34, no. 9, 2022.
- [135] L. Wang, C. Pan, J. Wang, and Q. Gao, “Statistical signatures of component wall-attached eddies in proper orthogonal decomposition modes of a turbulent boundary layer,” *Journal of Fluid Mechanics*, vol. 944, A26, 2022.
- [136] M. Warholic, D. Heist, M Katcher, and T. Hanratty, “A study with particle-image velocimetry of the influence of drag-reducing polymers on the structure of turbulence,” *Experiments in fluids*, vol. 31, pp. 474–483, 2001.
- [137] M. Warholic, H Massah, and T. Hanratty, “Influence of drag-reducing polymers on turbulence: Effects of reynolds number, concentration and mixing,” *Experiments in Fluids*, vol. 27, no. 5, pp. 461–472, 1999.
- [138] S. T. Wereley and R. M. Lueptow, “Spatio-temporal character of non-wavy and wavy taylor–couette flow,” *Journal of Fluid Mechanics*, vol. 364, pp. 59–80, 1998.

- [139] J. Westerweel, “Fundamentals of digital particle image velocimetry,” *Measurement Science and Technology*, vol. 8, no. 12, p. 1379, 1997.
- [140] C. M. White and M. G. Mungal, “Mechanics and prediction of turbulent drag reduction with polymer additives,” *Annu. Rev. Fluid Mech.*, vol. 40, pp. 235–256, 2008.
- [141] C Willert, S. T. Wereley, and J. Kompenhans, *Particle image velocimetry: A practical guide*, 2007.
- [142] W. W. Willmarth and Wei, “Laser anemometer measurements of reynolds stress in a turbulent channel flow with drag reducing polymer additives,” *The Physics of Fluids*, vol. 30, no. 4, pp. 933–935, 1987.
- [143] H Wiswell, B Snow, F. Tricouros, A. Smits, and T Van Buren, “End effects in low aspect ratio taylor–couette flow,” *Philosophical Transactions of the Royal Society A*, vol. 381, no. 2243, p. 20 220 118, 2023.
- [144] Z. Wu, D. Laurence, S. Utyuzhnikov, and I. Afgan, “Proper orthogonal decomposition and dynamic mode decomposition of jet in channel crossflow,” *Nuclear Engineering and Design*, vol. 344, pp. 54–68, 2019.
- [145] L. Xi, “Turbulent drag reduction by polymer additives: Fundamentals and recent advances,” *Physics of Fluids*, vol. 31, no. 12, p. 121 302, 2019.
- [146] I Zadrazil, A Bismarck, G. Hewitt, and C. Markides, “Shear layers in the turbulent pipe flow of drag reducing polymer solutions,” *Chemical Engineering Science*, vol. 72, pp. 142–154, 2012.

# Appendix A: Coordinate Conversion

## A.1 Cartesian Coordinate System to Cylindrical Coordinate system

The relation between the Cartesian coordinate and the Cylindrical coordinate is given by:

$$x = r \cos \theta \quad (\text{A.1})$$

$$y = r \sin \theta \quad (\text{A.2})$$

$$z = z \quad (\text{A.3})$$

The gradient operator on a scalar  $F$ :

$$\nabla F = \frac{\partial F}{\partial r} \mathbf{e}_r + \frac{1}{r} \frac{\partial F}{\partial \theta} \mathbf{e}_\theta + \frac{\partial F}{\partial z} \mathbf{e}_z \quad (\text{A.4})$$

Divergence of a vector  $\mathbf{f}$  ( $\mathbf{f} = f_r \mathbf{e}_r + f_\theta \mathbf{e}_\theta + f_z \mathbf{e}_z$ ):

$$\nabla \cdot \mathbf{f} = \frac{1}{r} \frac{\partial}{\partial r} (r f_r) + \frac{1}{r} \frac{\partial f_\theta}{\partial \theta} + \frac{\partial f_z}{\partial z} \quad (\text{A.5})$$

Curl of a vector  $\mathbf{f}$  ( $\mathbf{f} = f_r \mathbf{e}_r + f_\theta \mathbf{e}_\theta + f_z \mathbf{e}_z$ ):

$$\nabla \times \mathbf{f} = \left( \frac{1}{r} \frac{\partial f_z}{\partial \theta} - \frac{\partial f_\theta}{\partial z} \right) \mathbf{e}_r + \left( \frac{\partial f_r}{\partial z} - \frac{\partial f_z}{\partial r} \right) \mathbf{e}_\theta + \frac{1}{r} \left( \frac{\partial}{\partial r} (r f_\theta) - \frac{\partial f_r}{\partial \theta} \right) \mathbf{e}_z \quad (\text{A.6})$$

Laplacian of a scalar  $F$ :

$$\nabla^2 F = \frac{1}{r} \frac{\partial}{\partial r} \left( r \frac{\partial F}{\partial r} \right) + \frac{1}{r^2} \frac{\partial^2 F}{\partial \theta^2} + \frac{\partial^2 F}{\partial z^2} \quad (\text{A.7})$$

# Appendix B: Equation Derivations

## B.1 Relation between $C_{f,s}$ and $C_{f,l}$

Skin coefficient by Srinivasan *et al.* (2015) :

$$C_{f,s} = \frac{\tau_{w,i}}{\frac{1}{2}\rho U_{ref}^2}. \quad (\text{B.1})$$

Inner wall shear stress is given by:

$$\tau_{w,i} = \frac{\langle \mathbb{T} \rangle_t}{2\pi r_i^2 l_c}. \quad (\text{B.2})$$

Substitute Equation B.2 into Equation B.1:

$$C_{f,s} = \frac{\langle \mathbb{T} \rangle_t}{\rho \pi r_i^2 l_c U_{ref}^2}. \quad (\text{B.3})$$

Lathrop *et al.* (1992) defined skin friction coefficient:

$$C_{f,l} = \frac{G}{\text{Re}^2}, \quad (\text{B.4})$$

where  $G$  is dimensionless torque.

The mean torque can be expressed in terms of  $G$ :

$$\langle T \rangle_t = \rho \nu^2 l_c G. \quad (\text{B.5})$$

Substitute Equation B.5 into Equation B.4:

$$C_{f,l} = \frac{\langle \mathbb{T} \rangle_t}{\rho \nu^2 l_c \text{Re}^2}. \quad (\text{B.6})$$

The Reynolds number is given by:

$$\text{Re} = \omega_r r_i (r_o - r_i) / \nu. \quad (\text{B.7})$$

Substitute Equation B.7 into Equation B.6:

$$C_{f,l} = \frac{\langle \text{T} \rangle_t}{\rho l_c U_{ref}^2 r_i (r_o - r_i)^2}. \quad (\text{B.8})$$

Thus the relation between  $C_{f,l}$  and  $C_{f,s}$  can be obtained:

$$\frac{C_{f,l}}{C_{f,s}} = \frac{\pi r_i^2}{(r_o - r_i)^2}. \quad (\text{B.9})$$

# Appendix C: Matlab Code

## C.1 Code for POD Analysis

Listing C.1: Snapshot-POD code

```
%% POD code

clear all
close all
clc

load('G:\Water_125RPM_FILE\125rpm_water\TC_Struct_water_125rpm.mat')
temp1 = size(TC(1).U(:,1));
wavelength = 2.209;
r_i = 0.060325;
r_o = 0.079375;
d = (r_o - r_i)*10^3;
%% resolution calculation
Factor_X = (max(X(:)) - min(X(:)))/(size(X,2)-1);
x_min = 0;
y_min = 0;
x_max = 1;
y_max_temp = size(X, 1) *Factor_X;
y_max = y_max_temp/(d);
%% time correlated visualization
% for i=1:100 %% max 3000
%
%     figure(1);
%     clf;           % clear the figure
%     imagesc([x_min x_max], [y_min y_max],(TC(i).W))
%     set(gca,'YDir','normal')
%     set(gcf,'color','w')
%     axis equal
%     set(gca,'CLim',[min(TC(:).U) max(TC(:).U)])
%     colormap('jet');
%     h=colorbar
%     set(gcf,'position',[200 200 500 800])
%     caxis([0, U_ref]);
%
%     xlabel(gca,'$r^{*}$','FontSize',28,'Interpreter','latex')
%     ylabel(gca,'$z^{*}$','FontSize',28,'Interpreter','latex')
%     ylabel(h, 'Instantaneous Velocity, m/s','FontSize',16,'FontName','Times New Roman');
%     pause(0.05)
%
% end

%% calculate average and fluctuations
I=size(TC(1).U,1);
J=size(TC(1).V,2);
n_snap= 3000          ;
Uinf=1;  %% actual value is 5 m/s
```

```

for i=1:n_snap
    X_Velocity_total(:,i)=1/Uinf.* [TC(i).U(:); TC(i).V(:)] ; % generate the data matrix (containing
% X_U(:,i)=[TC(i).U(:)] ; % generate the data matrix U
% X_V(:,i)=[TC(i).V(:)] ; % generate the data matrix V
end

AVG = mean(X_Velocity_total,2);
% AVG_U = mean(X_U,2);
% AVG_V = mean(X_V,2);
% AVG=mean(x(1:size(data(1).U(:)),1),2);
% %% plot mean kinetic energy
% figure
% AVG_field_U = reshape(AVG(1:temp1, 1),I,J);
% AVG_field_V = reshape(AVG(temp1+1:end, 1),I,J);
% imagesc([x_min x_max], [y_min y_max], AVG_field_U.^2+AVG_field_V.^2) % to illustrate Kinetic energy
% colormap('jet');
% axis equal
%%
% subtracting the mean from each column of A
for i=1:n_snap
% xp(:,i)=X_Velocity_total(:,i)-AVG;
xp(:,i)=X_Velocity_total(:,i) - AVG;
% xp(:,i) = X_Velocity_total(:,i) ;
end

%% clear vars
clearvars -except xp n_snap temp1 I J x_min x_max y_min y_max AVG
%% POD modes, method of snapshots

C = xp'*xp/n_snap ; % The correlation matrix C divided by the number of samples
[corr_U ,corr_S ,corr_V]=svd(C, "econ") ;
ui=xp*corr_U ; % POD modes

%%
%% Ghaemi code
for i=1:size(corr_S)
ui2(:,i)=ui(:,i)/(norm(ui(:,i),2));
end
a=ui2'*xp; %% amplitudes
%% %% Andrew's comment 1 on modes
% [U,S,V]=svd(xp, 'econ') ;
% % plot my modes
% U_S = U*S;
% figure

%%%%%%%%%%%%%%%%%%%%%%%%%%%%%%%%%%%%%%%%%%%%%%%%%%%%%%%%%%%%%%%%%%%%%%%%
figure
set(gcf,'color','w')
%%%%%%%%%%%%%%%%%%%%%%%%%%%%%%%%%%%%%%%%%%%%%%%%%%%%%%%%%%%%%%%%%%%%%%%%
% set number of modes to be investigated
N_pod = 6;
%% plot spatial modes of U
for i = 1: N_pod
subplot(2,3,i)
mode=i;
%figure
imagesc([x_min x_max], [y_min y_max], reshape(ui2(1:temp1, mode),I,J)) % to illustrate a mode
set(gca,'YDir','normal')
title(['Mode ', num2str(mode)])
colormap('jet');
xlabel(gca,'r^{*}$','FontSize',28,'Interpreter','latex')
ylabel(gca,'z^{*}$','FontSize',28,'Interpreter','latex')
set(gca,'FontSize',28, 'FontName','Times' );
pbaspect([1, 1.5, 1]);
set(gcf,'color','w')
colorbar
set(gca,'CLim',[-10^(-2) 10^(-2)])

```

```

% Set colorbar ticks
colorbar('Ticks', [-10^(-2), 0, 10^(-2)], 'TickLabels', {'-10^{-2}', '0', '10^{-2}'});

% Optional: Set scientific notation for tick labels
h = gca;
h.YAxis.TickLabelFormat = '%g';

end

%%%%%%%%%%%%%%%%%%%%%%%%%%%%%%%%%%%%%%%%%%%%%%%%%%%%%%%%%%%%%%%%%%%%%%%%%%%%%%
%%
figure
set(gcf, 'color', 'w')
%%%%%%%%%%%%%%%%%%%%%%%%%%%%%%%%%%%%%%%%%%%%%%%%%%%%%%%%%%%%%%%%%%%%%%%%%%%%%%
% set number of modes to be investigated
N_pod = 6;
%% plot spatial modes of V
for i = 1: N_pod
subplot(2,3,i)
mode=i;
%figure
imagesc([x_min x_max], [y_min y_max], reshape(ui2(templ+1:end, mode),I,J)) % to illustrate a mode
set(gca, 'YDir', 'normal')
title(['Mode ', num2str(mode)])
colormap('jet');
xlabel(gca, '$r^{*}$', 'FontSize', 28, 'Interpreter', 'latex')
ylabel(gca, '$z^{*}$', 'FontSize', 28, 'Interpreter', 'latex')
set(gca, 'FontSize', 28, 'FontName', 'Times' );
pbaspect([1, 1.5, 1]);
set(gcf, 'color', 'w')
colorbar
set(gca, 'CLim', [-10^(-2) 10^(-2)])
% Set colorbar ticks
colorbar('Ticks', [-10^(-2), 0, 10^(-2)], 'TickLabels', {'-10^{-2}', '0', '10^{-2}'});
% Optional: Set scientific notation for tick labels
h = gca;
h.YAxis.TickLabelFormat = '%g';
end

%%%%%%%%%%%%%%%%%%%%%%%%%%%%%%%%%%%%%%%%%%%%%%%%%%%%%%%%%%%%%%%%%%%%%%%%%%%%%% spatial mode + eigenvector%%%%%%%%%%%%%%%%%%%%%%%%%%%%%%%%%%%%%%%%%%%%%%%%%%%%%%%%%%%%%%%%%%%%%%%%%%%%%%
%% Spatial mode + eigenvector plot together
figure
set(gcf, 'color', 'w')
%%%%%%%%%%%%%%%%%%%%%%%%%%%%%%%%%%%%%%%%%%%%%%%%%%%%%%%%%%%%%%%%%%%%%%%%%%%%%%
% set number of modes to be investigated
N_pod = 6;
%% plot spatial modes of U
for i = 1: N_pod
subplot(2,3,i)
mode=i;
%figure
imagesc([x_min x_max], [y_min y_max], flipud(reshape(ui2(1:templ, mode),I,J))) % to illustrate a mode
set(gca, 'YDir', 'normal')
title(['Mode ', num2str(mode)])
colormap('jet');
xlabel(gca, '$r^{*}$', 'FontSize', 28, 'Interpreter', 'latex')
ylabel(gca, '$z^{*}$', 'FontSize', 28, 'Interpreter', 'latex')
set(gca, 'FontSize', 28, 'FontName', 'Times' );
pbaspect([1, 1.5, 1]);
set(gcf, 'color', 'w')
colorbar
set(gca, 'CLim', [-10^(-2) 10^(-2)])
% Set colorbar ticks
colorbar('Ticks', [-10^(-2), 0, 10^(-2)], 'TickLabels', {'-10^{-2}', '0', '10^{-2}'});
% Optional: Set scientific notation for tick labels
h = gca;
h.YAxis.TickLabelFormat = '%g';

```

```

hold on

x_prime = linspace(x_min, x_max, J);
y_prime = linspace(y_min, y_max, I);
[X_prime, Y_prime] = meshgrid(x_prime, y_prime);
Y_prime = flipud(Y_prime);
% Create 2D vector plot
factor = 150;
cc1 = factor.*reshape(ui2(1:temp1, mode),I,J);
cc2 = factor.*reshape(ui2(temp1+1:end, mode),I,J);
% cc2 = zeros(I, J);
quiver(X_prime(1:10:end, 1:10:end), Y_prime(1:10:end, 1:10:end),cc1(1:10:end, 1:10:end) ,cc2(1:10:end, 1:10:end)

end
%%
figure
set(gcf,'color','w')
%%%%%%%%%%%%%%%%%%%%%%%%%%%%%%%%%%%%%%%%%%%%%%%%%%%%%%%%%%%%%%%%%%%%%%%%
% set number of modes to be investigated
N_pod = 6;
%% plot spatial modes of V
for i = 1: N_pod
subplot(2,3,i)
mode=i;
%figure
imagesc([x_min x_max], [y_min y_max], flipud(reshape(ui2(temp1+1:end, mode),I,J))) % to illustrate a mode
set(gca,'YDir','normal')
title(['Mode ', num2str(mode)])
colormap('jet');
xlabel(gca,'$r^{*}$','$', 'FontSize',28,'Interpreter','latex')
ylabel(gca,'$z^{*}$','$', 'FontSize',28,'Interpreter','latex')
set(gca,'FontSize',28, 'FontName','Times' );
pbaspect([1, 1.5, 1]);
set(gcf,'color','w')
colorbar
set(gca,'CLim',[-10^(-2) 10^(-2)])
% Set colorbar ticks
colorbar('Ticks', [-10^(-2), 0, 10^(-2)], 'TickLabels', {'-10^{-2}', '0', '10^{-2}'});
% Optional: Set scientific notation for tick labels
h = gca;
h.YAxis.TickLabelFormat = '%g';
hold on

x_prime = linspace(x_min, x_max, J);
y_prime = linspace(y_min, y_max, I);
[X_prime, Y_prime] = meshgrid(x_prime, y_prime);
Y_prime = flipud(Y_prime);
% Create 2D vector plot
factor = 150;
cc1 = factor.*reshape(ui2(1:temp1, mode),I,J);
cc2 = factor.*reshape(ui2(temp1+1:end, mode),I,J);
quiver(X_prime(1:10:end, 1:10:end), Y_prime(1:10:end, 1:10:end),cc1(1:10:end, 1:10:end) ,cc2(1:10:end, 1:10:end)

end

%% create a 2 * 3 mode distribution for thesis
% control distance btw plots

%

figure
set(gcf,'color','w')
%%%%%%%%%%%%%%%%%%%%%%%%%%%%%%%%%%%%%%%%%%%%%%%%%%%%%%%%%%%%%%%%%%%%%%%%
% set number of modes to be investigated
N_pod = 6;
N_pod_x = 3;
%%
%%
%%

```

```

for i = 1: N_pod
    if i <=3
mode=i;
subplot(2,3,i)
%figure
imagesc([x_min x_max], [y_min y_max], flipud(reshape(ui2(1:temp1, mode),I,J))) % to illustrate a mode
else
    mode = i - 3;
    subplot(2,3,i)
imagesc([x_min x_max], [y_min y_max], flipud(reshape(ui2(temp1+1:end, mode),I,J))) % to illustrate a mode
    end

%figure

set(gca,'YDir','normal')
title(['Mode ', num2str(mode)])
colormap('jet');
xlabel(gca,' $r^{[*]}$ ','FontSize',28,'Interpreter','latex')
ylabel(gca,' $z^{[*]}$ ','FontSize',28,'Interpreter','latex')
set(gca,'FontSize',28,'FontName','Times');
pbaspect([1, 1.5, 1]);
set(gcf,'color','w')
colorbar
set(gca,'CLim',[-10^(-2) 10^(-2)])
% Set colorbar ticks
colorbar('Ticks', [-10^(-2), 0, 10^(-2)], 'TickLabels', {'-10^{-2}', '0', '10^{-2}'});
% Optional: Set scientific notation for tick labels
h = gca;
h.YAxis.TickLabelFormat = '%g';
hold on

x_prime = linspace(x_min, x_max, J);
y_prime = linspace(y_min, y_max, I);
[X_prime, Y_prime] = meshgrid(x_prime, y_prime);
Y_prime = flipud(Y_prime);
% Create 2D vector plot
factor = 150;
cc1 = factor.*reshape(ui2(1:temp1, mode),I,J);
cc2 = factor.*reshape(ui2(temp1+1:end, mode),I,J);
quiver(X_prime(1:10:end, 1:10:end), Y_prime(1:10:end, 1:10:end), cc1(1:10:end, 1:10:end), cc2(1:10:end, 1:10:end)
end
% set(ha(1:4),'XTickLabel',''); set(ha,'YTickLabel','')
% % Manually adjust the horizontal space between subplots
% subplot('Position', [0.1, 0.1, 0.25, 0.8]); % Adjust the values as needed
% subplot('Position', [0.4, 0.1, 0.25, 0.8]);
% subplot('Position', [0.7, 0.1, 0.25, 0.8]);
%
% % Repeat for the second row
% subplot('Position', [0.1, 0.1, 0.25, 0.4]);
% subplot('Position', [0.4, 0.1, 0.25, 0.4]);
% subplot('Position', [0.7, 0.1, 0.25, 0.4]);

% Show the plot
% Set the horizontal spacing between subplots
% horizontalSpacing = 0.02; % Adjust this value as needed
% Specify the number of rows and columns
% rows = 2;
% cols = 3;
% % Adjust the horizontal spacing between subplots
% hFig =(gcf);
% figPos = get(hFig, 'Position');
% figPos(3) = figPos(3) - (cols - 1) * horizontalSpacing;
% set(hFig, 'Position', figPos);
%% plot them separately
%%
for i = 1: N_pod
    if i <=3
mode=i;

```

```

% subplot(2,3,i)
figure
imagesc([x_min x_max], [y_min y_max], flipud(reshape(ui2(1:temp1, mode),I,J))) % to illustrate a mode
else
    mode = i - 3;
% subplot(2,3,i)
figure
imagesc([x_min x_max], [y_min y_max], flipud(reshape(ui2(temp1+1:end, mode),I,J))) % to illustrate a mode
end

%figure

set(gca, 'YDir', 'normal')
title(['Mode ', num2str(mode)])
colormap('jet');
xlabel(gca, '$r^{*}$', 'FontSize', 30, 'Interpreter', 'latex')
ylabel(gca, '$z^{*}$', 'FontSize', 30, 'Interpreter', 'latex')
set(gca, 'FontSize', 30, 'FontName', 'Times' );
pbaspect([1, 1.8, 1]);
set(gcf, 'color', 'w')
colorbar
set(gca, 'CLim', [-10^(-2) 10^(-2)])
% Set colorbar ticks
colorbar('Ticks', [-10^(-2), 0, 10^(-2)], 'TickLabels', {'-10^{-2}', '0', '10^{-2}'});
% Optional: Set scientific notation for tick labels
h = gca;
h.YAxis.TickLabelFormat = '%g';
hold on

x_prime = linspace(x_min, x_max, J);
y_prime = linspace(y_min, y_max, I);
[X_prime, Y_prime] = meshgrid(x_prime, y_prime);
Y_prime = flipud(Y_prime);
% Create 2D vector plot
factor = 150;
cc1 = factor.*reshape(ui2(1:temp1, mode),I,J);
cc2 = factor.*reshape(ui2(temp1+1:end, mode),I,J);
quiver(X_prime(1:10:end, 1:10:end), Y_prime(1:10:end, 1:10:end), ...
cc1(1:10:end, 1:10:end), cc2(1:10:end, 1:10:end), 'Color', 'k');
end
%% mode energy
tot_energy = sum(diag(corr_S)); %total energy is the sum of all the eigenvalues; eigenvalues are fr

for i=1:n_snap
    mode_eng(i)=corr_S(i,i)/tot_energy;
end

figure;
plot(100.*mode_eng , 'LineStyle', '-','Color', 'b','Marker', 'o' , 'MarkerFaceColor', [0 0.4 0.7] )
axis([1 10 0 100])
ylabel(gca, 'Mode Energy, %')
xlabel(gca, 'Mode number')
set(gca, 'FontSize', 28, 'FontName', 'Times' );
set(gca, 'FontSize', 28, 'FontName', 'Times' );
% Set the plot box aspect ratio to 4:3
pbaspect([4 4 1]);
set(gcf, 'color', 'w')
legend('Water, Re = 15000')
% grid on
%% plot out the eigenvalue
for j=1:n_snap
    Eig_eng(j)=corr_S(j,j);
end

figure
semilogy(Eig_eng, 'LineStyle', '-','Color', 'b','Marker', 'o' , 'MarkerFaceColor', [0 0.4 0.7] )
axis([0 3000 10^(-5) 10])
ylabel(gca, 'Singular values, $\sigma_{r}$', 'Interpreter', 'latex')

```

```

xlabel(gca,'Mode number, $r$', 'Interpreter', 'latex')
set(gca,'FontSize',28, 'FontName', 'Times' );
set(gca,'FontSize',28, 'FontName', 'Times' );
% Set the plot box aspect ratio to 4:3
pbaspect([4 4 1]);
set(gcf,'color','w')
legend('Water, Re = 15000')

%%
%%%%%%%%%%%%%%%%%%%%%%%%%%%%%%%%%%%%%%%%%%%%%%%%%%%%%%%%%%%%%%%%%%%%%%%%
%% time coefficient
figure
plot([0:n_snap-1], a(1,:), 'LineWidth',2);
xlabel('time [s]')
ylabel('time-dependent coefficient')
set(gca,'FontSize',28);
grid on

% shorter time coefficient plot
figure
plot([0:50], a(1,1:51), 'LineWidth',2);
xlabel('time [s]')
ylabel('time-dependent coefficient')
set(gca,'FontSize',28);
grid on

%%%%%%%%%%%%%%%%%%%%%%%%%%%%%%%%%%%%%%%%%%%%%%%%%%%%%%%%%%%%%%%%%%%%%%%%
%%%%%%%%%%%%%%%%%%%%%%%%%%%%%%%%%%%%%%%%%%%%%%%%%%%%%%%%%%%%%%%%%%%%%%%%
%% reconstruction (ROD)
clearvars -except ui2 a xp temp1 x_min x_max y_min y_max I J AVG
%% reconstruction
n_mode=107;

PHI=ui2(:,1:n_mode);
% PHI=ui2(:,n_mode);
AMP=a(1:n_mode,:);
% AMP=a(n_mode,:);
u_test=PHI*AMP;
%%
%%
% close all

i=15; %% any instantaneous time instant

%%

figure
subplot(1,2,1)
imagesc([x_min x_max], [y_min y_max], reshape(xp(1:temp1,i),I,J)) % Original fluctuation
set(gca,'CLim',[-0.1 0.1])
h=colorbar
set(gca,'YDir','normal')
% set(gcf,'position',[200 5 500 650])
colormap('jet');
xlabel(gca,'$r^{*}$', 'FontSize',28, 'Interpreter', 'latex')
ylabel(gca,'$z^{*}$', 'FontSize',28, 'Interpreter', 'latex')
set(gca,'FontSize',28, 'FontName', 'Times' );

```

```

pbaspect([1, 1.5, 1]);
ylabel(h, 'Velocity fluctuation, m/s', 'FontSize', 16, 'FontName', 'Times New Roman');

%axis equal

set(gcf, 'color', 'w')
subplot(1,2,2)
imagesc([x_min x_max], [y_min y_max], reshape(u_test(1:templ,i),I,J)) % to illustrate ROM
set(gca, 'CLim', [-0.1 0.1])
set(gca, 'YDir', 'normal')
h=colorbar
% set(gcf, 'position', [200 5 500 600])
colormap('jet');
% xlabel(gca, '$r^{*}$', 'FontSize', 28, 'Interpreter', 'latex')
% ylabel(gca, '$z^{*}$', 'FontSize', 28, 'Interpreter', 'latex')
set(gca, 'FontSize', 28, 'FontName', 'Times');
pbaspect([1, 1.5, 1]);
ylabel(h, 'Velocity fluctuation, m/s', 'FontSize', 24, 'FontName', 'Times New Roman');
%axis equal

%% visualize reconstruction of a snapshot without adding the average

figure
subplot(1,2,1)
imagesc([x_min x_max], [y_min y_max], reshape(xp(1:templ,i),I,J))
% set(gca, 'CLim', [-0.3 0.3])
set(gca, 'YDir', 'normal')
colormap('jet');
h=colorbar
% set(gcf, 'position', [200 100 800 500])
% set(gcf, 'position', [200 120 800 500])
xlabel(gca, '$r^{*}$', 'FontSize', 28, 'Interpreter', 'latex')
ylabel(gca, '$z^{*}$', 'FontSize', 28, 'Interpreter', 'latex')
ylabel(h, 'Original Velocity, m/s', 'FontSize', 22, 'FontName', 'Times New Roman');
set(gca, 'FontSize', 22, 'FontName', 'Times');
pbaspect([1, 1.5, 1]);
% axis equal

figure
imagesc([x_min x_max], [y_min y_max], ...
flipud(reshape(xp(1:templ,400),I,J))) % Original fluctuation

pbaspect([1, 1.5, 1]);

```

```

%% %% visualization of ROM
% close all
% for i=1:1:100
%
%     figure(1);
%     set(gcf, 'outerposition', get(0, 'screensize'))           %% maximize the screen
%     set(gcf, 'color', 'w')
%     clf;
%
%     subplot(1,2,1)
%     imagesc([x_min x_max], [y_min y_max], reshape(AVG(1:end/2),[I,J]) + reshape(xp(1:temp1,i),I,J))
%     set(gca, 'CLim', [-0.3 0.3])
%     set(gca, 'YDir', 'normal')
%     colormap('jet');
%     h=colorbar
%     %     set(gcf, 'position', [200 100 800 500])
%     %     set(gcf, 'position', [200 120 800 500])
%     xlabel(gca, '$r^{*}$', 'FontSize', 28, 'Interpreter', 'latex')
%     ylabel(gca, '$z^{*}$', 'FontSize', 28, 'Interpreter', 'latex')
%     ylabel(h, 'Original Velocity, m/s', 'FontSize', 22, 'FontName', 'Times New Roman');
%     set(gca, 'FontSize', 22, 'FontName', 'Times');
%     pbaspect([1, 2, 1]);
%     %     axis equal
%
%     subplot(1,2,2)
%
%     %imagesc(data(i).U)
%     imagesc([x_min x_max], [y_min y_max], reshape(AVG(1:end/2),[I,J])+reshape(u_test(1:temp1,i),I,J))
%     % imagesc(reshape(u_test(1:size(data(1).U(:)),i),I,J))
%     set(gca, 'CLim', [-0.3 0.3])
%     h=colorbar
%     set(gca, 'YDir', 'normal')
%     %     set(gcf, 'position', [200 120 800 500])
%     colormap('jet');
%     xlabel(gca, '$r^{*}$', 'FontSize', 28, 'Interpreter', 'latex')
%     ylabel(gca, '$z^{*}$', 'FontSize', 28, 'Interpreter', 'latex')
%     ylabel(h, 'Reconstructed Velocity, m/s', 'FontSize', 22, 'FontName', 'Times New Roman');
%     pbaspect([1, 2, 1]);
%     set(gca, 'FontSize', 22, 'FontName', 'Times');
%     %     axis equal
%     %pause(0.001)
%
%
%
%     % pause(0.02)
%
% end

```

## C.2 Code for Energy Spectrum

Listing C.2: Ensemble-Averaged Energy Spectrum code

```

clc, clear all;
close all;
%% temporal average
% AVG = mean(X_Velocity_total,2);
AVG.U = mean(X.U,2);
AVG.V = mean(X.V,2);
% AVG=mean(x(1:size(data(1).U(:)),1),2);
%% spatial average

```

```

% AVG = mean(X_Velocity_total,2);
% AVG_U = mean(X_U,1);
% AVG_V = mean(X_V,1);

% %% spatial averaged operation(comment off if using temporal average)
% AVG_U = repmat(AVG_U, I*J, 1);
% AVG_V = repmat(AVG_V, I*J, 1);

% subtracting the mean from each colum of A (temporal average used)
for i=1:n_snap
%     xp(:,i)=X_Velocity_total(:,i)-AVG;
    xp_u(:,i)=X_U(:,i) - AVG_U;
    xp_v(:,i)=X_V(:,i) - AVG_V;
end
% %% spatial averaged used
%     xp_u=X_U - AVG_U;
%     xp_v=X_V - AVG_V;
MeanSquare_fluct = 1./2.*(mean(xp_u.^2, 'all') + mean(xp_v.^2, 'all'));

tc.u_fluct = reshape(xp_u,I,J, n_snap);
tc.v_fluct = reshape(xp_v,I,J, n_snap);

[Ny, Nx] = size(X); % Size of the domain

Lx = (max(X(:)) - min(X(:)))*10^(-3); % Size of the domain in meters
Ly = (max(Y(:)) - min(Y(:)))*10^(-3);
dx = Lx/(size(X,2)); % Spatial resolution

kx = (2*pi/Lx)*((-Nx/2):(Nx/2 - 1));
ky = (2*pi/Ly)*((-Ny/2):(Ny/2 - 1));

[kx, ky] = meshgrid(kx, ky);

% Radial wavenumber
% k_radial = sqrt(kx.^2);
k_radial = sqrt(kx.^2 + ky.^2);

%% calculate the average velocity spectra over time
%% clearvars
clearvars xp_u xp_v AVG_U AVG_V X_W X_V X_U
tic;
for i = 1: n_snap

% Generate 2D velocity field
U = tc.u_fluct(:, :, i);
V = tc.v_fluct(:, :, i);

% Compute 2D wavenumber spectra
u_fft = fft2(U);
v_fft = fft2(V);

u_fft_shifted = fftshift(u_fft);
v_fft_shifted = fftshift(v_fft);

% Compute the velocity spectrum
% power_spectrum = (abs(u_fft_shifted).^2 + abs(v_fft_shifted).^2) / (Lx*Ly * Nx*Ny);
power_spectrum_u = (abs(u_fft_shifted).^2) / (Lx*Ly * Nx*Ny);
power_spectrum_v = (abs(v_fft_shifted).^2) / (Lx*Ly * Nx*Ny);
Energy_Spectrum = 1./2.*(power_spectrum_u + power_spectrum_v);

% Sum the velocity spectrum over annular rings to obtain energy spectra
k_unique = unique(k_radial(:));
power_spectrum_sum = zeros(size(k_unique));

```

```

Energy_Spectrum_sum = zeros(size(k_unique));

for j = 1:numel(k_unique)
    power_spectrum_sum(j) = sum(power_spectrum_u(k_radial(:) == k_unique(j)));
    Energy_Spectrum_sum(j) = sum(Energy_Spectrum(k_radial(:) == k_unique(j)));
end

%% limit my plot
%% plot only 2 to end (reason: log-log)
k_unique = k_unique(2:end);
power_spectrum_sum = power_spectrum_sum(2:end);
%% construct stuct matrix containing k and power spectrum

Transient_VelocitySpectra(:,i) = (power_spectrum_sum(2:end))';
Transient_EnergySpectra(:,i) = (Energy_Spectrum_sum(2:end))';

end
toc;

%%
Avg_VelocitySpectra = mean(Transient_VelocitySpectra,2);
Avg_EnergySpectra = mean(Transient_EnergySpectra,2);

k_unique = k_unique(2:end);

%% Nyquist Criterion
% Create a logical index for k_unique < k_max/2
index = k_unique < max(k_unique)./2;
% index = k_unique <= max(k_unique);

%% Plot the wavenumber spectrum
figure;
loglog(k_unique(index), Avg_VelocitySpectra(index), 'o-');
% loglog(k_unique(index)./min(k_unique(index)), Avg_VelocitySpectra(index), 'o-');

pbaspect([4 4 1]);
set(gcf, 'color', 'w');
xlabel('Wavenumber (k)');
ylabel('Power Spectrum');
% title('2D Turbulence Energy Spectrum');
set(gca, 'FontSize', 30, 'FontName', 'Times');
set(gcf, 'color', 'w')
% grid on;

%% -5/3 slope
% hold on;
%
% Calculate the corresponding y-values for the shifted -5/3 slope
% shift_factor = 10^4; % You can adjust this factor to control the vertical shift
% y_slope_shifted = shift_factor * 10.^(-5/3 * log10(k_unique./min(k_unique)));
%
% Plot the shifted -5/3 slope
% loglog(k_unique./min(k_unique), y_slope_shifted, '--', 'Color', 'r', 'LineWidth', 2);
% xlim([1 150])
% Add a legend
% legend('Data', ['-5/3 Slope'], ...
'Location', [0.592239584419876 0.812819436536942 0.0994791644935806 0.0835929363811251]);
% hold off;

%%%%%%%%%%%%%%%%%%%%%%%%%%%%%%%%%%%%%%%%%%%%%%%%%%%%%%%%%%%%%%%%%%%%%%%%Energy Spectrum (normalized)%%

```

```

%%
figure
loglog(k_unique(index), Avg_EnergySpectra(index), 'o-');
% loglog(k_unique(index)./min(k_unique(index)), ...
Avg_EnergySpectra(index), 'o-', 'LineWidth',1, 'Color', 'b') ;
% xlim([1 10^2])
xlim([10^2 10^4])
ylim([10^(-4) 10^4])
pbaspect([4 4 1]);
set(gcf, 'color', 'w');
xlabel('$\kappa$, m^{-1}$', 'Interpreter', 'latex');
ylabel('$E(\kappa)$, m^2s^{-2}$', 'Interpreter', 'latex');
xValues = [10^2 305.4415 10^3 1832.6 10^4];
% Customize x-axis tick labels
xticks(xValues);
xticklabels({'$10^2$', '$\frac{2\pi}{l_0}$', '$10^3$', '$\frac{12\pi}{l_0}$', '$10^4$'});
set(gca, 'FontSize', 30, 'FontName', 'Times', 'TickLabelInterpreter', 'latex');
set(gcf, 'color', 'w')
% grid on;

%% -5/3 slope
hold on;

% Calculate the corresponding y-values for the shifted -5/3 slope
shift_factor = 2*10^4; % You can adjust this factor to control the vertical shift
y_slope_shifted = shift_factor * 10.^(-5/3 * log10(k_unique./min(k_unique)));

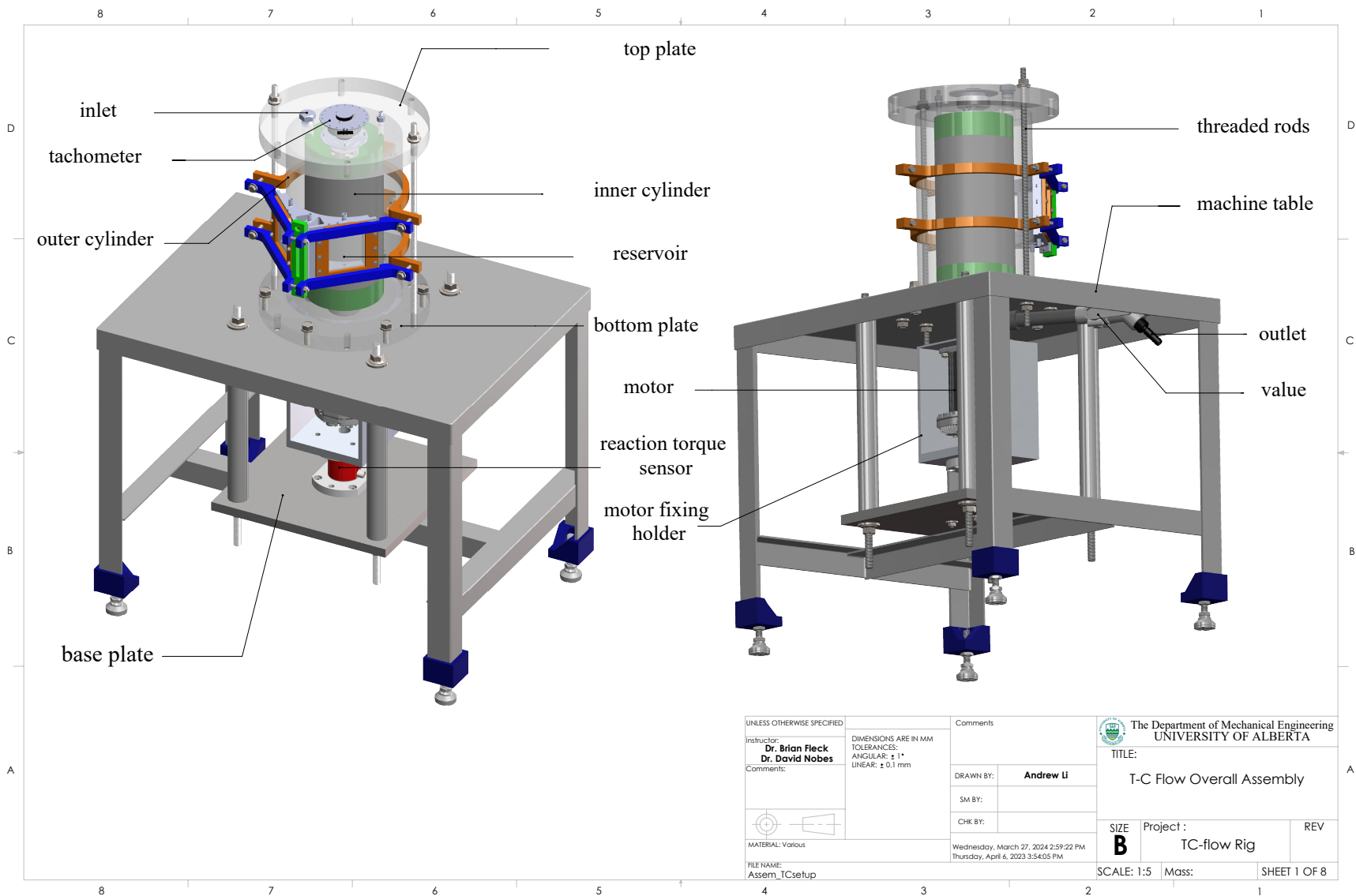
% Plot the shifted -5/3 slope
% loglog(k_unique./min(k_unique), y_slope_shifted, '-', 'Color', 'r', 'LineWidth', 3);
loglog(k_unique, y_slope_shifted, '-', 'Color', 'r', 'LineWidth', 3);

% xlim([1 200])
% Add a legend
legend('PAM-200ppm, Re = 15000', 'Position', ...
[0.520208198988503 0.846723899855839 0.184166935356326 0.0490135009167472], ...
'Interpreter', 'latex');

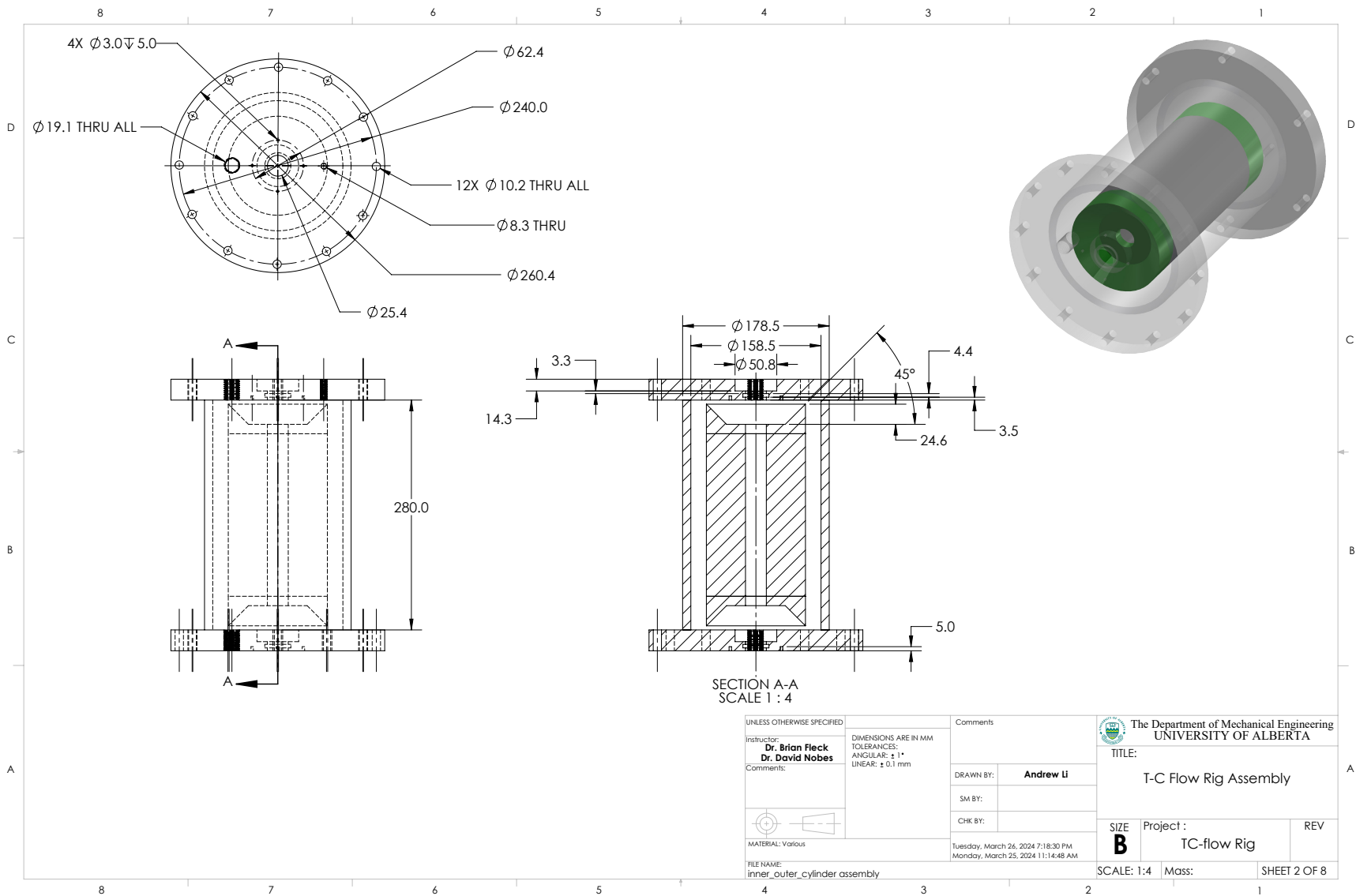
% Create textbox
annotation('textbox', ...
[0.601 0.746625129802699 0.0474374999999995 0.0612668743509862], ...
'String', {'-5/3'}, ...
'LineStyle', 'none', ...
'Interpreter', 'latex', ...
'FontSize', 30, ...
'FontName', 'Times', ...
'FitBoxToText', 'off');
hold off;

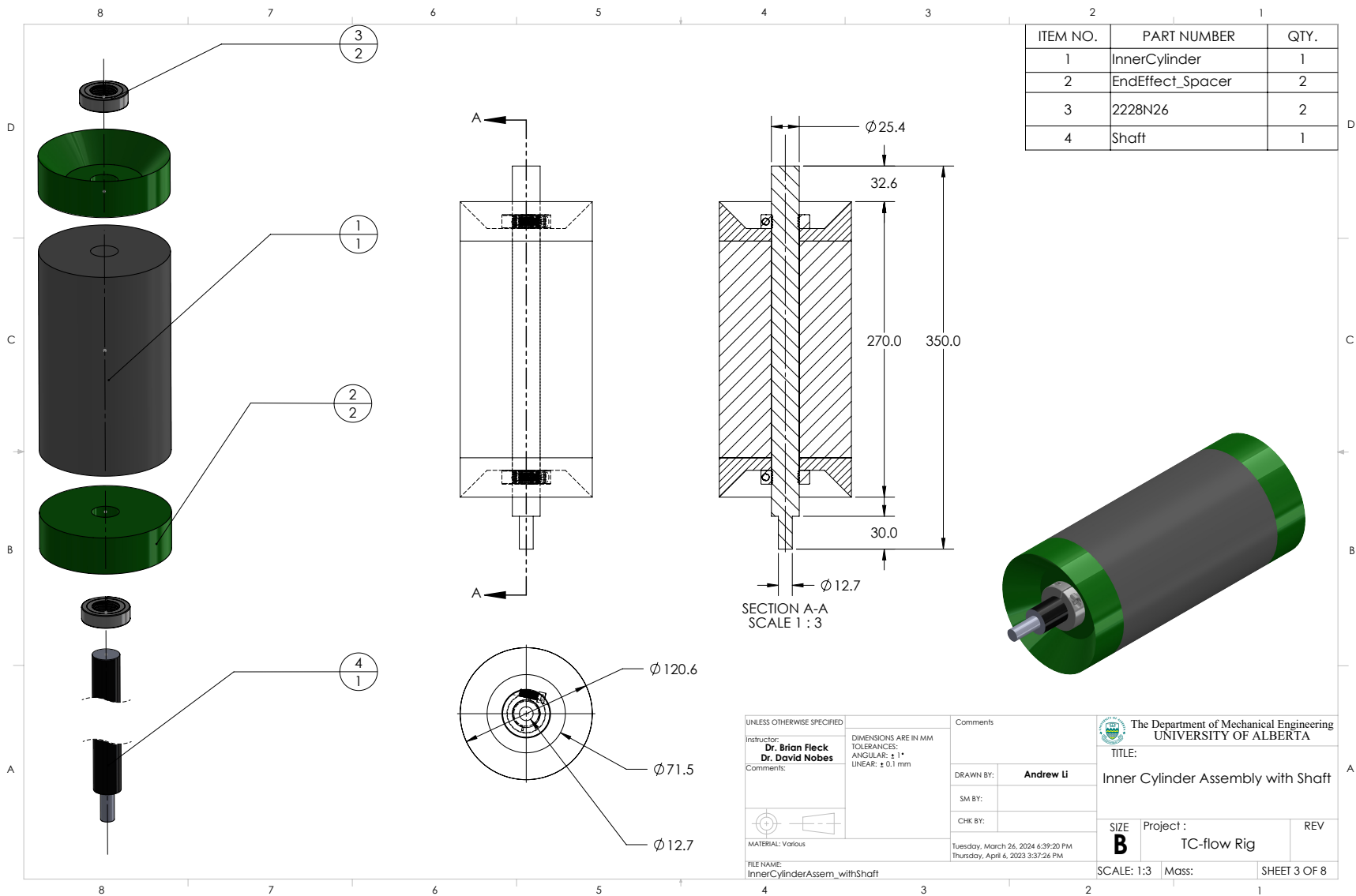
```

# Appendix D: Engineering Drawings of Taylor-Couette Flow Rig

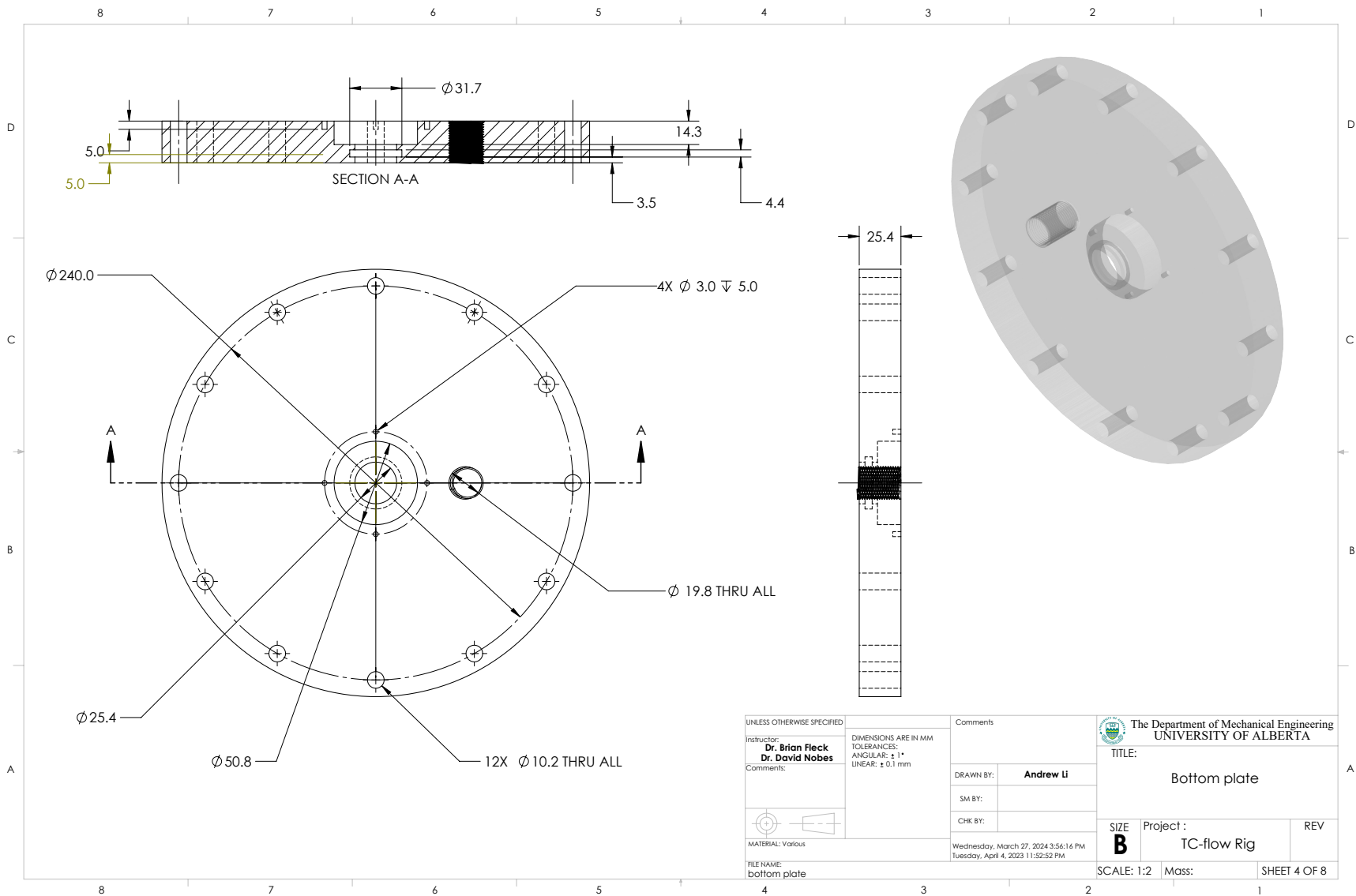


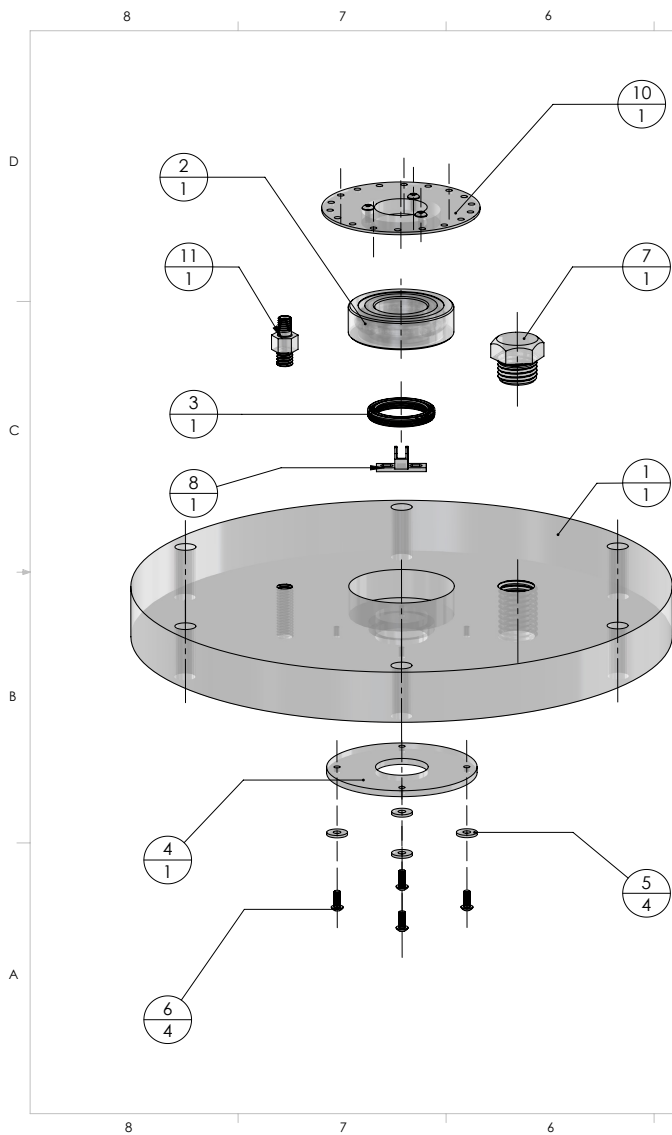
UNLESS OTHERWISE SPECIFIED		Comments	 The Department of Mechanical Engineering UNIVERSITY OF ALBERTA	
Instructor: <b>Dr. Brian Fleck</b> <b>Dr. David Nobes</b> Comments:			TITLE: T-C Flow Overall Assembly	
DIMENSIONS ARE IN MM TOLERANCES: ANGULAR: $\pm 1^\circ$ LINEAR: $\pm 0.1$ mm		DRAWN BY: <b>Andrew Li</b>	Project : TC-flow Rig	
		SM BY:	SIZE <b>B</b>	
		CHK BY:	SCALE: 1:5	
MATERIAL: Various FILE NAME: Assem_TCsetup		Wednesday, March 27, 2024 2:59:22 PM Thursday, April 4, 2023 3:54:05 PM		REV
		SHEET 1 OF 8		



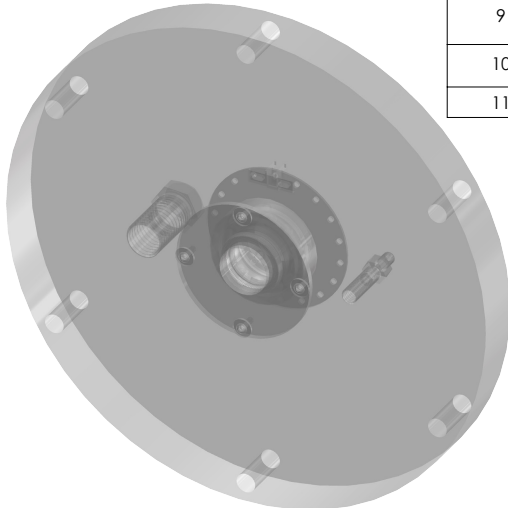


UNLESS OTHERWISE SPECIFIED		Comments	The Department of Mechanical Engineering UNIVERSITY OF ALBERTA	
Instructor: <b>Dr. Brian Fleck</b> <b>Dr. David Nobes</b> Comments:			TITLE: Inner Cylinder Assembly with Shaft	
DIMENSIONS ARE IN MM TOLERANCES: ANGULAR: ± 1° LINEAR: ± 0.1 mm		DRAWN BY: <b>Andrew Li</b>	SIZE <b>B</b> Project: TC-flow Rig REV	
MATERIAL: Various FILE NAME: InnerCylinderAssem_withShaft		SM BY:	SCALE: 1:3 Mass: SHEET 3 OF 8	
CHECKED BY: DATE: Tuesday, March 26, 2024 4:39:20 PM Thursday, April 4, 2023 3:37:26 PM				

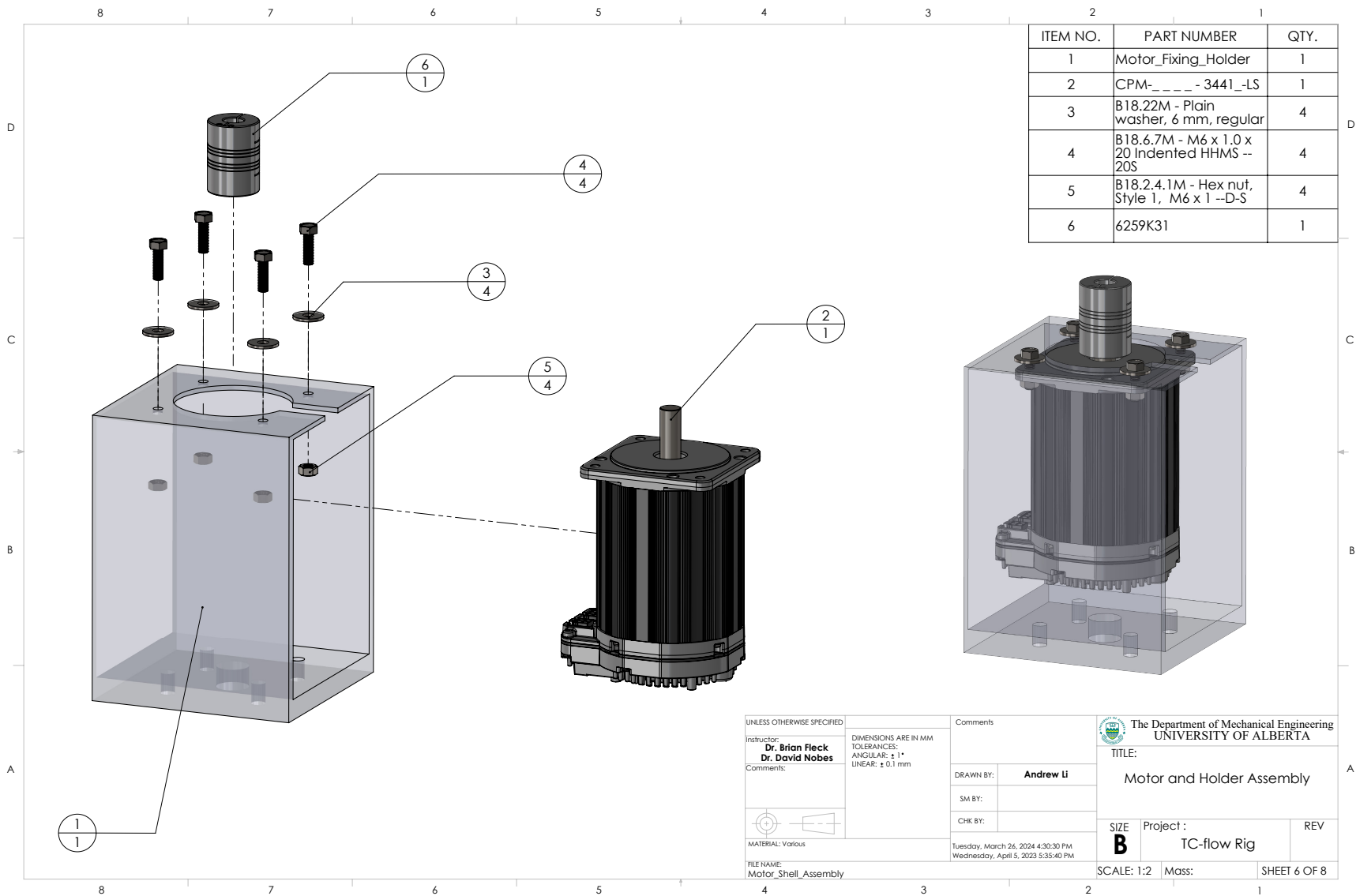


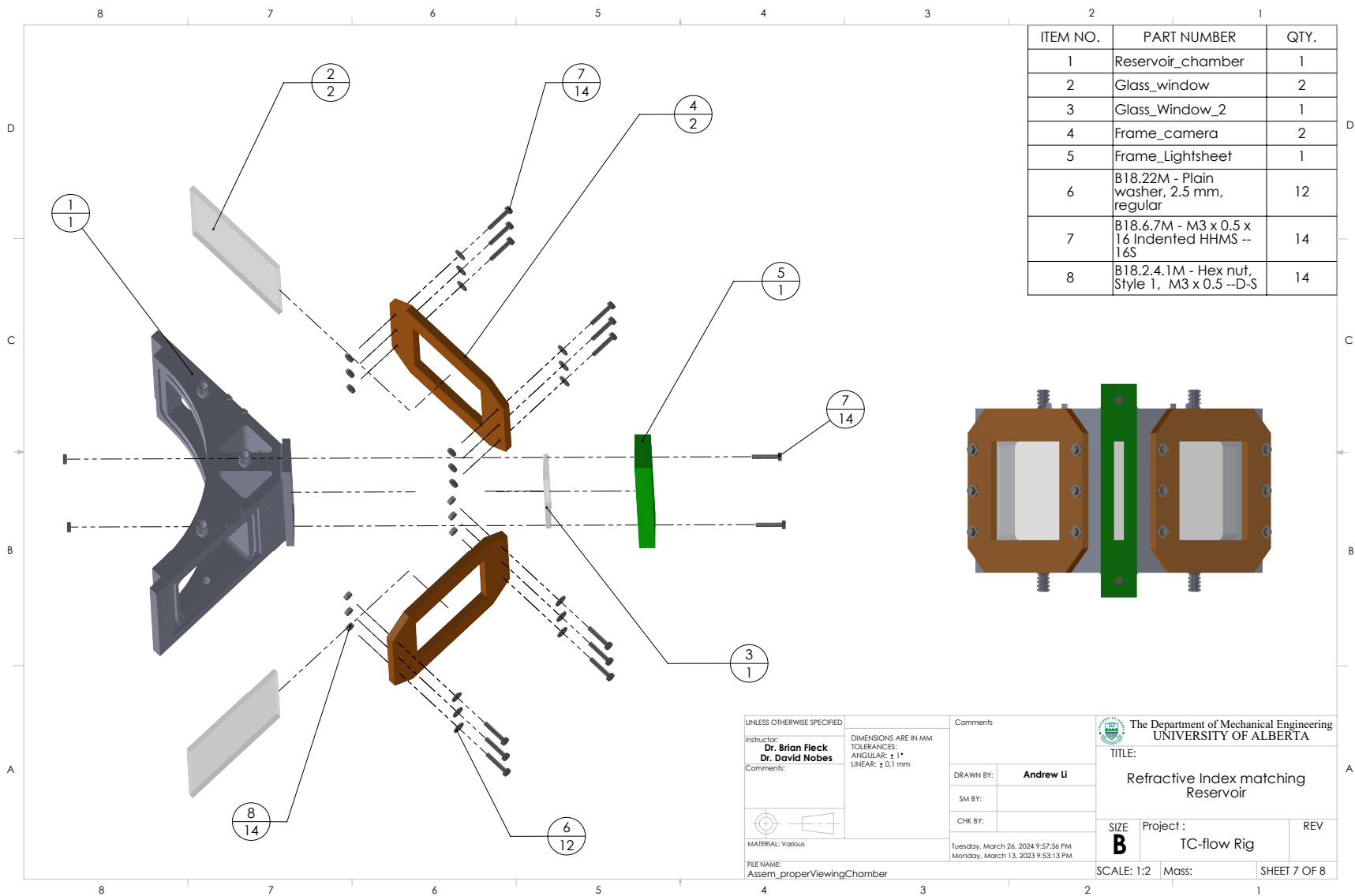


ITEM NO.	PART NUMBER	QTY.
1	top plate	1
2	2780T66	1
3	13125K85	1
4	Acrylic seal	1
5	B18.22M - Plain washer, 3 mm, regular	4
6	B18.3.4M - 3 x 0.5 x 8 SBHCS -S	4
7	92655A401	1
8	tachometer_support	1
9	B18.22M - Plain washer, 10 mm, narrow	2
10	tachometer_rotary_wif hBolt	1
11	Lok_tube_A	1



UNLESS OTHERWISE SPECIFIED	DIMENSIONS ARE IN MM TOLERANCES: ANGULAR: ± 1° LINEAR: ± 0.1 mm	Comments		The Department of Mechanical Engineering UNIVERSITY OF ALBERTA
		Instructor: <b>Dr. Brian Fleck</b> <b>Dr. David Nobes</b>		
Comments:		DRAWN BY:	<b>Andrew Li</b>	SIZE <b>B</b> Project: TC-flow Rig REV
		SM BY:		
MATERIAL: Various		CHK BY:		Wednesday, March 27, 2024 4:04:50 PM Thursday, April 4, 2023 3:02:02 PM
FILE NAME: top_plate_seal_ballbearing		SCALE: 1:2		Mass: SHEET 5 OF 8





ITEM NO.	PART NUMBER	QTY.
1	Reservoir_chamber	1
2	Glass_window	2
3	Glass_window_2	1
4	Frame_camera	2
5	Frame_Lightsheet	1
6	B18.22M - Plain washer, 2.5 mm, regular	12
7	B18.6,7M - M3 x 0.5 x 16 Indented HHMS -- 16S	14
8	B18.2,4.1M - Hex nut, Style 1, M3 x 0.5 --D-S	14

UNLESS OTHERWISE SPECIFIED

Instructor:  
**Dr. Brian Fleck**  
**Dr. David Nobes**

Comments:

DIMENSIONS ARE IN MM  
TOLERANCES:  
ANGULAR: ± 1°  
LINEAR: ± 0.1 mm

MATERIAL: Various

FILE NAME:  
Assem\_properViewingChamber

Comments

DRAWN BY: **Andrew Li**

SM BY:

CHK BY:

Tuesday, March 26, 2024 9:57:56 PM  
Monday, March 13, 2023 9:53:13 PM

The Department of Mechanical Engineering  
UNIVERSITY OF ALBERTA

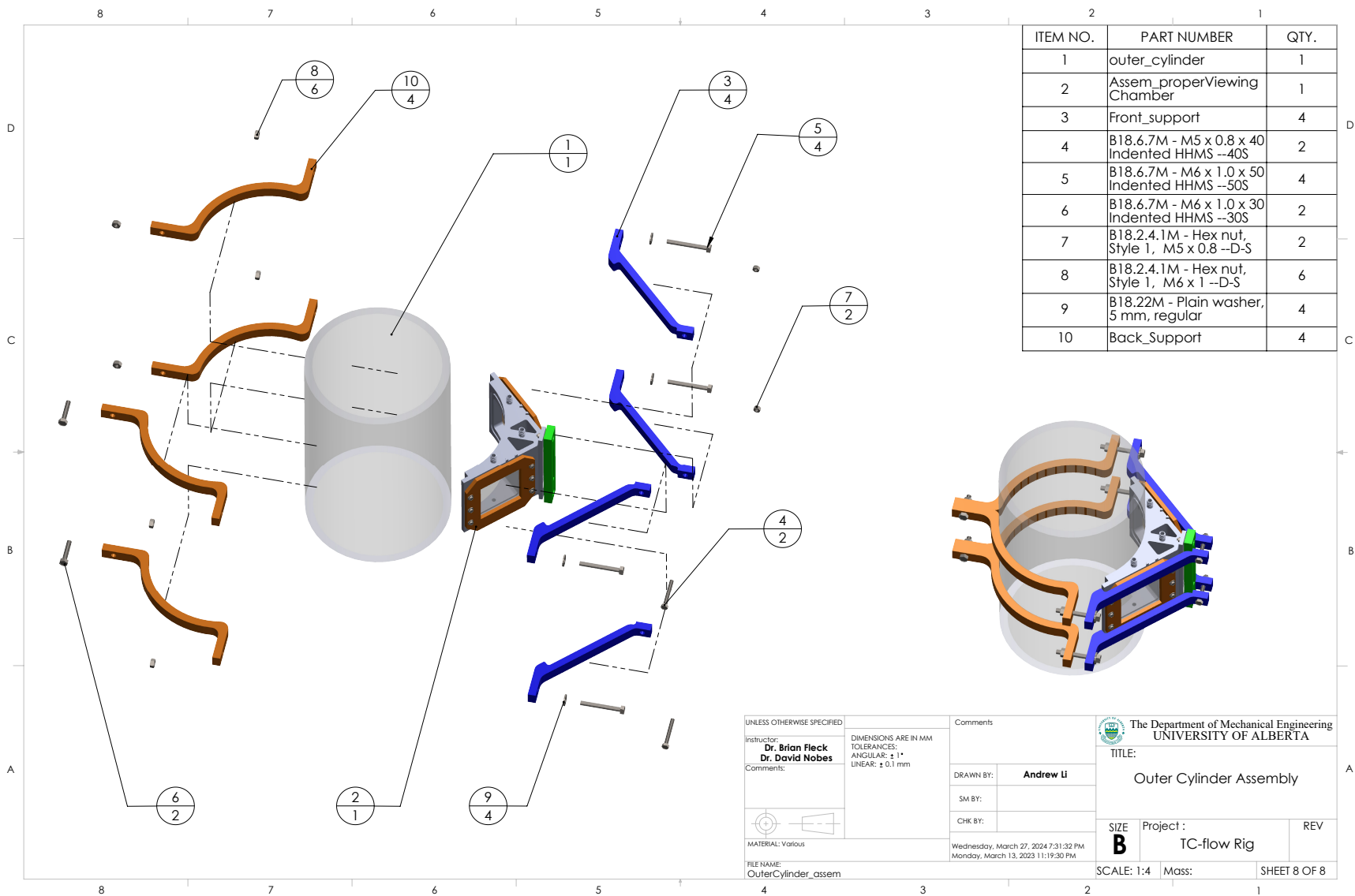
TITLE:  
**Refractive Index matching Reservoir**

Project : **TC-flow Rig**

SCALE: 1:2

Mass:

SHEET 7 OF 8



ITEM NO.	PART NUMBER	QTY.
1	outer_cylinder	1
2	Assem_properViewing Chamber	1
3	Front_support	4
4	B18.6.7M - M5 x 0.8 x 40 Indented HHMS --40S	2
5	B18.6.7M - M6 x 1.0 x 50 Indented HHMS --50S	4
6	B18.6.7M - M6 x 1.0 x 30 Indented HHMS --30S	2
7	B18.2.4.1M - Hex nut, Style 1, M5 x 0.8 --D-S	2
8	B18.2.4.1M - Hex nut, Style 1, M6 x 1 --D-S	6
9	B18.22M - Plain washer, 5 mm, regular	4
10	Back_Support	4

UNLESS OTHERWISE SPECIFIED Instructor: <b>Dr. Brian Fleck</b> <b>Dr. David Nobes</b> Comments:	DIMENSIONS ARE IN MM TOLERANCES: ANGULAR: ± 1° LINEAR: ± 0.1 mm	Comments		The Department of Mechanical Engineering <b>UNIVERSITY OF ALBERTA</b> TITLE: <b>Outer Cylinder Assembly</b>
		DRAWN BY:	<b>Andrew Li</b>	
MATERIAL: Various		SM BY:		SCALE: 1:4 Mass: SHEET 8 OF 8
FILE NAME: OuterCylinder_assem		CHK BY:		
		Wednesday, March 27, 2024 7:31:32 PM Monday, March 13, 2023 11:19:30 PM		